Self-Energy and Self-Consistency Within Many-Body Perturbation Theory

Sijen, Javier G.

Award date:
2020

Self-Energy and Self-Consistency Within Many-Body Perturbation Theory

Master Project

Javiér Sijen (0784557)
j.g.sijen.1@student.tue.nl

Eindhoven University of Technology
Department of Mathematics and Computer Science

Supervisor: dr. B. Baumeier

June 2, 2020

Contents

List of Figures

Abstract

In this thesis, I investigate the excited-state properties of molecules within the Many-Body Perturbation Theory (MBPT) framework. MBPT is formulated as a hierarchy of coupled equations-of-motion for the Green's functions. The so-called GW approximation decouples these equations such that simulations of single-electron creation and annihilation processes are possible. The central quantity of the GW approximation is the self-energy operator Σ. I investigate two methods for calculating the self-energy; one analytical method and one approximate method. I implement the analytical calculation in the VOTCA software suite. The accuracy and scaling of this implementation is benchmarked using other software packages and theoretical estimates. I argue that the analytical method is better suited for benchmarking other GW implementations, whereas approximate methods are better suited for large scale analyses.

Acknowledgements

I would like to thank my supervisor Björn Baumeier for this project and opportunity to explore the field of quantum mechanics. I would also like to thank Jens Wehner for his feedback, directions and mini crash courses in quantum mechanics during the entire duration of the project. Furthermore, I would like to thank the entire VOTCA team, including Gianluca, Onur, Pranav, Vivek, Wouter and Yuriy, whom I've had the pleasure of meeting, and of course Björn and Jens, for their research on the subject and providing the basis for my project.

Chapter 1

Introduction

Quantum Mechanics (QM) is a branch of physics that describes physical phenomena on the atomic and subatomic level. Mathematical problems that arise in QM are complicated; either an analytical solution cannot be obtained or a numerical solution is computationally expensive. Since numerical approximations are typically the best we have, QM calculations are generally performed on computers. The goal is to construct computational models that accurately simulate real-world experiments. These computational models may in turn reveal properties that real-world experiments cannot. Since QM simulations are computationally demanding, QM models can only describe a few physical phenomena at once and are limited in space and time scales. With increasingly powerful computers, the scale and resolution of these simulations is improved.

One application of QM is the development of organic solar cells. In an increasingly technologically advanced society, clean and renewable sources of electricity are vital. Power generation in a solar cell depends on three principal steps: (1) the absorption of light and creation of an electron-hole pair through molecular excitation (2) the separation of the electron-hole pair into two separate charge carriers and (3) the propagation of the charge carriers to opposite poles, causing an electrical current. QM models can help us explain these processes and in turn reveal techniques to increase their efficiency. In this thesis, we to take a closer look at the first step: the excitation process.

In order to explain excitation processes, we must first describe the molecular system. The molecular system is a collection of atoms, where each atom consists of a positively charged nucleus and a negatively charged electron cloud surrounding it. We model the molecular system using Molecular Orbital (MO) theory. In MO theory, every electron must occupy a particular orbital around its nucleus. Each orbital has an energy associated to it, which corresponds to the energy an electron needs to occupy that orbital. There are infinitely many orbitals, but only a finite number of electrons. In the ground state, the electrons occupy the lowest-energy orbitals such that the total energy of the system is minimized.

We can disturb the ground state electron configuration by supplying the molecule with extra energy. Photons can be seen as packets of energy. Through photo-absorption, electrons are able to absorb a photon's energy, causing the electron to be transferred into a higher-energy orbital. The molecule is now excited. In the excited state, the electron arrangement is

disturbed and the total energy of the system is increased. The energy that is required for this transfer process is called the *excitation energy*. We will see that the excitation energy can be approximated by the energy difference between the lower-energy orbital and the higher-energy orbital. This is a crude approximation, however. In reality, the entire system reacts to the excitation, which influences the excitation energy.

The orbital energies are a result of interaction forces between the electrons and otherwise external forces exerted on the system. The interaction forces depend on the relative positions of the electrons. Heisenberg's uncertainty principle states that both the electron position and momentum cannot be known simultaneously. Instead of tracking the exact position of every electron individually, we estimate the probability of each electron being at a given position. The probability density of the electron positions is called the electron density. The problem now is quantifying the electron density.

A popular technique for determining the electron density is Density Functional Theory (DFT) [1]. Because of its popularity, in 1998 one of its inventors, W. Kohn, received a Nobel Prize for it [2]. DFT is based on the notion that, in the ground state, the electrons arrange themselves such that the total system energy is minimized. We can calculate expectation values of the total system energy via functionals of the electron density. We can subsequently estimate excitation energies by computing energy differences between excited states and the ground state. A well-known practical problem with DFT is that the energy functional contains terms, called exchange-correlation, whose form is unknown and need to be approximated. While DFT accurately predicts the ground state energies of molecules, it underestimates excitation energies for most materials [3]. This problem is known as the "band gap problem".

Using the framework of Many-Body Perturbation Theory (MBPT), we can more accurately describe the excited state system in terms of the simpler ground state system [4]. MBPT is formulated as a hierarchy of coupled equations-of-motion for the Green's functions. The so-called GW approximation decouples these equations such that simulations of single-particle creation and annihilation processes are possible. Using these single-particle processes, we can subsequently model two-particle excitation processes in which one electron jumps from a low-energy orbital to a higher-energy orbital. To this end, we must solve the Bethe-Salpeter Equation (BSE). The ground state system, which serves as an initial "guess" to the GW step, can be obtained through a preceding DFT calculation. This three-step procedure is called DFT-GW-BSE, or more commonly GW-BSE.

The central quantity of the GW approximation is the *self-energy* operator Σ, which reads

$$\Sigma\left(\mathbf{r},\mathbf{r}',\omega\right)=\frac{i}{2\pi}\int \mathrm{d}\omega' e^{i\eta\omega'}G(\mathbf{r},\mathbf{r}',\omega+\omega')W(\mathbf{r},\mathbf{r}',\omega'). \tag{1.1}$$

The calculation of the frequency-dependence in particular involves computationally expensive convolution of the Green's function G and the screened Coulomb interaction W. The evaluation of W requires the calculation of the polarizability P. The polarizability of a molecule is the tendency of its electron cloud to be distorted by an external electric field. The calculation of P involves a particularly complicated frequency-dependence. There are several ways for dealing with this frequency-dependence. We will find that P can be calculated analytically by solving an eigenvalue problem of the size of the *transition space*, i.e. the space of all possible electronic excitations. This method is referred to as the *Fully-Analytical Approach*, or

FAA in short. While FAA yields an analytical expression of P, it involves a computationally demanding eigenvalue problem. Alternatively, we will find that we can approximate P using a *plasmon-pole* model, This method is referred to as the *Plasmon-Pole Model*, or *PPM* in short. While the PPM is computationally cheap, it provides us only with an approximation of P.

Typically, approximate methods are aimed at describing large scale systems, whereas analytical methods are aimed at accuracy and robustness of the calculated quantities with respect to experimental results. An analytical method therefore offers a reliable reference point for the development and application of approximate methods.

In this thesis, we implement the FAA for GW-BSE in the VOTCA-XTP package as part of the VOTCA software suit [5, 6, 7]. The role of VOTCA-XTP is the simulation of electronic states and excitation transport [8]. Importantly, it implements the three-step DFT-GW-BSE procedure. VOTCA-XTP is written in C++ and is freely available on Github [9].

The thesis is structured as follows. First, the theoretical footing is established in Chapter 2. Next, in Chapter 3, the mathematical formulation of GW, and specifically the FAA, is outlined. In Chapter 4, we briefly discuss the practicalities of the implementation. The accuracy and scaling of the implementation is tested in Chapter 5. Finally, in Chapter 6 we summarize the thesis and reflect on the results.

Chapter 2

Theoretical Background

In this chapter, we discuss electronic structure theory and its application in modeling molecular excitation processes. First, we briefly go over the fundamental quantum mechanical concepts and introduce the quantum system. Next, we give a quantum mechanical description of molecular systems. We then describe how we compute the ground state energies of molecular systems using Density Functional Theory (DFT). Finally, we move on to the GW-BSE method for calculating excitation energies of molecular systems using DFT input.

2.1 The Quantum System

Before we begin modeling the molecular system, we briefly go over the fundamental concepts of quantum mechanics. We introduce the wave function, which describes the quantum state of the quantum system. Furthermore, we introduce the Schrödinger equation, which describes the time evolution of the wave function.

We consider a region of space in which various particles interact with each other. This collection of particles and interactions may be referred to as the *quantum system*. Any physical quantity that can be measured in the system is an *observable*. The *quantum state* provides a probability distribution for the value of each observable, i.e. for the outcome of each possible measurement on the system. Mathematically, we describe the quantum state by a complex-valued probability amplitude; the *wave function*, which we typically denote by $|\Psi\rangle$. The wave function exists in a Hilbert space, representing the *state space* of the system. An observable operator $\hat{O}$, also simply referred to as "observable", is a Hermitian operator that maps the wave function into itself: $\hat{O}\,|\Psi_i\rangle = \lambda_i\,|\Psi_i\rangle$. The eigenstate $|\Psi_i\rangle$ represents the observed state and the eigenvalue λ_i denotes the value of the physical quantity related to the observable $\hat{O}$.

Central to the study of quantum mechanics is the Schrödinger equation, which describes the time evolution of the wave function. The Schrödinger equation is regarded as the quantum-analogue to Newton's laws in classical mechanics. The time-dependent Schrödinger equation is given by:

$$\hat{H}\,|\Psi(t)\rangle = i\hbar\frac{\partial}{\partial t}\,|\Psi(t)\rangle\,. \tag{2.1}$$

The Hamiltonian $\hat{H}$ is the operator corresponding to the total energy of the system. If we could solve the Schrödinger equation for the wave function, we could fully describe the evolution of the quantum system. In the next section, we give a specific example of a quantum system; namely, the molecular system.

2.2 The Molecular System

The molecular system is described as a collection of atoms. Each atom has a positively charged nucleus, containing protons and neutrons, with negatively charged electrons surrounding it. We consider a system with M nuclei and N electrons. The nuclei positions are given by $\mathbf{R} = \{\mathbf{R}_1, \mathbf{R}_2, \ldots, \mathbf{R}_M\}$ and the electron positions are given by $\mathbf{r} = \{\mathbf{r}_1, \mathbf{r}_2, \ldots, \mathbf{r}_N\}$. All particle positions are given in three-dimensional coordinates, i.e. in $\mathbb{R}^3$. The charges of the nuclei are given by $\mathbf{Z} = \{Z_1, Z_2, \ldots, Z_M\}$, $Z_j \in \mathbb{N}^+$ and the charges of the electron equal negative the elementary charge, i.e. $z_i = -1, i = 1, 2, \ldots, N$. All values are expressed in atomic units[1].

We can describe the electronic structure of molecular systems using Molecular Orbital (MO) theory. The electrons do not float around the molecule randomly. Instead, every electron must occupy a *Molecular Orbital* (MO). Essentially, an MO represents the region of space where its occupying electrons are likely to be found. Each orbital has an energy associated to it, called the *energy level*, which corresponds to the energy an electron needs to occupy that orbital. There are infinitely many MOs, but only a finite number of electrons to occupy them with. According to the Pauli exclusion principle, each MO can be occupied by up to two electrons with opposite spin.

The energy level of an MO depends on the electrostatic forces between its occupying electrons and the remaining electrons. While any two MOs describe unique electronic orbitals, their energy levels may be the same. In that case, the MOs are referred to as being *degenerate*. In the ground-state, the electrons fill up the lowest-energy *valence* MOs while the higher-energy *conduction* MOs remain empty [2]. This is referred to as the Aufbau principle. The Highest Occupied Molecular Orbital is abbreviated by HOMO and the Lowest Unoccupied Molecular Orbital is abbreviated by LUMO. We often visualize the MOs of a molecule using MO diagrams, as shown in Figure 2.1 (A).

Through photo-excitation, an electron may be transferred from an occupied MO to an unoccupied MO, as shown in Figure 2.1 (B). All electrons in the system react to this transfer process and the energy levels of all MOs change. The energy that is required for this transfer process is called the *excitation energy* or the *band gap*. In particular, the energy required to transfer the electron from the HOMO to the LUMO is called the *HOMO-LUMO gap*. We are interested in predicting the excitation energies.

In order to mathematically describe the molecular system, we set up the molecular wave function $\Psi(\mathbf{r}, \mathbf{R}, t)$, which represents a snap-shot, spatial description of the system. The time

[1] We use atomic units: $m_e \equiv 1$, $e \equiv 1$, $\hbar = h/(2\pi) \equiv 1$ and $k_e = 1/(4\pi_0) \equiv 1$.

[2] The terms valance/conduction originate from solid state systems. In molecular systems, we also use occupied/virtual.

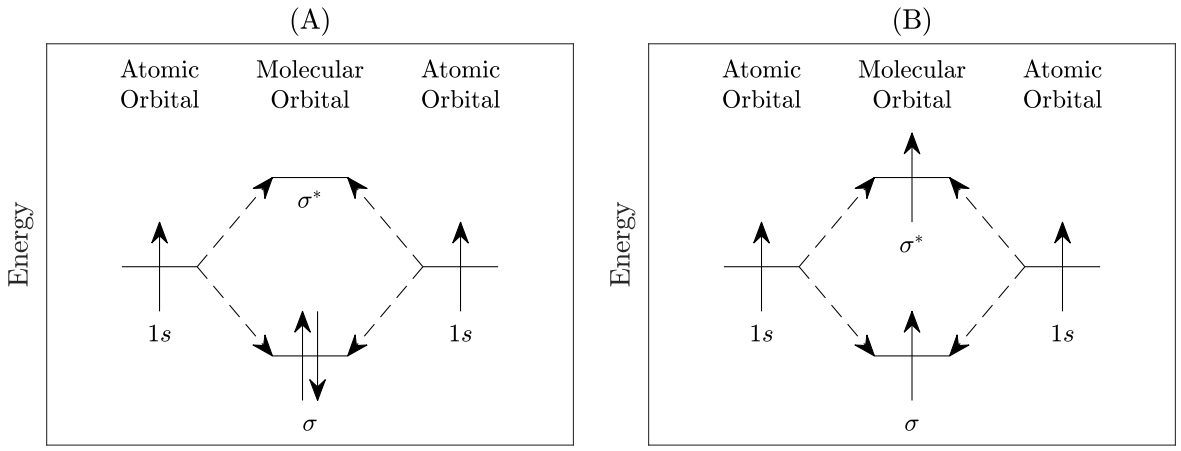

Figure 2.1: Molecular Orbital (MO) diagrams of the hydrogen molecule H_2. The orbitals are represented by horizontal bars and the electrons are represented by arrows. The direction of the arrows represent the relative spin (spin-up or spin-down) of the electrons occupying that orbital. The y-axis denotes orbital energy and the x-axis denotes no physical quantity. (A) The ground-state MO diagram of H_2. Two Atomic Orbitals (AOs) are combined (dashed arrows) to form one lower-energy sigma (σ) bonding Molecular Orbital (MO). (B) An excited-state Molecular Orbital diagram of H_2. One of the electrons in the low-energy σ MO is excited to the high-energy σ^* MO.

evolution of the system is governed by the Schrödinger equation (Equation 2.1), which we repeat below [3]:

$$\hat{H} \left|\Psi(\mathbf{r}, \mathbf{R}, t)\right\rangle = i\hbar \frac{\partial}{\partial t} \left|\Psi(\mathbf{r}, \mathbf{R}, t)\right\rangle . \tag{2.2}$$

The Hamiltonian $\hat{H}$ is the operator corresponding to the total energy of the system. Since $\hat{H}$ is time-independent, we can separate Equation 2.2 into a temporal (subscript t) and spatial (subscript s) part:

$$\Psi(\mathbf{r}, \mathbf{R}, t) = \Psi_s(\mathbf{r}, \mathbf{R}) \Psi_t(t), \tag{2.3}$$

such that

$$\Psi_t(t) = \exp(-iEt), \tag{2.4}$$

$$\hat{H} \left|\Psi_s(\mathbf{r}, \mathbf{R})\right\rangle = E \left|\Psi_s(\mathbf{r}, \mathbf{R})\right\rangle . \tag{2.5}$$

Here E denotes the scalar total energy of the system given the particle positions $\mathbf{r}$ and $\mathbf{R}$. The total energy of the system comprises the kinetic energy and the potential energy of the particles. The kinetic energy is a result of particle motion whereas potential energy is a result of particle interaction such as electrostatic repulsion and chemical bonds. Accordingly, we write the Hamiltonian operator $\hat{H}$ of the system as a sum of individual operators:

$$\hat{H} = \hat{T}_{\text{el}} + \hat{T}_{\text{nuc}} + \hat{V}_{\text{el-el}} + \hat{V}_{\text{nuc-nuc}} + \hat{V}_{\text{nuc-el}}, \tag{2.6}$$

[3] We restrict our analysis to closed shell systems, in which each MO is occupied by 2 electrons with opposite spin, resulting in a net magnetization of zero. The spin variable is thus implicitly accounted for.

with $\hat{T}_{\text{el}}$ and $\hat{T}_{\text{nuc}}$ the kinetic energy operators of the electrons and nuclei respectively:

$$\hat{T}_{\text{el}} = \sum_i \frac{\hat{\mathbf{p}}_i^2}{2m_{\mathbf{e}}}, \tag{2.7}$$

$$\hat{T}_{\text{nuc}} = \sum_I \frac{\hat{\mathbf{P}}_I^2}{2M_I}, \tag{2.8}$$

$\hat{V}_{\text{el-el}}$ and $\hat{V}_{\text{nuc-nuc}}$ the electron-electron and nucleus-nucleus interaction operators respectively:

$$\hat{V}_{\text{el-el}} = \frac{1}{2}\sum_{i\neq j} \frac{-1\cdot -1\cdot e^2}{|\mathbf{r}_i - \mathbf{r}_j|}, \tag{2.9}$$

$$\hat{V}_{\text{nuc-nuc}} = \frac{1}{2}\sum_{I\neq J} \frac{Z_I\cdot Z_J\cdot e^2}{|\mathbf{R}_I - \mathbf{R}_J|}, \tag{2.10}$$

and finally $\hat{V}_{\text{nuc-el}}$ the nucleus-electron interaction operator:

$$\hat{V}_{\text{nuc-el}} = \sum_{i,I} \frac{-1\cdot Z_I\cdot e^2}{|\mathbf{r}_i - \mathbf{R}_I|}. \tag{2.11}$$

Given the expression of the Hamiltonian and a set of initial conditions, we could in principle solve the Schrödinger equation (Equation 2.2) to obtain the wave function Ψ and thus a full description of the system. In 1926 E. Schrödinger published the solution for the hydrogen atom [10]. The hydrogen atom is a 2-body system containing only one nucleus ($M = 1$) and one electron ($N = 1$). For this particular case, the Schrödinger equation can be separated into two simpler and analytically solvable equations through separation of variables. Generally, the Schrödinger equation cannot be solved analytically and we must therefore resort to numerical methods. However, even for small but technologically relevant systems, numerical computations are extremely demanding because of the sheer number of variables involved. To facilitate numerical calculations, we need to make several approximations.

2.2.1 Born-Oppenheimer Approximation

For molecular systems, a sensible approximation is the Born-Oppenheimer approximation, which was proposed by M. Born and R. Oppenheimer in 1927 [11]. The Born-Oppenheimer approximation is the assumption that the motion of nuclei and electrons can be treated separately. It makes use of the fact that nuclei are about three orders of magnitude heavier than electrons. Consequently, electrons react near instantly to the movement of nuclei. Or conversely, from the electron's perspective the nuclei appear to be stationary. The underlying assumption is that the nuclei positions $\mathbf{R}$ remain fixed and only enter the problem as parameters. By applying this approximation, we can separate the wave function in an electronic wave function Ψ_{el} and a nuclear wave function Ψ_{nuc}:

$$\Psi_s(\mathbf{r}, \mathbf{R}) = \Psi_{\text{el}}(\mathbf{r}; \mathbf{R})\Psi_{\text{nuc}}(\mathbf{R}). \tag{2.12}$$

The nuclei positions $\mathbf{R}$ only enter as parameters in the electronic wave function and are hereafter neglected in the notation. The electronic system is now governed by the electronic Schrödinger equation. Using this approximation, we simplify Equation 2.5 to:

$$\hat{H}_{\text{el}} \left|\Psi_{\text{el}}(\mathbf{r})\right\rangle = E_{\text{el}} \left|\Psi_{\text{el}}(\mathbf{r})\right\rangle, \tag{2.13}$$

where E_{el} denotes the total energy of the electron system and $\hat{H}_{\text{el}}$ the electronic Hamiltonian:

$$\hat{H}_{\text{el}} = \hat{T}_{\text{el}} + \hat{V}_{\text{el-el}} + \hat{V}_{\text{nuc-el}}. \tag{2.14}$$

Using the Born-Oppenheimer approximation, we simplify the nuclei-electron interactions by treating their motion separately. However, The electron-electron interactions still pose difficulties since the dynamics of one electron is influenced by all other electrons in the system.

2.2.2 Independent Particle System

Before dealing with the complicated electron-electron interactions, let us first consider the simplistic case in which the electrons are non-interacting. By neglecting the electron-electron interactions entirely, the Hamiltonian reduces to a sum of one-particle Hamiltonians $\hat{h}_i$:

$$\hat{H}_{\text{el}} = \hat{T}_{\text{el}} + \hat{V}_{\text{nuc-el}} = \sum_i \hat{h}_i, \qquad \hat{h}_i := \frac{\hat{\mathbf{p}}_i^2}{2} - \sum_I \frac{Z_I}{|\mathbf{r}_i - \mathbf{R}_I|}. \tag{2.15}$$

Now, each one-particle problem $\hat{h}_i\phi_i = \varepsilon_i\phi_i$ can be solved independently, with ϕ_i being the one-particle wave function and ε_i the one-particle energy. Since $\hat{h}_i$ acts only on ϕ_i, we have $\hat{h}_i\phi_j = 0$, for all $i \neq j$. The full electronic wave function can thus be written as a product of one-particle wave functions [12, 13]:

$$\Psi_{\text{el}}(\mathbf{r}) \approx \Psi_{\text{H}}(\mathbf{r}) = \prod_i \phi_i(\mathbf{r}_i). \tag{2.16}$$

This is the Hartree wave function. A shortcoming of the Hartree wave function is that it does not satisfy the anti-symmetry constraint imposed by the Pauli-Exclusion principle:

$$\Psi(\mathbf{r}_1, \mathbf{r}_2, \ldots, \mathbf{r}_i, \mathbf{r}_j, \ldots, \mathbf{r}_{N-1}, \mathbf{r}_N) = -\Psi(\mathbf{r}_1, \mathbf{r}_2, \ldots, \mathbf{r}_j, \mathbf{r}_i, \ldots, \mathbf{r}_{N-1}, \mathbf{r}_N). \tag{2.17}$$

In order to satisfy the anti-symmetry constraint, the wave function can instead be approximated by a *Slater determinant* [14]:

$$\Psi_{\text{el}}(\mathbf{r}) \approx \Psi_{\text{HF}}(\mathbf{r}) = \frac{1}{\sqrt{N!}} \begin{vmatrix} \phi_1(\mathbf{r}_1) & \ldots & \phi_N(\mathbf{r}_1) \\ \vdots & \ddots & \vdots \\ \phi_1(\mathbf{r}_N) & \ldots & \phi_N(\mathbf{r}_N) \end{vmatrix}. \tag{2.18}$$

In either case, the advantage of the simplistic independent-particle system is that energy levels do not depend on electron-electron interactions. In particular, the energy levels are unaffected when an electron is transferred from one MO to the other. In this case, the excitation energy simply equates to the energy level difference, as shown in Figure 2.2 (A). On the other hand, in a fully-interacting system, the remaining electrons react to the excitation process, resulting in a shift of the energy levels. In this case, the excitation energy does not equate to the pre-excitation energy level difference, as shown in Figure 2.2 (B). While the independent-particle system is insufficient to describe the fully-interacting system, it can help us approximate the fully-interacting system.

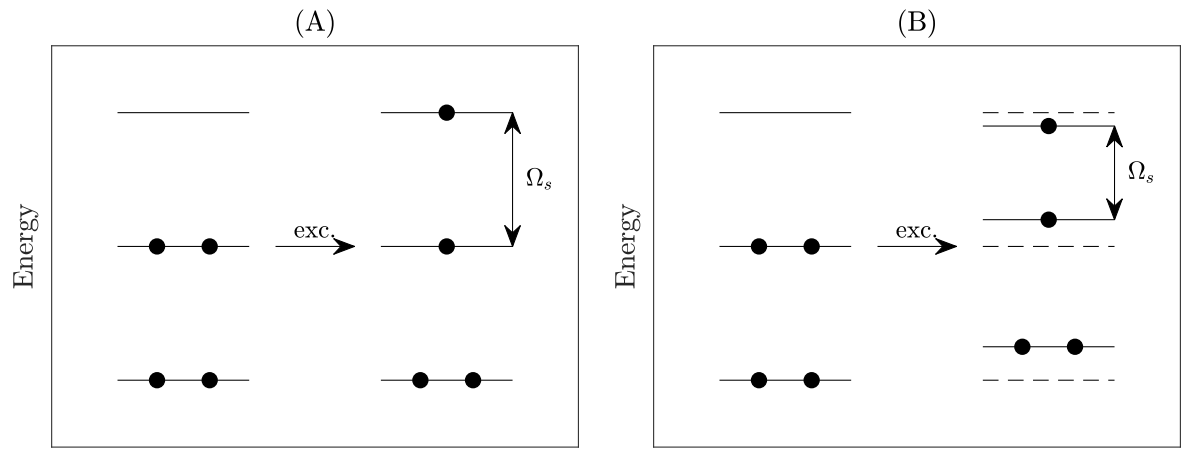

Figure 2.2: MO diagrams of two fictional molecular systems: (A) an independent-particle system and (B) a fully-interacting system. The orbitals are represented by horizontal bars and the electrons represented by dots. In the independent-particle system (A), the energy levels are unaffected by the excitation process. Consequently, the excitation energy Ω_s simply equates to the energy level difference. In the fully-interacting system (B), the original energy levels (dashed) are shifted as a result of the excitation process. Consequently, the excitation energy Ω_s does not equate to the pre-excitation energy level difference.

2.2.3 The Variational Principle

Instead of obtaining a full solution of the electronic Schrödinger equation (Equation 2.13), we could try finding part of the solution by imposing some constraints. Specifically, we can obtain the ground state wave function Ψ_0 and the ground state energies E_0 by imposing that the system energy $E_{\mathrm{el}}(\Psi) = \langle \Psi_{\mathrm{el}} | \hat{H}_{\mathrm{el}} | \Psi_{\mathrm{el}} \rangle$ is minimized:

$$\begin{aligned} \Psi_0 &= \mathrm{argmin}_{\Psi}\ E_{\mathrm{el}}(\Psi), \\ \text{s.t.} \quad \int \mathrm{d}^3\mathbf{r}\, |\Psi(\mathbf{r})|^2 &= 1. \end{aligned} \tag{2.19}$$

This is known as the variational principle. Even with the imposed constraints, solving the electronic Schrödinger equation (Equation 2.13) is difficult because of the electron-electron interactions. To proceed, we once again neglect all electron-electron interactions and approximate the wave function by the Hartree-Fock wave function Ψ_{HF} (Equation 2.18). The optimization problem of the Hartree-Fock independent-particle system is then given by:

$$\begin{aligned} \Psi_0 &= \mathrm{argmin}_{\Psi_{\mathrm{HF}}}\ E_{\mathrm{el}}(\Psi_{\mathrm{HF}}), \\ \text{s.t.} \quad \int \mathrm{d}^3\mathbf{r} \phi_i(\mathbf{r}_i)\phi_j(\mathbf{r}_j) &= \delta_{i,j}, \\ \int \mathrm{d}^3\mathbf{r}\, |\Psi_{\mathrm{HF}}(\mathbf{r})|^2 &= 1. \end{aligned} \tag{2.20}$$

The solution of this problem is given by a system of N (partial) functional derivatives:

$$\delta \langle \Psi_{\mathrm{HF}} | \hat{H}_{\mathrm{el}} | \Psi_{\mathrm{HF}} \rangle \big/ \delta\phi_i = 0, \qquad i = 1, 2, \ldots, N. \tag{2.21}$$

This system of functional derivatives yields the *Hartree-Fock* equations [15]:

$$[\hat{h}_i + V_{\mathrm{H}} + V_{\mathrm{X}}]\phi_i = \varepsilon_i^{\mathrm{HF}}\phi_i, \tag{2.22}$$

where $\varepsilon_i^{\mathrm{HF}}$ denotes the Hartree-Fock one-particle energy, V_{H} denotes the *Hartree potential* and V_{X} denotes the *exchange potential*:

$$V_{\mathrm{H},i} = \int \mathrm{d}^3\mathbf{r}' \sum_{i\neq j} |\phi_j(\mathbf{r}')|^2 \frac{1}{|\mathbf{r}-\mathbf{r}'|} = \int \mathrm{d}^3\mathbf{r}' \frac{\rho_j(\mathbf{r}')}{|\mathbf{r}-\mathbf{r}'|}, \tag{2.23}$$

$$V_{\mathrm{X}}\phi_i(\mathbf{r}) = \sum_j \int \mathrm{d}^3\mathbf{r}' \phi_j(\mathbf{r}') \frac{1}{|\mathbf{r}-\mathbf{r}'|} \phi_i(\mathbf{r}')\phi_j(\mathbf{r}). \tag{2.24}$$

The Hartree potential represents the classical electrostatic potential at position $\mathbf{r}_i'$, generated by the charge distribution $\rho(\mathbf{r})$. Important is to note that the Hartree-Fock independent-particle energies $\varepsilon_i^{\mathrm{HF}}$ now depend on the potentials $V_{\mathrm{H},i}$, which in turn depend on the variables $\phi_i(\cdot)$. The problem must therefore be solved self-consistently. This method for describing the ground state system is called the Hartree-Fock (HF) method, or alternatively the Self-Consistent Field (SCF) method.

2.3 Ground State Electron Density via DFT

In the previous section, we introduced the electronic wave function Ψ_{el}, of the N-electron system. We showed how we can approximate the ground state wave functions and energy levels of the molecular system using the HF method. Specifically, we varied the one-particle wave functions such that the system energy was minimized. In this section, we introduce the Density Functional Theory (DFT) method for describing the ground state system. Like the HF method, the DFT method also applies the variational principle. However, instead of varying one-particle wave functions, with DFT we vary the electron density of the system. We summarize important steps and approximations of the DFT method. A more thorough analysis of the method can be found in [16].

The electronic wave function quantifies the probability of finding the i-th electron at a given position $\mathbf{r}_i$, for $i = 1, 2, \ldots, N$. Since the electronic wave function is not an observable of the system, it cannot be measured. We can, however, measure the electron density $n(\mathbf{r})$, which is related to the electronic wave function Ψ via

$$n(\mathbf{r}) = N \int \mathrm{d}^3\mathbf{r}_2 \ldots \mathbf{r}_N \left|\Psi(\mathbf{r}, \mathbf{r}_2, \ldots, \mathbf{r}_N)\right|^2. \tag{2.25}$$

The electron density quantifies the probability of an electron occupying an infinitesimal element of space surrounding any given point $\mathbf{r}$. Since it only depends on 3 coordinates, the electron density is a much simpler quantity than the electronic wave function.

Naturally, the electrons arrange themselves such that the total energy of the system is minimized. DFT is based on this natural tendency to reach ground state. Specifically, if we

assume that the total energy of the system is a functional of the electron density, we can find the ground state electron density by solving the optimization problem

$$\frac{\delta E_0[n]}{\delta n}\Big|_{n=n_0} = 0. \tag{2.26}$$

The foundation of DFT was established by Hohenberg and Kohn [1], who proved that the total energy is a functional of the density. Furthermore, they proved that the ground state electron density is a minimizer of the total energy of the system.

The total energy is commonly split into four contributing factors:

$$E_0[n] = E_{\text{nuc}-\text{el}}[n] + T_{\text{el}}[n] + E_{\text{el}-\text{el}}[n] + E_{\text{XC}}[n]. \tag{2.27}$$

The functional forms of the classical electrostatic electron-nucleus $E_{\text{el}-\text{nuc}}$ and electron-electron (or Coulomb) $E_{\text{el}-\text{el}}$ interactions are known and given by:

$$E_{\text{el}-\text{nuc}}[n] = \frac{1}{2}\iint \mathrm{d}^3\mathbf{r}\mathrm{d}^3\mathbf{r}'\frac{n(\mathbf{r})n(\mathbf{r}')}{|\mathbf{r}-\mathbf{r}'|}, \tag{2.28}$$

$$E_{\text{el}-\text{el}}[n] = \int \mathrm{d}^3\mathbf{r}\hat{V}_{\text{nuc}-\text{el}}(\mathbf{r})n(\mathbf{r}'). \tag{2.29}$$

However, the kinetic energy $T_{\text{el}}[n]$ cannot be calculated from an electron density. Furthermore, the functional form of the exchange-correlation $E_{\text{XC}}[n]$ is not known. In order to proceed, we must rewrite the system such that $T_{\text{el}}[n]$ may be calculated. The $E_{\text{XC}}[n]$ term must be approximated.

In 1965, W. Kohn and L. Sham proposed an independent-particle model approach for dealing with the kinetic energy $T_{\text{el}}[n]$ [17]. They showed that the electron density for N interacting particles can be constructed from N non-interacting Kohn-Sham orbitals ϕ_i^{KS}:

$$n(\mathbf{r}) = \sum_{i=1}^{N} \left|\phi_i^{\text{KS}}(\mathbf{r})\right|^2. \tag{2.30}$$

The idea is that we transform the system of N interacting particles into a fictitious system of N non-interacting one-particle orbitals whose joint electron density is identical to the electron density of the original system. This fictitious system of non-interacting orbitals is also referred to as the Kohn-Sham (KS) system.

The kinetic energy functional $T_{\text{el}}[n]$ of the KS system is given by:

$$T_{\text{el}}[n] = -\frac{1}{2}\sum_{i=1}^{N}\int \mathrm{d}^3\mathbf{r}\phi_i^{\text{KS}}\nabla^2\phi_i^{\text{KS}}. \tag{2.31}$$

Since the kinetic energy is a function of ϕ_i^{KS} explicitly and no longer of n, we rewrite the optimization problem (Equation 2.26) accordingly:

$$\frac{\delta E_0[n]}{\delta \phi_i^{\text{KS}}}\Big|_{n=n_0} = 0, \qquad i = 1, 2, \ldots, N. \tag{2.32}$$

So, we are now required to solve N optimization problems, each corresponding to one independent particle. However, we cannot vary the set ϕ_i^{KS} freely. Since the normalized orbitals

ϕ_i^{KS} are supposed to be non-interacting, they must be orthonormal to each other:

$$\int \mathrm{d}^3\mathbf{r}\phi_i^{\mathrm{KS}}\phi_j^{\mathrm{KS}} = \delta_{i,j}, \qquad \delta_{i,j} = \begin{cases} 1 & \text{if } i = j, \\ 0 & \text{otherwise,} \end{cases} \tag{2.33}$$

where $\delta_{i,j}$ denotes the Kronecker delta. Each of the N optimization problems is now subject to N constraints that ensure orthonormality of the orbitals. We reformulate the constrained optimization problem using a Lagrange function with Lagrange multipliers $\epsilon_{i,j}$:

$$\frac{\delta}{\delta\phi_i^{\mathrm{KS}}}\left[E_0[n] - \sum_j^N \epsilon_{i,j}\left(\int \mathrm{d}^3\mathbf{r}\phi_i^{\mathrm{KS}}\phi_j^{\mathrm{KS}} - \delta_{i,j}\right)\right]\Bigg|_{n=n_0} = 0, \qquad i = 1, 2, \ldots, N. \tag{2.34}$$

Thus far, no approximations are made and the kinetic energy functional resulting from the Kohn-Shan system (Equation 2.31) is exact.

Unfortunately, the exact form of the exchange-correlation functional $E_{\mathrm{XC}}[n]$ is not known and it can only be approximated. As a result, all many-body complications in DFT stem from the exchange-correlation functional. Approximate functionals may be fitted to experimental data, e.g. B3LYP [18, 19], whereas others may interpolate between limiting cases where the exact functional is known, e.g. PBE [20]. While approximations exist that accurately calculate certain physical quantities, there is no go-to approximation which produces consistent results across the board [21]. We use PBE0 functionals, which have been shown to provide accurate excitation energies [22].

Once we have selected an approximate functional for the exchange-correlation, we can express all four energy contributions (Equation 2.27) in their functional form. We can now proceed with solving the optimization problem in Equation 2.34. Note that we are differentiating functionals with respect to the orbital function ϕ_i. Without derivation, the following equations for the Kohn-Sham orbitals are obtained [16]:

$$\left[-\frac{1}{2}\nabla^2 + \hat{V}_{\mathrm{nuc-el}} + V_H[n] + V_{\mathrm{XC}}[n]\right]\phi_i^{\mathrm{KS}} = \sum_j \epsilon_{i,j}\phi_j^{\mathrm{KS}}, \qquad i = 1, 2, \ldots, N. \tag{2.35}$$

We define the DFT Hamiltonian $\hat{H}^{\mathrm{DFT}}[n]$ as the left-hand side operator acting on the orbitals, which is Hermitian. We can look at this system of equations as a matrix equation:

$$\hat{H}^{\mathrm{DFT}}[n]\{\phi_i^{\mathrm{KS}}\} = \underline{\epsilon}\{\phi_i^{\mathrm{KS}}\}. \tag{2.36}$$

The left-hand side of this equation represents a Hermitian operator $\hat{H}^{\mathrm{DFT}}[n]$ acting on the orbitals $\{\phi_i^{\mathrm{KS}}\}$. The right-hand side matrix of Lagrange multipliers $\underline{\epsilon}$ must therefore also be Hermitian. Consequently, we can diagonalize $\underline{\epsilon} = \underline{\mathbf{U}}\underline{\epsilon}^{\mathrm{KS}}\underline{\mathbf{U}}^T$ using unitary transformation matrices leading to

$$\hat{H}^{\mathrm{DFT}}[n]\{\phi_i^{\mathrm{KS}}\} = \underline{\mathbf{U}}^T\underline{\epsilon}^{\mathrm{KS}}\underline{\mathbf{U}}\{\phi_i^{\mathrm{KS}}\} \;\Leftrightarrow\; \hat{H}^{\mathrm{DFT}}[n]\underline{\mathbf{U}}\{\phi_i^{\mathrm{KS}}\} = \underline{\epsilon}^{\mathrm{KS}}\underline{\mathbf{U}}\{\phi_i^{\mathrm{KS}}\},$$

effectively transforming the orbitals into $\{\phi_i^{\mathrm{KS}}\} := \underline{\mathbf{U}}\{\phi_i\}$. The resulting equation is known as the Kohn-Sham equation:

$$\hat{H}^{\mathrm{DFT}}[n]\phi_i^{\mathrm{KS}} = \epsilon_i^{\mathrm{KS}}\phi_i^{\mathrm{KS}}, \qquad i = 1, 2, \ldots, N. \tag{2.37}$$

This equation resembles the electronic Schrödinger equation (Equation 2.14). However, the orbitals ϕ_i^{KS} do not represent wave functions and the energies ϵ_i^{KS} do not represent physical energies. Instead, this equation describes the dynamics of the fictitious system of non-interacting orbitals. We note that the Hamiltonian H^{DFT} depends on the electron density n, which in turn depends on the Kohn-Sham wave functions ϕ_i^{KS}, which we are optimizing. Therefore, we can only solve this equation self-consistently, i.e. make a guess of the electron density n and solve for ϕ_i^{KS} from which a new density is constructed. This process is repeated until the electron density is converged within a certain tolerance.

In order to optimize ϕ_i^{KS}, we require a mathematical representation of it. However, wave functions are defined at an in infinite number of points and therefore cannot exist in a finite space such as the computer memory. In practice, $\phi_i^{\mathrm{KS}}(\mathbf{r})$ is expanded in a finite number of *basis functions* $\chi_j(\mathbf{r})$:

$$\phi_i^{\mathrm{KS}}(\mathbf{r}) = \sum_{j=1}^{N_{i,\chi}} X_{i,j}\chi_j(\mathbf{r}), \qquad i = 1, 2, \ldots, N. \tag{2.38}$$

Here, $X_{i,j} \in \mathbb{R}$ represents the relative weighting coefficient corresponding to the contribution of basis function χ_j to the full wave function ϕ_i^{KS}. We use atom-centered Gaussian Type Orbitals (GTOs), which offer computationally efficient integral evaluations [23]. These types of basis functions are of the form:

$$\chi(\mathbf{r}) = N_{l,\alpha} Y_{l,m}(v, \phi) r^l e^{-\alpha r^2}. \tag{2.39}$$

Every atom requires a distinct set of basis functions. A collection of basis functions which can describe the molecular system in its entirety is called a *basis set*. When selecting a suitable basis set, we make a trade-off between computation times and accuracy. By increasing the number of basis functions, we can more accurately describe the orbitals ϕ_i^{KS}, but we also increase the computational cost of our calculations.

2.4 Electronically Excited States via GW-BSE

In the previous section, we introduced the DFT method for computing the energy of a molecular system given its electron density. While DFT accurately predicts the ground state energies of molecules, it underestimates band gaps for most materials [3]. This error stems from the use of approximate exchange-correlation functionals. Now, we introduce the *GW*-BSE method. The GW-BSE method is built upon the ground state system established in the previous section, yet it yields more accurate excitation energies than DFT. In this thesis, we limit ourselves to the first step of the GW-BSE method: the GW method, which deals with calculating the self-energy (Equation 1.1).

We distinguish between two types of excitation processes: one-particle excitations and two-particle excitations. In one-particle excitations, a single electron is either added to or annihilated from the system. In two-particle excitations, one electron is created and one electron is annihilated. In the latter, the charge of the molecule remains unchanged. Two-particle excitation processes are therefore also referred to as neutral excitations. We summarize important steps and approximations of the *GW* method. A more detailed explanation of the method can be found in [16, 24, 25].

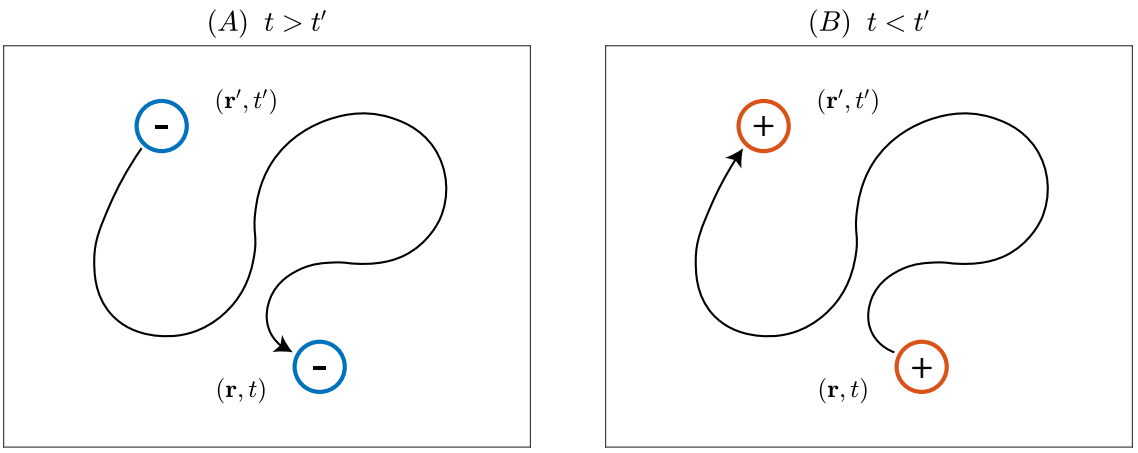

Figure 2.3: A visualization of the one-particle excitation process as described by the Green's function G. (A) $t > t'$: an electron is created at $(\mathbf{r}', t')$, propagates through the system and is annihilated at $(\mathbf{r}, t)$. (B) $t < t'$: a hole is created at $(\mathbf{r}', t')$, propagates through the system and is annihilated at $(\mathbf{r}, t)$.

2.4.1 One-Particle Excitations

One-particle excitations are processes in which one electron is temporarily added (created) or removed (annihilated) from the molecular system. We model these one-particle excitations as a sequence of three events: (1) the creation of an electron at $(\mathbf{r}', t')$, (2) its evolution from t' to t through the interacting many-body system and (3) its annihilation at $(\mathbf{r}, t)$. The annihilation of an electron is equivalent to the creation of a *hole*, i.e. the absence of an electron. Mathematically, we describe these events using operators in the Heisenberg picture.

First, let $|n, s\rangle$ denote the n-electron s^{th} excited state of the system and let $E_{n,s}$ denote the energy associated to this state. Acting on these states are the annihilation operator $\hat{\phi}(\mathbf{r}t)$, which annihilates one electron at $(\mathbf{r}, t)$, and the creation operator $\hat{\phi}^\dagger(\mathbf{r}t)$, which creates one electron at $(\mathbf{r}, t)$. The creation and annihilation operators are given by:

$$\hat{\phi}(\mathbf{r}t) = \exp(i\hat{H}t)\hat{\phi}(\mathbf{r}, 0)\exp(-i\hat{H}t). \tag{2.40}$$

These operators are governed by the Equation Of Motion (EOM) in the Heisenberg picture[4]:

$$i\frac{\partial}{\partial t}\hat{\phi}(\mathbf{r}t) = \left[\hat{\phi}(\mathbf{r}t), \hat{H}\right]. \tag{2.41}$$

The energies ε_s associated to these creation and annihilation processes follow from:

$$\begin{aligned}
\langle n, 0|\, \hat{\phi}^\dagger(\mathbf{r}t)\, |n+1, s\rangle &= \langle n, 0|\exp(i\hat{H}t)\hat{\phi}^\dagger(\mathbf{r}, 0)\exp(-i\hat{H}t)\, |n+1, s\rangle \\
&= \langle n, 0|\exp(iE_{n,0}t)\hat{\phi}^\dagger(\mathbf{r}, 0)\exp(-iE_{n+1,s}t)\, |n+1, s\rangle \\
&= \underbrace{\langle n, 0|\, \hat{\phi}^\dagger(\mathbf{r}, 0)\, |n+1, s\rangle}_{=:f_s(\mathbf{r})} \exp\Big[-i\underbrace{(E_{n+1,s} - E_{n,0})}_{=:\varepsilon_s}t\Big].
\end{aligned} \tag{2.42}$$

[4]In group theory, $[f, g]$ denotes the commutator of elements f and g of a group G.

The full one-particle excitation process is described by the one-particle Green's function (see Figure 2.3), which is defined as:

$$iG(\mathbf{r}t, \mathbf{r}'t') = \begin{cases} \langle n, 0 | \, \hat{\phi}(\mathbf{r}t)\hat{\phi}^\dagger(\mathbf{r}t) \, | n, 0 \rangle & t > t' \quad \text{creation} \rightarrow \text{annihilation} \\ \langle n, 0 | \, \hat{\phi}^\dagger(\mathbf{r}t)\hat{\phi}(\mathbf{r}t) \, | n, 0 \rangle & t' > t \quad \text{annihilation} \rightarrow \text{creation} \end{cases} . \tag{2.43}$$

For now, we only consider $t > t'$, i.e. creation followed by annihilation (Figure 2.3 (A)). By combining Equations 2.42, 2.43 and subsequently doing a Fourier transform ($(t - t') \rightarrow \omega$), we can derive the so-called *Lehman expression* of the one-particle Green's function:

$$G_1(\mathbf{r}, \mathbf{r}', \omega) = \sum_v^{N_v} \frac{\phi_v(\mathbf{r})\phi_v(\mathbf{r}')}{\omega - \varepsilon_v - i\eta} + \sum_c^{N_c} \frac{\phi_c(\mathbf{r})\phi_c(\mathbf{r}')}{\omega - \varepsilon_c + i\eta}. \tag{2.44}$$

Here, index v runs over the occupied (valence) states and index c runs over the unoccupied (conduction) states. The "small" parameter $\eta \rightarrow 0^+$ ensures that integrals over the Green's function converge. The poles of the Green's function correspond to the desired creation and annihilation energies: ε_c, ε_v. If we can relate the one-particle Green's function to our molecular system, we can compute these energies.

the one-particle Green's function G_1 satisfies the Equation of Motion (EOM) for the Green's function:

$$\left[\frac{\partial}{\partial t} - \hat{h}\right] G_1(\mathbf{r}t, \mathbf{r}'t') + i \int \mathrm{d}^3\mathbf{r}'' v(\mathbf{r}, \mathbf{r}'') G_2(\mathbf{r}''t, \mathbf{r}'t', \mathbf{r}t) = \delta(\mathbf{r} - \mathbf{r}')\delta(t - t'). \tag{2.45}$$

Here, δ denotes the Dirac delta function and $\hat{h}$ denotes the one-particle Hamiltonian (Equation 2.15). Without going into detail, it is important to note that this equation contains both the one-particle Green's function G_1 and the two-particle Green's function G_2. This continues for higher order Green's functions as well and leads to an infinite system of equations. In order to obtain a closed system of equations, from which we can obtain G_1, we introduce the *self-energy* operator $\Sigma(\mathbf{r}t, \mathbf{r}''t'')$ via

$$i \int \mathrm{d}^3\mathbf{r}'' v(\mathbf{r}', \mathbf{r}'') G_2(\mathbf{r}''t, \mathbf{r}'t', \mathbf{r}t) = - \int \mathrm{d}^3\mathbf{r}'' \mathrm{d}t'' \Sigma(\mathbf{r}t, \mathbf{r}''t'') G_1(\mathbf{r}t, \mathbf{r}'t'). \tag{2.46}$$

Substitution of Equation 2.46 into Equation 2.45 yields

$$\left[\frac{\partial}{\partial t} - \hat{h}\right] G_1(\mathbf{r}t, \mathbf{r}'t') - \int \mathrm{d}^3\mathbf{r}'' \mathrm{d}t'' \Sigma(\mathbf{r}t, \mathbf{r}''t'') G_1(\mathbf{r}t, \mathbf{r}'t') = \delta(\mathbf{r} - \mathbf{r}')\delta(t - t'). \tag{2.47}$$

We can obtain an expression for Σ by solving a closed set of coupled equations known as

Hedin's equations [26]:

$$\Sigma(1,2) = i \int \mathrm{d}34 G_1(1,3) W(1,4) \Gamma(4,2,3), \tag{2.48a}$$

$$\Gamma(1,2,3) = \delta(1,2)\delta(1,3) + \int \mathrm{d}4567 \frac{\partial \Sigma(1,2)}{\partial G_1(4,5)} G_1(4,6) G_1(5,7) \Gamma(6,7,3), \tag{2.48b}$$

$$\chi(1,2) = -i \int \mathrm{d}34 G_1(1,3) G_1(4,1) \Gamma(3,4,2), \tag{2.48c}$$

$$\epsilon(1,2) = \delta(1,2) - \int \mathrm{d}3 v(1,3) \chi(3,2), \tag{2.48d}$$

$$W(1,2) = \int \mathrm{d}3 \epsilon^{-1}(1,3) v(3,2). \tag{2.48e}$$

The notation is simplified by combining the space and frequency variables into a single variable, i.e. $\mathbf{r}t \equiv 1$ and $\mathbf{r}'t' \equiv 2$, or $\mathbf{r}, \mathbf{r}', \omega \equiv 1, 2$ and $\mathbf{r}, \mathbf{r}', \mathbf{r}'', \omega \equiv 1, 2, 3$. Here, Γ is the vertex correction, χ the reducible polarizability, ϵ the dielectric function and W the screened Coulomb interaction. Furthermore, δ denotes the Kronecker delta and $v = |\mathbf{r} - \mathbf{r}'|^{-1}$ denotes the Coulomb interaction. The polarizability of a molecule is the tendency of its electron cloud to be distorted by an external electric field. The dielectric function ϵ describes the response of the system to the electric screening field. The screened-Coulomb interaction W describes the electron-electron interactions v of the many-electron system. In practice, solving this system is impossible. The vertex correction Γ is particularly complicated as it is given by recursive relation, containing a fourth degree integral and a functional derivative. To proceed, we simplify the system by making two important approximations.

The first approximation is the GW approximation, which assumes that the expansion of the self-energy Σ in terms of the Green's function G_1 can be truncated after the first term. This is achieved by setting $\Gamma(1,2,3) = \delta(1,2)\delta(1,3)$. Substituting this into Equations 2.48a to 2.48e yields

$$\Sigma(1,2) = iG_1(1,2)W(1,2), \tag{2.49a}$$

$$P(1,2) = -iG_1(1,2)G_1(2,1), \tag{2.49b}$$

$$\epsilon(1,2) = \delta(1,2) - \textstyle\int \mathrm{d}3 v(1,3)\chi(3,2), \tag{2.49c}$$

$$W(1,2) = \textstyle\int \mathrm{d}3 \epsilon^{-1}(1,3) v(3,2). \tag{2.49d}$$

The self-energy simplifies to $\Sigma(1,2) = iG_1(1,2)W(1,2)$ (hence the name GW approximation). Furthermore, the reducible polarizability χ simplifies to the irreducible polarizability $P = iG(1,2)G(2,1)$. This simplification of the polarizability corresponds to the Random Phase Approximation (RPA). In the RPA setting, electron-hole pair react with each other and the remaining electronic system as being non-interacting.

The second approximation is the Quasi-Particle (QP) approximation, which assumes that the excitation of a many-body system of interacting particles can be described by a single *quasi-particle*. The quasi-particle can be thought of as a real particle within a cloud of screening particles. The coulomb interactions ν between all electrons in the system are modeled by a screened Coulomb interaction $W = \epsilon^{-1} v$ of the quasi-particle with itself (see Figure 2.4). The

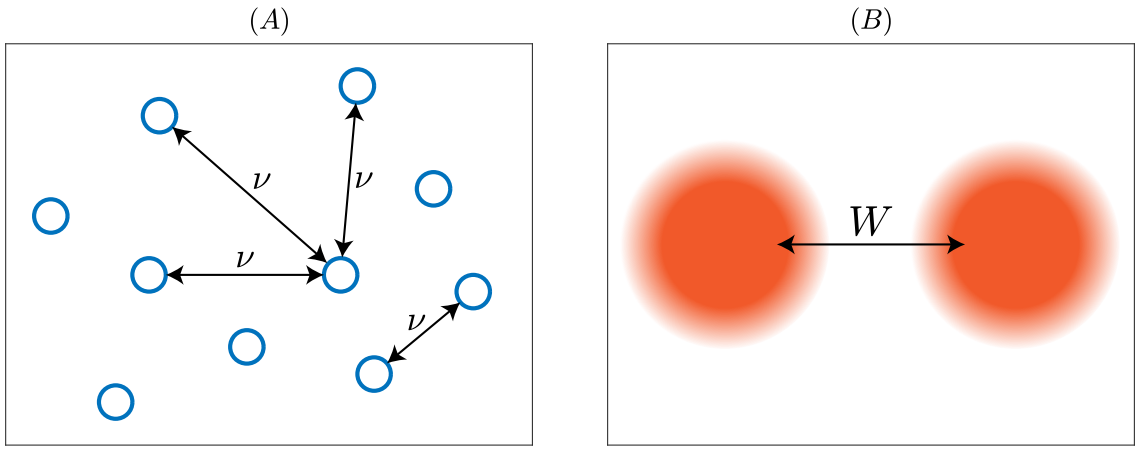

Figure 2.4: (A) The many-electron system of interacting particles. The particles interact with each other through Coulomb interactions ν. (B) The quasi-particle. The coulomb interactions ν between all electrons in the system are modeled by a screened Coulomb interaction $W = \epsilon^{-1}v$ of the quasi-particle with itself.

excited system now only contains one particle: the quasi-particle. The total energy of this system equals the energy of this quasi-particle and is called the Quasi-Particle (QP) energy ε_{QP}. From the QP energies, we can obtain the desired creation and annihilation energies. The QP energies are defined as the poles of G_1 as shown in Equation 2.44.

We can visualize the QP approximation using the spectral function $A(\omega)$ (see Figure 2.5). The spectral function is related to the photoemission spectrum of the molecule; its peaks represent excitations. Introducing the quasi-particle, the spectral function is decomposed in a coherent and an incoherent part:

$$A(\omega) = Z_{\text{QP}} A_{\text{coh}}(\omega) + (1 - Z_{\text{QP}}) A_{\text{incoh}}(\omega). \tag{2.50}$$

The quasi-particle only accounts for the coherent part of the spectral function. The incoherent part may contribute satellite peaks to the full spectral function, but these peaks are neglected by the quasi-particle approximation. The weight of the coherent part Z_{QP} is called the Quasi-Particle (QP) weight and is defined as:

$$Z_{\text{QP}} := \left(1 - \frac{\mathrm{dRe}[\Sigma(\omega)]}{\mathrm{d}\omega}\bigg|_{\omega=\varepsilon_{\text{QP}}}\right)^{-1} \in [0, 1]. \tag{2.51}$$

Note that the QP weight is defined as the sum of the zeroth and first order terms of a Taylor expansion of the spectral function around $\omega = \varepsilon_{QP}$. The QP approximation holds when the quasi-particle resembles the real system, i.e. the excitations must have long lifetimes: $\mathrm{Im}(\Sigma_c) \to 0$, and there must be little to no satellite peaks: $(1 - Z_{QP}) \to 0$. Note that decreasing the "small" parameter η (Equation 2.44) will decrease $\mathrm{Im}(\Sigma)$ and therefore also decrease the error of the QP approximation.

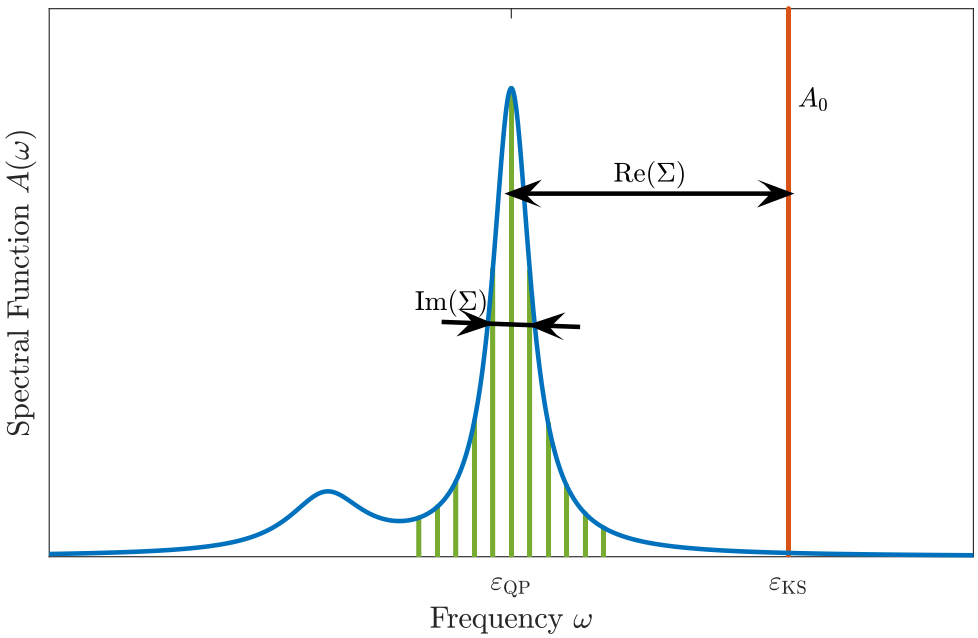

Figure 2.5: In the non-interacting system (e.g. the KS system), the spectral function consists of δ-peaks (red) at the KS energies. However, in the real interacting system, the particles rearrange in reaction to the excitation. In the spectral function, this is reflected by a separation of the δ-peaks into smaller and shifted peaks (green), each corresponding to an excited state with a different electron arrangement. The spectral function then becomes a continuum, collecting the peaks under Lorentzian curves (blue). Introducing the quasi-particle, the spectral function is decomposed in a coherent and an incoherent part. The coherent part is centered around the quasi-particle energy $\varepsilon_{\mathrm{QP}}$ and has a Lorentzian shape. Its shift from the non-interacting energy is proportional to Re[Σ] and its Full Width at Half Maximum (FWHM) is proportional to Im[Σ]. The lifetime of the quasi-particle is inversely proportional to the peak width. The incoherent part may include satellite peaks, but is neglected by the quasi-particle approximation.

In order to obtain the QP energies, we relate them to the self-energy. First, we generalize $\omega \in \mathbb{R} \to z \in \mathbb{C}$ and rewrite the Green's function (Equation 2.44) into its spectral representation:

$$G_1(\mathbf{r}, \mathbf{r}', z) = \sum_i^{N_{\mathrm{MO}}} \frac{\psi_i(\mathbf{r}, z)\bar{\psi}_i(\mathbf{r}', z)}{z - E_i(z)}. \tag{2.52}$$

Here, $\psi_i(\mathbf{r}, z)$ and $\bar{\psi}_i(\mathbf{r}', z)$ respectively denote the right and left eigenvectors of the Hamiltonian $\hat{H} = \hat{h}_0 + \Sigma(\mathbf{r}', \mathbf{r}, z)$ and $E_i(z)$ the corresponding eigenvalues. Substitution of Equation 2.52 into the EOM (Equation 2.45) yields the following relation between the self-energy Σ and the energy z [24]:

$$\hat{h}_0\psi_i(\mathbf{r}, z) + \int \mathrm{d}^3\mathbf{r}'\Sigma(\mathbf{r}, \mathbf{r}', z)\psi_i(\mathbf{r}', z) = E_i(z)\psi_i(\mathbf{r}, z). \tag{2.53}$$

Recall that the QP energies are defined as the poles of the Green's function: $\varepsilon_i^{\mathrm{QP}} - E_i(\varepsilon_i^{\mathrm{QP}})$. Substitution of $z = \varepsilon_i^{\mathrm{QP}}$, rewriting $\psi_i^{\mathrm{QP}}(\mathbf{r}) \equiv \psi_i(\mathbf{r}, z = \varepsilon_i^{\mathrm{QP}})$ and collecting all terms in the

integral yields:

$$\int \mathrm{d}^3\mathbf{r}' \left[\delta(\mathbf{r},\mathbf{r}')\hat{h}_0\psi_i^{\mathrm{QP}}(\mathbf{r}) + \Sigma(\mathbf{r},\mathbf{r}',\varepsilon_i^{\mathrm{QP}})\psi_i^{\mathrm{QP}}(\mathbf{r}')\right] = \int \mathrm{d}^3\mathbf{r}' \left[\delta(\mathbf{r},\mathbf{r}')E_i(z)\psi_i^{\mathrm{QP}}(\mathbf{r})\right], \quad (2.54)$$

or alternatively, in bra-ket notation and only considering the diagonals:

$$\left[\hat{h}_0 + \Sigma(\varepsilon_i^{\mathrm{QP}})\right] |\phi_i^{\mathrm{QP}}\rangle = \varepsilon_i^{\mathrm{QP}} |\phi_i^{\mathrm{QP}}\rangle . \quad (2.55)$$

We solve this equation using a perturbative approach. We approximate the orbitals and Hamiltonian of the QP system by those of the KS system, i.e.

$$|\phi_i^{\mathrm{QP}}\rangle \approx |\phi_i^{\mathrm{KS}}\rangle , \qquad \hat{h}_0 \approx \hat{h}_0^{\mathrm{DFT}} = \hat{H}^{\mathrm{DFT}} - \hat{V}_{\mathrm{XC}}, \qquad \varepsilon_i^{\mathrm{KS}} = \langle\phi_i^{\mathrm{KS}}| \hat{H}^{\mathrm{DFT}} |\phi_i^{\mathrm{KS}}\rangle . \quad (2.56)$$

Substituting this into Equation 2.55 and left multiplying with the KS orbitals yields the QP equation:

$$\varepsilon_i^{\mathrm{QP}} = \varepsilon_i^{\mathrm{KS}} + \langle\phi_i^{\mathrm{KS}}| \Sigma(\varepsilon_i^{\mathrm{QP}}) - \hat{V}_{\mathrm{XC}} |\phi_i^{\mathrm{KS}}\rangle . \quad (2.57)$$

This equation relates the self-energy Σ to the QP energies $\varepsilon_i^{\mathrm{QP}}$. Once the self-energy Σ is calculated via Equations 2.49a to 2.49d, we can use this relation to find the QP energies $\varepsilon_i^{\mathrm{QP}}$. Note that the QP energies equal the KS energies plus an additional correction term. Furthermore, the self-energy is evaluated at the QP energy, which means that Equation 2.57 must be solved self-consistently.

Before we proceed, we discuss the problem of self-consistency. We note that the computation of the self-energy requires input in the form of MO energies. We pass these energies ε as a parameter, i.e. $\Sigma(\omega) = \Sigma(\varepsilon;\omega)$. The self-energy on the right-hand side in Equation 2.57 is evaluated as $\Sigma(\varepsilon_{\mathrm{QP}};\varepsilon_{\mathrm{QP}})$. In a first attempt, we can set the input energies to the Kohn-Sham energies obtained through DFT calculations: $\Sigma(\varepsilon_{\mathrm{QP}};\varepsilon_{\mathrm{QP}}) \approx \Sigma(\varepsilon_{\mathrm{KS}};\varepsilon_{\mathrm{QP}})$. For the next iterations, we can use the previously obtained QP energy. Symbolically:

$$\begin{aligned}
1: &\quad \varepsilon_{\mathrm{QP}}^{(1)} = \varepsilon_{\mathrm{KS}} + \langle\phi_{\mathrm{KS}}| \Sigma(\varepsilon_{\mathrm{KS}};\varepsilon_{\mathrm{QP}}^{(1)}) - \hat{V}_{\mathrm{XC}} |\phi_{\mathrm{KS}}\rangle ; \\
2: &\quad \varepsilon_{\mathrm{QP}}^{(2)} = \varepsilon_{\mathrm{KS}} + \langle\phi_{\mathrm{KS}}| \Sigma(\varepsilon_{\mathrm{QP}}^{(1)};\varepsilon_{\mathrm{QP}}^{(2)}) - \hat{V}_{\mathrm{XC}} |\phi_{\mathrm{KS}}\rangle ; \\
&\vdots \\
k: &\quad \varepsilon_{\mathrm{QP}}^{(k)} = \varepsilon_{\mathrm{KS}} + \langle\phi_{\mathrm{KS}}| \Sigma(\varepsilon_{\mathrm{QP}}^{(k-1)};\varepsilon_{\mathrm{QP}}^{(k)}) - \hat{V}_{\mathrm{XC}} |\phi_{\mathrm{KS}}\rangle .
\end{aligned} \quad (2.58)$$

We refer to these iterations as GW iterations. If we terminate the this process after the first iteration, we obtain the unconverged QP energies $\varepsilon_{\mathrm{QP}}^{(1)}$. This approach is called G_0W_0, or one-shot GW. If we continue this process N times such that

$$|\varepsilon_{\mathrm{QP}}^{(N)} - \varepsilon_{\mathrm{QP}}^{(N-1)}| < \epsilon, \quad (2.59)$$

where ϵ denotes the desired tolerance, we obtain the converged QP energies $\varepsilon_{\mathrm{QP}}^{(N)}$. This approach is called $evGW$. While $evGW$ provides the QP energies up to desired precision, G_0W_0 provides a good estimate of the QP energies at lower computational cost.

2.4.2 Two-Particle Excitations

Two-particle excitations are processes in which one electron is created and one electron is annihilated, such that the total number of electrons remains unchanged. These excitations are therefore also called neutral excitations. We model these neutral excitation processes in the framework of Green's functions. Recall that in the previous section we simplified Hedin's equation by applying the GW approximation. The reducible polarizability χ was simplified to the irreducible polarizability P. This simplification of the polarizability corresponds to the Random Phase Approximation (RPA). In the RPA setting, the electron-hole pair react with each other and the remaining electronic system as being non-interacting. However, this electron-hole interaction is exactly what we need in order to model two-particle excitations.

In order to describe two-particle excitations, we extend the two-point Green's function to the four-point Green's function, systematically describing all possible neutral excitations. This form is known as the two-particle correlation function:

$$L(12,1'2') = -G_2(12,1'2') + G_1(1,2)G_1(1',2'). \tag{2.60}$$

It satisfies the Dyson-like, Bethe-Salpeter Equation (BSE):

$$L(12,1'2') = L_0(12,1'2') + \int \mathrm{d}3456 L_0(14,1'3)K(35,46)L(62,52'). \tag{2.61}$$

Here, $L_0(12,1'2') = G_1(1,2')G_1(2,1')$ denotes the non-interacting two-particle correlation function and K denotes the interaction kernel. We assume that both one-particle excitation processes occur simultaneously at time t. The time dependence can therefore be reduced: $L(12,1'2') \equiv L(\mathbf{r}_1,\mathbf{r}_2,\mathbf{r}_1',\mathbf{r}_2',t)$.

The non-interacting two-particle correlation function L_0 describes a neutral excitation process in a non-interacting system. We can retrieve the irreducible polarizability by evaluating:

$$P(\mathbf{r}_1,\mathbf{r}_2,\omega) = -iL_0(\mathbf{r}_1,\mathbf{r}_2;\mathbf{r}_1,\mathbf{r}_2;\omega). \tag{2.62}$$

The two-particle correlation function L describes a neutral excitation process in a fully-interacting system. We obtain the reducible polarizability by evaluating:

$$\chi(\mathbf{r}_1,\mathbf{r}_2,\omega) = -iL(\mathbf{r}_1,\mathbf{r}_2;\mathbf{r}_1,\mathbf{r}_2;\omega). \tag{2.63}$$

Thus, in order to model two-particle excitations, we replace the irreducible polarizability P in Equation 2.49b with the reducible polarizability χ, which follows from the Equation 2.61. Besides this modification of the polarizability, the QP energies follow from solving the QP equation, as explained in the previous section.

So far, we only considered the QP energies, not the two-particle excitation energies. The QP energies can be thought of as the energy required to create or annihilate a single electron in the MO. However, the QP energies are not physical, i.e. we cannot relate them to real-world measurements. The two-particle excitation energies, on the other hand, are physical and can be related to singlet/triplet excitation energies of the molecule. The two-particle excitation energies follow from the BSE method.

Chapter 3

Methodology

In the previous chapter, we provided the background theory for the three-step DFT-GW-BSE procedure. To arrive at the desired Quasi-Particle (QP) energies, we must perform two steps: (1) solve Hedin's equations (Equations 2.49a to 2.49d) to obtain the self-energy Σ and (2) solve the QP equation (Equation 2.57) to obtain the QP energies ε_{QP}.

The self-energy operator Σ is given by the GW convolution: $\Sigma = GW$. Here, G denotes the Green's function and W denotes the screened-Coulomb interaction. Recall that the screened-Coulomb interaction W describes the electron-electron interactions v of the many-electron system: $W = \epsilon^{-1}v$. Here v denotes the bare Coulomb interaction and ϵ denotes the dielectric function. The dielectric function describes the response of the system to the electric screening field: $\epsilon = 1 - v\chi$. Here χ denotes the reducible polarizability. The polarizability of a molecule is its ability to form dipoles in reaction to an electric field. The reducible polarizability is computed by solving the BSE.

In this chapter, we discuss the methodology behind the GW step. First, we calculate the reducible polarizability, which we need to evaluate the screened Coulomb interaction W. Next, we discuss an analytical method and an approximate method for computing the self-energy Σ. Once we have an expression for the self-energy, we compute the QP energies by numerically solving the QP equation.

3.1 Polarizability

We introduced the reducible polarizability χ (Equation 2.48c) and the irreducible polarizability P (Equation 2.49b). Via the GW approximation, the reducible polarizability χ was simplified to its irreducible counterpart P. However, in order to model two-particle excitations, we need to re-introduce the reducible polarizability χ. We achieve this by extending the one-particle correlation function L_0 to the two-particle correlation function L. Then, the irreducible polarizability P follows from Equation 2.62 and the reducible polarizability χ follows from Equation 2.63. In this section, we calculate the irreducible polarizability P and the reducible polarizability χ.

3.1.1 Irreducible Polarizability

The irreducible polarizability P is given by Equation 2.62. In order to draw conclusions for the interacting system, we extend it from a two-point quantity to a four-point quantity:

$$P(12,1'2') = -iG_1(1,2')G_1(2,1'). \tag{3.1}$$

We express the polarizability in the Lehman representation. We start with a Fourier transform to the frequency domain. The product of the one-particle green's functions in the time-domain results in a convolution in the Fourier domain:

$$P(\mathbf{r}_1,\mathbf{r}_2;\mathbf{r}_1',\mathbf{r}_2';\omega) = -\frac{i}{2\pi}\int \mathrm{d}\omega'\, G_1(\omega+\omega')G_1(\omega). \tag{3.2}$$

Substitution of the Lehman representation of the one-particle Green's function G_1 (Equation 2.44) yields:

$$P(\mathbf{r}_1,\mathbf{r}_2;\mathbf{r}_1',\mathbf{r}_2';\omega) = -\frac{i}{2\pi}\sum_{vc}\int \mathrm{d}\omega' I(\mathbf{r}_1,\mathbf{r}_2;\mathbf{r}_1',\mathbf{r}_2';\omega), \tag{3.3}$$

where

$$\begin{aligned} I(\mathbf{r}_1,\mathbf{r}_2;\mathbf{r}_1',\mathbf{r}_2';\omega) = \quad & \left(\frac{\mathbb{1}\{c=0\}\cdot\phi_v(\mathbf{r})\phi_v(\mathbf{r}')}{\omega+\omega'-\varepsilon_v-i\eta} + \frac{\mathbb{1}\{v=0\}\cdot\phi_c(\mathbf{r})\phi_c(\mathbf{r}')}{\omega+\omega'-\varepsilon_c+i\eta}\right) \\ & \times\left(\frac{\mathbb{1}\{c=0\}\cdot\phi_v(\mathbf{r})\phi_v(\mathbf{r}')}{\omega'-\varepsilon_v-i\eta} + \frac{\mathbb{1}\{v=0\}\cdot\phi_c(\mathbf{r})\phi_c(\mathbf{r}')}{\omega'-\varepsilon_c+i\eta}\right). \end{aligned} \tag{3.4}$$

The integral can be evaluated analytically on the complex plane using complex contour deformation theory [24]. We give a brief overview of contour deformation theory in Appendix A.1. Performing this integration yields:

$$P(\mathbf{r}_1,\mathbf{r}_2,\mathbf{r}_1',\mathbf{r}_2',\omega) = \sum_{vc}\left[\frac{\phi_c(\mathbf{r}_1)\phi_v(\mathbf{r}_2)\phi_v^*(\mathbf{r}_1')\phi_c^*(\mathbf{r}_2')}{\omega-(\varepsilon_c-\varepsilon_v)+i\eta} - \frac{\phi_v(\mathbf{r}_1)\phi_c(\mathbf{r}_2)\phi_c^*(\mathbf{r}_1')\phi_v^*(\mathbf{r}_2')}{\omega+(\varepsilon_c-\varepsilon_v)-i\eta}\right]. \tag{3.5}$$

3.1.2 Reducible Polarizability

The reducible polarizability χ is given by Equation 2.63. In order to compute it, we must evaluate the two-particle correlation, which is defined as:

$$L(12,1'2') = -G_2(12,1'2') + G_1(12)G_1(1'2') \tag{3.6}$$

and satisfies the Dyson-like, Bethe-Salpeter Equation (BSE):

$$L(12,1'2') = L_0(12,1'2') + \int \mathrm{d}3456 L_0(14,1'3)K(35,46)L(62,52'). \tag{3.7}$$

Here, $L_0(12,1'2') = G_1(1,1')G_1(2,2')$ denotes the non-interacting two-particle correlation function and K denotes the interaction kernel. We assume that both one-particle excitation processes occur simultaneously at time t. The time dependence can therefore be reduced: $L(12,1'2') \equiv L(\mathbf{r}_1,\mathbf{r}_2,\mathbf{r}_1',\mathbf{r}_2',t)$.

To simplify the mathematical formulation, we introduce the so-called *transition space* as product basis of one-particle wave functions. Any four-point quantity $f(x_1, x_2; x_3, x_4; \omega) \in \mathbb{C}$ can be transformed to this basis as follows:

$$f(x_1, x_2; x_3, x_4; \omega) = \sum_{n_1,n_2,n_3,n_4} \phi_{n_1}(x_1)\phi^*_{n_2}(x_2)[\underline{\mathbf{f}}(\omega)]^{n_3,n_4}_{n_1,n_2}\phi_{n_3}(x_3)\phi^*_{n_4}(x_4), \tag{3.8}$$

where the matrix $\underline{\mathbf{f}}(\omega) \in \mathbb{C}^{N^2_{\mathrm{MO}} \times N^2_{\mathrm{MO}}}$ is given by:

$$[\underline{\mathbf{f}}(\omega)]^{n_3,n_4}_{n_1,n_2} = \int \mathrm{d}x_1\mathrm{d}x_2\mathrm{d}x_3\mathrm{d}x_4 \; \phi_{n_1}(x_1)\phi^*_{n_2}(x_2)f(x_1, x_2; x_3, x_4; \omega)\phi_{n_3}(x_3)\phi^*_{n_4}(x_4). \tag{3.9}$$

The indices $n_1, n_2, n_4, n_1 \in \{1, 2, \ldots, N_{\mathrm{MO}}\}$ run over the MOs. The two dimensions of the matrix $\underline{\mathbf{f}}$ correspond to the transitions $n_1 \to n_2$ and $n_3 \to n_4$. Note that all matrices in this representation are Hermitian, i.e. $\underline{\mathbf{f}} = \underline{\mathbf{f}}^*$. Using this basis, we can rewrite Equation 3.7 as a matrix equation:

$$\underline{\mathbf{L}}(\omega) = \underline{\mathbf{L}}_0(\omega) + \underline{\mathbf{L}}_0(\omega)\underline{\mathbf{K}}(\omega)\underline{\mathbf{L}}(\omega). \tag{3.10}$$

The non-interacting correlation L_0 (Equation 3.5) is transformed to this basis:

$$[-i\underline{\mathbf{L}}_0(\omega)]^{n_3,n_4}_{n_1,n_2} = (\delta_{n_1,v} - \delta_{n_2,v}) \cdot \frac{\delta_{n_1,n_3} \cdot \delta_{n_2,n_4}}{\Delta\varepsilon_{n_2,n_1} - \omega}. \tag{3.11}$$

Otherwise, in matrix representation:

$$-i\underline{\mathbf{L}}_0(\omega) = \begin{array}{c} n_1n_2 \backslash n_3n_4 \\ vv \\ cc \\ vc \\ cv \end{array} \begin{array}{c} \begin{array}{cccc} vv & cc & vc & cv \end{array} \\ \begin{bmatrix} 0 & 0 & 0 & 0 \\ 0 & 0 & 0 & 0 \\ 0 & 0 & \frac{1}{\Delta\varepsilon_{n_2,n_1} - \omega} & 0 \\ 0 & 0 & 0 & \frac{-1}{\Delta\varepsilon_{n_2,n_1} - \omega} \end{bmatrix} \end{array}. \tag{3.12}$$

In this basis, $-i\underline{\mathbf{L}}_0$ is diagonal: $n_1 = n_3$, $n_2 = n_4$. We limit ourselves to the subspace of resonant ($v \to c$) and anti-resonant ($c \to v$) transitions:

$$-i\underline{\mathbf{L}}_0(\omega) \in \mathbb{C}^{N^2_{\mathrm{MO}} \times N^2_{\mathrm{MO}}} \;\to\; -i\underline{\mathbf{L}}_0(\omega) \in \mathbb{C}^{2N_t \times 2N_t}, \tag{3.13}$$

where $N_t := N_v \cdot N_c$. Finally, we introduce the occupation matrix $\underline{\mathbf{F}}$ such that

$$-i\underline{\mathbf{L}}_0 = -i\tilde{\underline{\mathbf{L}}}_0 \cdot \underline{\mathbf{F}} = \underbrace{\begin{bmatrix} (\Delta\varepsilon_{n_2,n_1} - \omega)^{-1} & 0 \\ 0 & (\Delta\varepsilon_{n_2,n_1} - \omega)^{-1} \end{bmatrix}}_{=:-i\tilde{\underline{\mathbf{L}}}_0 \in \mathbb{C}^{2N_t \times 2N_t}} \cdot \underbrace{\begin{bmatrix} 1 & 0 \\ 0 & -1 \end{bmatrix}}_{=:\underline{\mathbf{F}} \in \mathbb{C}^{2N_t \times 2N_t}}, \tag{3.14}$$

with the matrix elements given by:

$$[-i\tilde{\underline{\mathbf{L}}}_0]^{n_3,n_4}_{n_1,n_2} = \delta_{n_1,n_3}\delta_{n_2,n_4} \cdot (\Delta\varepsilon_{n_2,n_1} - \omega)^{-1} \tag{3.15}$$

$$[\underline{\mathbf{F}}]^{n_3,n_4}_{n_1,n_2} = \delta_{n_1,n_3}\delta_{n_2,n_4} \cdot (\delta_{n_1,v} - \delta_{n_2,v}). \tag{3.16}$$

We have rewritten the BSE (Equation 3.10) in terms of the transition space. Next, we solve this equation for the two-particle correlation function $\underline{\mathbf{L}}$. First, we separate $\underline{\mathbf{L}}$:

$$\begin{aligned} -i\underline{\mathbf{L}}(\omega) &= -i\underline{\tilde{\mathbf{L}}}_0(\omega)\underline{\mathbf{F}} - i\underline{\tilde{\mathbf{L}}}_0(\omega)\underline{\mathbf{FK}}(\omega)\underline{\mathbf{L}}(\omega) \\ &= \left[1 + i\underline{\tilde{\mathbf{L}}}_0(\omega)\underline{\mathbf{FK}}(\omega)\right]^{-1} \cdot -i\underline{\tilde{\mathbf{L}}}_0(\omega)\underline{\mathbf{F}} \\ &= \left[-i\underline{\tilde{\mathbf{L}}}_0^{-1}(\omega) - i\underline{\mathbf{FK}}(\omega)\right]^{-1}\underline{\mathbf{F}}. \end{aligned} \tag{3.17}$$

Since $-i\underline{\tilde{\mathbf{L}}}_0^{-1}$ (Equation 3.15) is diagonal, its inverse is given by:

$$-i\underline{\tilde{\mathbf{L}}}_0^{-1}(\omega) = \begin{bmatrix} \Delta\varepsilon_{n_2,n_1} - \omega & 0 \\ 0 & \Delta\varepsilon_{n_2,n_1} - \omega \end{bmatrix}, \tag{3.18}$$

which allows us to extract the frequency-dependence:

$$-i\underline{\tilde{\mathbf{L}}}_0^{-1}(\omega) = \underline{\mathbf{D}} - \omega\underline{\mathbf{I}} = \underbrace{\begin{bmatrix} \Delta\varepsilon_{n_2,n_1} & 0 \\ 0 & \Delta\varepsilon_{n_2,n_1} \end{bmatrix}}_{=:\underline{\mathbf{D}} \in \mathbb{C}^{2N_t \times 2N_t}} - \omega \underbrace{\begin{bmatrix} 1 & 0 \\ 0 & 1 \end{bmatrix}}_{=:\underline{\mathbf{I}} \in \mathbb{R}^{2N_t \times 2N_t}}. \tag{3.19}$$

Furthermore, we introduce the two-particle Hamiltonian $\underline{\mathbf{H}}^{\mathrm{2p}}$:

$$\underline{\mathbf{H}}^{\mathrm{2p}}(\omega) := \underline{\mathbf{D}} + i\underline{\mathbf{FK}}. \tag{3.20}$$

Using Equations 3.19 and 3.20, we rewrite Equation 3.17 into

$$-i\underline{\mathbf{L}} = \left[\underline{\mathbf{H}}^{\mathrm{2p}} - \omega\underline{\mathbf{I}}\right]^{-1}\underline{\mathbf{F}}. \tag{3.21}$$

Using this expression, we can calculate the two-particle correlation function $\underline{\mathbf{L}}$ and in turn the reducible polarizability χ (Equation 2.63), which we need for the *GW* calculations. However, this expression is problematic since it requires the evaluation of a frequency-dependent matrix inverse at every *GW* iteration. We can simplify this frequency-dependence by rewriting the matrix inverse in terms of the eigendecomposition of the two-particle Hamiltonian $\underline{\mathbf{H}}^{\mathrm{2p}}$. In the next section, we solve the eigenvalue problem related to the two-particle Hamiltonian $\underline{\mathbf{H}}^{\mathrm{2p}}$ to find an alternative expression of the polarizability χ.

3.2 Diagonalizing the Two-Particle Hamiltonian

By diagonalizing the two-particle Hamiltonian $\underline{\mathbf{H}}^{\mathrm{2p}}$ (Equation 3.20), we compute the eigenvalues Ω_s and eigenvectors $\mathbf{u}_s$. The eigenvalues and eigenvectors are required compute the reducible polarizability χ (Equation 3.42), which we need for the *GW* calculations. Due to the symmetry between the resonant ($c \to c$) and anti-resonant ($v \to c$) transitions, the two-particle Hamiltonian has a very specific block structure [27]:

$$\underline{\mathbf{H}}^{\mathrm{2p}} = \begin{bmatrix} \underline{\mathbf{A}} & \underline{\mathbf{B}} \\ -\underline{\mathbf{B}} & -\underline{\mathbf{A}} \end{bmatrix} \in \mathbb{R}^{2N_t \times 2N_t}, \tag{3.22}$$

with $\underline{\mathbf{A}}, \underline{\mathbf{B}} \in \mathbb{R}^{N_t \times N_t}$ and $N_t = N_v \cdot N_v$. The individual matrix blocks read

$$[\underline{\mathbf{A}}]_{v,c}^{v',c'} = (\varepsilon_c - \varepsilon_v)\delta_{v,v'}\delta_{c,c'} + (vc|v'c') + \Xi_{v,c}^{v',c'}, \tag{3.23a}$$

$$[\underline{\mathbf{B}}]_{v,c}^{v',c'} = (vc|v'c') + \Xi_{v,c}^{v',c'}. \tag{3.23b}$$

Index $v = 1, 2, \ldots, N_v$ runs over the occupied MOs (/valence states) and index $c = 1, 2, \ldots, N_c$ runs over the unoccupied MOs (/conduction states). The BSE kernel Ξ is responsible for modeling the electron-hole interactions that arise in two-particle excitations. A variety of methods exists to deal with the electron-hole interactions, including: RPA, TD-HF, TD-DFT and BSE. The only difference between these methods lies in the expression of the BSE kernel Ξ. We calculate the polarizability χ in the RPA setting, for which $\Xi = 0$. The Molecular Electronic Repulsion (ERI) integral $(ab|cd)$ is defined as:

$$(ab|cd) := \iint \mathrm{d}\mathbf{r}_1 \mathrm{d}\mathbf{r}_2 \; \phi_a(\mathbf{r}_1)\, \phi_b(\mathbf{r}_1)\, |\mathbf{r}_1 - \mathbf{r}_2|^{-1} \phi_c(\mathbf{r}_2)\, \phi_d(\mathbf{r}_2). \tag{3.24}$$

Using the resolution-of-identity (RI) approximation, we can efficiently evaluate an entire range of ERI integrals using matrix multiplication:

$$\underline{\mathbf{E}}_{a,c} = \underline{\mathbf{M}}[a]\underline{\mathbf{M}}[c]^T \in \mathbb{R}^{N_{\mathrm{MO}} \times N_{\mathrm{MO}}}, \qquad [\underline{\mathbf{E}}_{a,c}]_{b,d} = \sum\nolimits_{\beta} M_{a,b}^{\beta} M_{c,d}^{\beta} \approx (ab|cd). \tag{3.25}$$

Here, $\underline{\mathbf{M}} \in \mathbb{R}^{N_{\mathrm{MO}} \times N_{\mathrm{MO}} \times N_x}$ are the pre-computed three-center integrals over the auxiliary basis set, with dimensions N_x. See Appendix B.2 for more information.

We write the $2N_t \times 2N_t$ diagonalization of the two-particle Hamiltonian $\underline{\mathbf{H}}^{\mathrm{2p}}$ as follows:

$$\begin{bmatrix} \underline{\mathbf{A}} & \underline{\mathbf{B}} \\ -\underline{\mathbf{B}} & -\underline{\mathbf{A}} \end{bmatrix} \begin{bmatrix} \mathbf{X}_s \\ \mathbf{Y}_s \end{bmatrix} = \Omega_s \begin{bmatrix} \mathbf{X}_s \\ \mathbf{Y}_s \end{bmatrix}. \tag{3.26}$$

The eigenvalues Ω_s denote the neutral excitation energies [1]. We solve this eigenvalue problem for the purpose of evaluating the reducible polarizability (Equation 3.42). Due to the specific block structure of $\underline{\mathbf{H}}^{\mathrm{2p}}$, we can rewrite the eigenvalue problem in Equation 3.26 into a smaller eigenvalue problem. From Equation 3.26 follows the set of coupled equations:

$$\underline{\mathbf{A}}\mathbf{X}_s + \underline{\mathbf{B}}\mathbf{Y}_s = \Omega_s \mathbf{X}_s, \tag{3.27a}$$

$$-\underline{\mathbf{B}}\mathbf{X}_s - \underline{\mathbf{A}}\mathbf{Y}_s = \Omega_s \mathbf{Y}_s. \tag{3.27b}$$

Addition and subtraction of Equations 3.27a and 3.27b yields

$$(\underline{\mathbf{A}} - \underline{\mathbf{B}})(\mathbf{X}_s - \mathbf{Y}_s) = \Omega_s(\mathbf{X}_s + \mathbf{Y}_s). \tag{3.28a}$$

$$(\underline{\mathbf{A}} + \underline{\mathbf{B}})(\mathbf{X}_s + \mathbf{Y}_s) = \Omega_s(\mathbf{X}_s - \mathbf{Y}_s), \tag{3.28b}$$

By combining Equations 3.28a and 3.28b, we obtain

$$\begin{aligned} & (\underline{\mathbf{A}} + \underline{\mathbf{B}})(\mathbf{X}_s + \mathbf{Y}_s) = \Omega_s^2 (\underline{\mathbf{A}} - \underline{\mathbf{B}})^{-1}(\mathbf{X}_s + \mathbf{Y}_s) \\ \Leftrightarrow \quad & (\underline{\mathbf{A}} - \underline{\mathbf{B}})^{1/2}(\underline{\mathbf{A}} + \underline{\mathbf{B}})(\mathbf{X}_s + \mathbf{Y}_s) = \Omega_s^2 (\underline{\mathbf{A}} - \underline{\mathbf{B}})^{-1/2}(\mathbf{X}_s + \mathbf{Y}_s) \\ \Leftrightarrow \quad & (\underline{\mathbf{A}} - \underline{\mathbf{B}})^{1/2}(\underline{\mathbf{A}} + \underline{\mathbf{B}})(\underline{\mathbf{A}} - \underline{\mathbf{B}})^{1/2}(\underline{\mathbf{A}} - \underline{\mathbf{B}})^{-1/2}(\mathbf{X}_s + \mathbf{Y}_s) = \Omega_s^2 (\underline{\mathbf{A}} - \underline{\mathbf{B}})^{-1/2}(\mathbf{X}_s + \mathbf{Y}_s). \end{aligned} \tag{3.29}$$

[1] If the BSE kernel Ξ is configured to the BSE method, the eigenvalues Ω_s equate to the neutral excitation energies of the fully-interacting system

Finally, we define

$$\underline{\mathbf{C}} := (\underline{\mathbf{A}} - \underline{\mathbf{B}})^{1/2}(\underline{\mathbf{A}} + \underline{\mathbf{B}})(\underline{\mathbf{A}} - \underline{\mathbf{B}})^{1/2}, \quad (3.30) \qquad \mathbf{Z}_s := (\underline{\mathbf{A}} - \underline{\mathbf{B}})^{-1/2}(\mathbf{X}_s + \mathbf{Y}_s). \quad (3.31)$$

Equation 3.29 can then be rewritten into the smaller $N_s \times N_s$ eigenvalue problem:

$$\underline{\mathbf{C}}\mathbf{Z}_s = \Omega_s^2 \mathbf{Z}_s, \tag{3.32}$$

where $N_s := N_t$ denotes the number of eigenvalues of the two-particle Hamiltonian. The matrix $\underline{\mathbf{C}}$ is again Hermitian and half the size of the original problem. From the eigenvectors $\mathbf{Z}_s$, we can recover the vectors $\mathbf{X}_s$ and $\mathbf{Y}_s$ according to: [2]

$$(\mathbf{X}_s + \mathbf{Y}_s) = (\underline{\mathbf{A}} - \underline{\mathbf{B}})^{1/2}\mathbf{Z}_s, \tag{3.33a}$$
$$(\mathbf{X}_s - \mathbf{Y}_s) = \Omega_s(\underline{\mathbf{A}} - \underline{\mathbf{B}})^{-1/2}\mathbf{Z}_s, \tag{3.33b}$$

followed by addition and subtraction of Equations 3.33a and 3.33b:

$$\mathbf{X}_s = \frac{1}{2}\left[(\underline{\mathbf{A}} - \underline{\mathbf{B}})^{1/2} + \Omega_s(\underline{\mathbf{A}} - \underline{\mathbf{B}})^{-1/2}\right]\mathbf{Z}_s, \tag{3.34a}$$
$$\mathbf{Y}_s = \frac{1}{2}\left[(\underline{\mathbf{A}} - \underline{\mathbf{B}})^{1/2} - \Omega_s(\underline{\mathbf{A}} - \underline{\mathbf{B}})^{-1/2}\right]\mathbf{Z}_s. \tag{3.34b}$$

Note that the matrix $(\underline{\mathbf{A}} - \underline{\mathbf{B}}) = (\varepsilon_c - \varepsilon_v)\delta_{v,v'}\delta_{c,c'}$ is diagonal in the RPA setting ($\Xi = 0$). Therefore, its inverse and square root in Equations 3.34a and 3.34b are readily available.

Returning to the original eigenvalue problem. From

$$\underline{\mathbf{H}}^{2\mathrm{p}}[\mathbf{Y}_s^T \;\; \mathbf{X}_s^T]^T = -\Omega_s[\mathbf{Y}_s^T \;\; \mathbf{X}_s^T]^T \quad \text{and} \quad [\mathbf{X}_s^T \;\; -\mathbf{Y}_s^T]\underline{\mathbf{H}}^{2\mathrm{p}} = \Omega_s[\mathbf{X}_s^T \;\; -\mathbf{Y}_s^T]$$

follow the same set of coupled equations as Equations 3.27a and 3.27b and are thus valid solutions to the eigenvalue problem. In conclusion, we find

$$\underline{\mathbf{H}}^{2\mathrm{p}}\underline{\mathbf{U}} = \underline{\mathbf{U}}\underline{\mathbf{\Lambda}} \quad \Leftrightarrow \quad \underbrace{\begin{bmatrix} \underline{\mathbf{A}} & \underline{\mathbf{B}} \\ -\underline{\mathbf{B}} & -\underline{\mathbf{A}} \end{bmatrix}}_{=\underline{\mathbf{H}}^{2\mathrm{p}}} \underbrace{\begin{bmatrix} \underline{\mathbf{X}} & \underline{\mathbf{Y}} \\ \underline{\mathbf{Y}} & \underline{\mathbf{X}} \end{bmatrix}}_{=\underline{\mathbf{U}}} = \underbrace{\begin{bmatrix} \underline{\mathbf{X}} & \underline{\mathbf{Y}} \\ \underline{\mathbf{Y}} & \underline{\mathbf{X}} \end{bmatrix}}_{=\underline{\mathbf{U}}} \underline{\mathbf{\Lambda}}, \tag{3.35a}$$

$$\underline{\mathbf{V}}\underline{\mathbf{H}}^{2\mathrm{p}} = \underline{\mathbf{\Lambda}}\underline{\mathbf{V}} \quad \Leftrightarrow \quad \underbrace{\begin{bmatrix} \underline{\mathbf{X}} & -\underline{\mathbf{Y}} \\ -\underline{\mathbf{Y}} & \underline{\mathbf{X}} \end{bmatrix}^T}_{=\underline{\mathbf{V}}} \underbrace{\begin{bmatrix} \underline{\mathbf{A}} & \underline{\mathbf{B}} \\ -\underline{\mathbf{B}} & -\underline{\mathbf{A}} \end{bmatrix}}_{=\underline{\mathbf{H}}^{2\mathrm{p}}} = \underline{\mathbf{\Lambda}} \underbrace{\begin{bmatrix} \underline{\mathbf{X}} & -\underline{\mathbf{Y}} \\ -\underline{\mathbf{Y}} & \underline{\mathbf{X}} \end{bmatrix}^T}_{=\underline{\mathbf{V}}}, \tag{3.35b}$$

where

$$\underline{\mathbf{X}} = [\mathbf{X}_1, \mathbf{X}_2, \ldots, \mathbf{X}_{N_s}] \cdot \underline{\mathbf{c}} \in \mathbb{R}^{N_s \times N_s}, \quad (3.36) \qquad \underline{\mathbf{Y}} = [\mathbf{Y}_1, \mathbf{Y}_2, \ldots, \mathbf{Y}_{N_s}] \cdot \underline{\mathbf{c}} \in \mathbb{R}^{N_s \times N_s}. \quad (3.37)$$

Furthermore,

$$\underline{\mathbf{\Lambda}} = \mathrm{diag}(\Omega_1, \Omega_2, \ldots, \Omega_{N_s}, -\Omega_1, -\Omega_2, \ldots, -\Omega_{N_s}) \in \mathbb{R}^{2N_s \times 2N_s} \tag{3.38}$$

[2] The latter follows from Equation 3.28a: $(\mathbf{X}_s - \mathbf{Y}_s) = \Omega_s(\underline{\mathbf{A}} - \underline{\mathbf{B}})^{-1}(\mathbf{X}_s + \mathbf{Y}_s) = \Omega_s(\underline{\mathbf{A}} - \underline{\mathbf{B}})^{-1/2}\mathbf{Z}_s$.

contains the eigenvalues λ_k on its diagonal, $\underline{\mathbf{U}} \in \mathbb{R}^{2N_s \times 2N_s}$ contains the right eigenvectors $\mathbf{u}_k$ in its columns and $\underline{\mathbf{V}} \in \mathbb{R}^{2N_s \times 2N_s}$ contains the left eigenvectors $\mathbf{v}_k$ on its rows. Note that, in Equations 3.36 and 3.37, we scale the eigenvectors $\mathbf{X}_s$ and $\mathbf{Y}_s$ with the normalization factors c_s, contained in the matrix $\underline{\mathbf{c}} = \mathrm{diag}(c_1, c_2, \ldots, c_{N_s}) \in \mathbb{R}^{N_s \times N_s}$. After some algebra:

$$\mathbf{X}_s^T \mathbf{X}_s = \frac{1}{4} \mathbf{Z}_s^T \left[(\underline{\mathbf{A}} - \underline{\mathbf{B}}) + 2\Omega_s + \Omega_s^2 (\underline{\mathbf{A}} - \underline{\mathbf{B}})^{-1} \right] \mathbf{Z}_s, \tag{3.39a}$$

$$\mathbf{Y}_s^T \mathbf{Y}_s = \frac{1}{4} \mathbf{Z}_s^T \left[(\underline{\mathbf{A}} - \underline{\mathbf{B}}) - 2\Omega_s + \Omega_s^2 (\underline{\mathbf{A}} - \underline{\mathbf{B}})^{-1} \right] \mathbf{Z}_s, \tag{3.39b}$$

$$\mathbf{X}_s^T \mathbf{Y}_s = \mathbf{Y}_s^T \mathbf{X}_s = \frac{1}{4} \mathbf{Z}_s^T \left[(\underline{\mathbf{A}} - \underline{\mathbf{B}}) - \Omega_s^2 (\underline{\mathbf{A}} - \underline{\mathbf{B}})^{-1} \right] \mathbf{Z}_s, \tag{3.39c}$$

$$\mathbf{X}_s^T \mathbf{X}_s - \mathbf{Y}_s^T \mathbf{Y}_s = \Omega_s \mathbf{Z}_s^T \mathbf{Z}_s = \Omega_s, \tag{3.39d}$$

$$\mathbf{X}_s^T \mathbf{Y}_s - \mathbf{Y}_s^T \mathbf{X}_s = 0, \tag{3.39e}$$

where we assume that the eigenvectors $\mathbf{Z}_s$ are normalized, we find:

$$\begin{aligned} \underline{\mathbf{VU}} &= \begin{bmatrix} \mathbf{X} & -\mathbf{Y} \\ -\mathbf{Y} & \mathbf{X} \end{bmatrix}^T \begin{bmatrix} \mathbf{X} & \mathbf{Y} \\ \mathbf{Y} & \mathbf{X} \end{bmatrix} = \begin{bmatrix} \mathbf{X}^T & -\mathbf{Y}^T \\ -\mathbf{Y}^T & \mathbf{X}^T \end{bmatrix} \begin{bmatrix} \mathbf{X} & \mathbf{Y} \\ \mathbf{Y} & \mathbf{X} \end{bmatrix} \\ &= \begin{bmatrix} \mathbf{X}^T\mathbf{X} - \mathbf{Y}^T\mathbf{Y} & \mathbf{X}^T\mathbf{Y} - \mathbf{Y}^T\mathbf{X} \\ \mathbf{X}^T\mathbf{Y} - \mathbf{Y}^T\mathbf{X} & \mathbf{X}^T\mathbf{X} - \mathbf{Y}^T\mathbf{Y} \end{bmatrix} = \begin{bmatrix} \underline{\mathbf{c}}^2 & \underline{\mathbf{0}} \\ \underline{\mathbf{0}} & \underline{\mathbf{c}}^2 \end{bmatrix} \underline{\mathbf{\Lambda}}. \end{aligned} \tag{3.40}$$

The normalization condition $\underline{\mathbf{VU}} = \underline{\mathbf{I}}$ is satisfied when $c_s = \Omega_s^{-1/2}$. The two-particle Hamiltonian $\underline{\mathbf{H}}^{2\mathrm{p}}$ can then be decomposed in its eigenvalues and eigenvectors as follows [3]:

$$\underline{\mathbf{H}}^{2\mathrm{p}} = \underline{\mathbf{U\Lambda U}}^{-1} = \underline{\mathbf{U\Lambda V}} = \sum\nolimits_k \lambda_k \mathbf{u}_k \mathbf{v}_k^T. \tag{3.41}$$

Using this eigendecomposition, we write an alternative expression of the polarizability χ:

$$\underline{\chi} = -i\underline{\mathbf{L}} = \left[\underline{\mathbf{H}}^{2\mathrm{p}} - \omega \underline{\mathbf{I}} \right]^{-1} \underline{\mathbf{F}} = \sum\nolimits_k \frac{\mathbf{u}_k \mathbf{v}_k^T}{\lambda_k - \omega} \underline{\mathbf{F}}. \tag{3.42}$$

where $(\lambda_k - \omega)^{-1}$ are the eigenvalues of the matrix $[\underline{\mathbf{H}}^{2\mathrm{p}} - \omega \underline{\mathbf{I}}]^{-1}$.

In summary, we first compute matrices $\underline{\mathbf{A}}$ and $\underline{\mathbf{B}}$, using Equations 3.23a, 3.23b and then the matrix $\underline{\mathbf{C}}$ using Equation 3.32. We solve the eigenvalue problem in Equation 3.32, to find the eigenvalues Ω^2 and eigenvectors $\mathbf{Z}_s$ of $\underline{\mathbf{C}}$. We then reconstruct the eigenvectors of the original eigenvalue problem according to Equations 3.35a and 3.35b. Finally, we calculate the polarizability using Equation 3.42.

The matrix $\underline{\mathbf{C}}$, being represented in the transition space, is Hermitian. Furthermore, because the eigenvalues of $\underline{\mathbf{C}}$ represent physical energies > 0, we must have that $\underline{\mathbf{C}}$ is positive definite. When we solve the eigenvalue problem related to $\underline{\mathbf{C}}$, we can choose an eigenvalue algorithm that exploits these matrix properties.

[3] The latter equation follows from: $[\underline{\mathbf{H}}^{2\mathrm{p}}]_{i,j} = [\underline{\mathbf{U\Lambda V}}]_{i,j} = \sum_k \lambda_k [\underline{\mathbf{U}}]_{i,k} [\underline{\mathbf{V}}]_{k,j} = \sum_k \lambda_k [\mathbf{u}_k]_i [\mathbf{v}_k^T]_j = [\sum_k \lambda_k \mathbf{u}_k \mathbf{v}_k^T]_{i,j}$.

3.3 Computing the Self-Energy

Now that we calculated the polarizability χ (Equation 3.42) by diagonalizing the two-particle Hamiltonian, we can proceed with solving Hedin's equations for the self-energy. The self-energy is given by the convolution of the Green's function G and the screened Coulomb interaction W. Symbolically: $\Sigma = GW$ (Equation 2.49a). According to the convolution theorem, a product in the time domain results in a convolution in the Fourier domain:

$$\Sigma(\mathbf{r}, \mathbf{r}', \omega) = \frac{i}{2\pi} \int \mathrm{d}\omega_1 e^{i\eta\omega_1} G(\mathbf{r}, \mathbf{r}', \omega + \omega_1) W(\mathbf{r}, \mathbf{r}', \omega_1). \tag{3.43}$$

The Green's function is given by Equation 2.44. The screened Coulomb interaction is given by Equation 2.49d:

$$W(1,2) = \int \mathrm{d}3 \epsilon^{-1}(1,3) v(3,2), \tag{3.44}$$

or symbolically: $W = \epsilon^{-1} v$. This form is inconvenient as it contains the inversion of the dielectric function ϵ. Fortunately, this inversion is known as it is required to compute the optical excitation spectra [28]. It relates to the reducible polarizability χ as follows:

$$\epsilon^{-1}(1,2) = \delta(1,2) + \int \mathrm{d}3 v(1,3) \chi(3,2), \tag{3.45}$$

or symbolically: $\epsilon^{-1} = \delta + v\chi$. In Section 3.1.2, we calculate the reducible polarizability χ (Equation 2.63) exactly by solving the eigenvalue problem related to the two-particle Hamiltonian $\underline{\mathbf{H}}^{\mathrm{2p}}$ (Equation 3.20). Substituting Equation 3.45 into Equation 3.44 yields:

$$\begin{aligned} W(1,2) &= \int \mathrm{d}3 \epsilon^{-1}(1,3) v(3,2) \\ &= \int \mathrm{d}3 \left(\delta(1,3) + \int d4 v(1,4) \chi(4,3) \right) v(3,2) \\ &= \int \mathrm{d}3 \delta(1,3) v(3,2) + \int \mathrm{d}34 v(1,4) \chi(4,3) v(3,2) \\ &= v(1,2) + \int \mathrm{d}34 v(1,3) \chi(3,4) v(4,2), \end{aligned} \tag{3.46}$$

or symbolically: $W = v + v\chi v$. We substitute this into the expression of the self-energy (Equation 3.43). Consequently, the self-energy is split into two terms: the self-energy exchange Σ_x and the self-energy correlation Σ_c. Symbolically:

$$\Sigma(\omega) = \Sigma_x + \Sigma_c(\omega), \quad \text{with} \quad \Sigma_x = \int \mathrm{d}\omega' G v, \quad \Sigma_c(\omega) = \int \mathrm{d}\omega' v \chi(\omega) v. \tag{3.47}$$

Practical calculations are performed in real coordinate space using the self-energy exchange matrix:

$$[\underline{\mathbf{\Sigma}}_x]_{mn} = \langle m | \Sigma_x | n \rangle, \tag{3.48}$$

and the self-energy correlation matrix:

$$[\underline{\mathbf{\Sigma}}_c(\omega)]_{mm} := \mathrm{Re}\left[\langle m | \Sigma_c([\omega]_m) | m \rangle \right], \tag{3.49a}$$

$$[\underline{\mathbf{\Sigma}}_c(\omega)]_{mn} := \frac{1}{2} \Big(\mathrm{Re}\big[\langle m | \Sigma_c([\omega]_m) | n \rangle \big] + \mathrm{Re}\big[\langle m | \Sigma_c([\omega]_n) | n \rangle \big] \Big). \tag{3.49b}$$

The off-diagonal elements of $\underline{\mathbf{\Sigma}}_c$ are approximated by [29]. Note that the diagonal elements, which are important during the GW self-consistency, are not affected by this approximation.

In Section 3.3.1, we present an expression for the exchange term Σ_x with which we can easily compute it. Unfortunately, calculating the correlation term Σ_c is not as straightforward. As we have discussed, the calculation of χ requires the diagonalization of the two-particle Hamiltonian $\underline{\mathbf{H}}^{2\mathrm{p}}$. This diagonalization step is particularly expensive. We could, however, approximate the polarizability using a *plasmon-pole* model. Importantly, this is where the method branches off into: (1) the Fully-Analytical Approach (FAA) and (2) the Plasmon-Pole Model (PPM). In the FAA, we calculate χ exactly by solving the eigenvalue problem related to $\underline{\mathbf{H}}^{2\mathrm{p}}$. This method is discussed in Section 3.3.2. In the PPM, we approximate χ using a plasmon-pole model. This method is discussed in Section 3.3.3.

3.3.1 Self-Energy Exchange

The expectation values of the self-energy exchange are given by [24]:

$$\langle m|\,\Sigma_x\,|n\rangle = -\sum_v \int \mathrm{d}\mathbf{r}_1 \mathrm{d}\mathbf{r}_2 \frac{\phi_m(\mathbf{r}_1)\phi_v(\mathbf{r}_2)\phi_n^*(\mathbf{r}_2)\phi_v^*(\mathbf{r}_1)}{|\mathbf{r}_1-\mathbf{r}_2|}. \tag{3.50}$$

3.3.2 Self-Energy Correlation (FAA)

We can calculate the reducible polarizability χ exactly. As discussed, this calculation involves solving the $N_s \times N_s$ eigenvalue problem related to the two-particle Hamiltonian $\underline{\mathbf{H}}^{2\mathrm{p}}$. Once the polarizability is calculated, the self-energy correlation can be analytically integrated using complex contour deformation theory [24]. We give a brief overview of contour deformation theory in Appendix A.1. The expectation values of the self-energy correlation are given by [27]:

$$\langle m|\,\Sigma_c(\omega)\,|n\rangle = 2\left(\sum_{v,s}\frac{R^s_{m,v}R^s_{n,v}}{\omega-\varepsilon_v+\Omega_s-i\eta}+\sum_{c,s}\frac{R^s_{m,c}R^s_{n,c}}{\omega-\varepsilon_c-\Omega_s+i\eta}\right). \tag{3.51}$$

The factor 2 accounts for the fact that, in a closed shell systems, each MO is occupied by two electrons. The residues $R^s_{m,n}$ are defined as:

$$R^s_{m,n} := \sum_{v,c}(mn|vc)(X^s_{v,c}+Y^s_{v,c}). \tag{3.52}$$

The real part of the self-energy correlation is found to be:

$$\begin{aligned}\mathrm{Re}\big[\,\langle m|\,\Sigma_c(\omega)\,|n\rangle\,\big] = 2\Bigg(&\sum_{v,s}\frac{R^s_{m,v}R^s_{n,v}\,(\omega-\varepsilon_v+\Omega_s)}{(\omega-\varepsilon_v+\Omega_s)^2+\eta^2}\\ &+\sum_{c,s}\frac{R^s_{m,c}R^s_{n,c}\,(\omega-\varepsilon_c-\Omega_s)}{(\omega-\varepsilon_c-\Omega_s)^2+\eta^2}\Bigg).\end{aligned} \tag{3.53}$$

3.3.3 Self-Energy Correlation (PPM)

Instead of calculating the dielectric function ϵ exactly, we can instead approximate it using a Plasmon-Pole Model (PPM) [30]. Before we approximate ϵ, we express it in its symmetrized form. To this end, we introduce the *symmetrized Coulomb interaction* $\tilde{v}(\mathbf{r}_1, \mathbf{r}_2) = \pi^{-3/2}|\mathbf{r}_1 - \mathbf{r}_2|^{-2}$, which convoluted with itself gives back the bare Coulomb interaction:

$$v(\mathbf{r}_1, \mathbf{r}_2) = \int \mathrm{d}3\tilde{v}(\mathbf{r}_1, \mathbf{r}_3)\tilde{v}(\mathbf{r}_3, \mathbf{r}_2), \tag{3.54}$$

or symbolically: $v = \tilde{v}\tilde{v}$. The symmetrized Coulomb interaction $\tilde{v}$ relates the conventional dielectric function ϵ to the *symmetrized dielectric function* $\tilde{\epsilon}$ via:

$$\tilde{\epsilon} := \tilde{v}^{-1}\epsilon\tilde{v}. \tag{3.55}$$

Substituting this into Equations 3.44 and 3.45 yields the symmetrized forms of the screened Coulomb interaction W and the dielectric function ϵ respectively [4]:

$$W = \tilde{v}\tilde{\epsilon}^{-1}\tilde{v}, \tag{3.56}$$

$$\tilde{\epsilon}^{-1} = \delta + \tilde{v}\chi\tilde{v}. \tag{3.57}$$

The symmetrized dielectric function can be decomposed in its eigenvalues λ_ℓ and eigenvectors Φ_ℓ as follows:

$$[\underline{\tilde{\epsilon}}]_{\alpha,\beta}(\omega) = \sum_{\ell}^{N_x} \Phi_\ell^\alpha(\omega)\lambda_\ell(\omega)(\Phi_\ell^\beta)^*(\omega). \tag{3.58}$$

We can now approximate $\tilde{\epsilon}$ by replacing the reducible polarizability χ by the static polarizability $P(\omega = 0)$ (Equation 3.5). Replacing χ with $P(\omega = 0)$, in Equation 3.57, yields the static dielectric function. The static dielectric function is then extended to the dynamic dielectric function using a Plasmon-Pole Model (PPM) [30]. According to the PPM approximation, only the eigenvalues λ_ℓ are assumed to depend on the frequency ω, whereas the eigenvectors Φ_ℓ are assumed to be frequency independent:

$$\lambda_\ell^{-1}(\omega) \approx 1 + \frac{z_\ell\omega_\ell}{2}\left[\frac{1}{\omega - (\omega_\ell - i\eta)} - \frac{1}{\omega + (\omega_\ell - i\eta)}\right]. \tag{3.59}$$

Here, z_ℓ denotes the plasmon-pole weight and ω_ℓ denotes the plasmon-pole frequency. The two model parameters z_ℓ and ω_ℓ are found by fitting the plasmon-pole model (Equation 3.58) to the exact dielectric function for the frequencies $\omega = 0$ and $\omega = E_0 i$, with E_0 an additional model parameter. The self-energy Σ now follows from Equation 3.43, using $W = \tilde{v}\tilde{\epsilon}^{-1}\tilde{v}$. Note that the frequency-independent part of $\lambda_\ell(\omega)$, which equals 1, results in the self-energy exchange, whose expectation values are given by Equation 3.50. The remainder yields the self-energy correlation, whose expectation values are given by:

$$\langle m|\,\Sigma_c(\omega)\,|n\rangle = 2\left(\sum_{v,\ell}\frac{\frac{1}{4}z_\ell\omega_\ell M^\ell_{m,v}M^\ell_{n,v}}{\omega - \varepsilon_v + \omega_\ell} + \sum_{c,\ell}\frac{\frac{1}{4}z_\ell\omega_\ell M^\ell_{m,c}M^\ell_{n,c}}{\omega - \varepsilon_c - \omega_\ell}\right). \tag{3.60}$$

The factor 2 accounts for the fact that, in a closed shell systems, each MO is occupied by two electrons.

[4] Using $W = \epsilon^{-1}v = \tilde{v}\tilde{v}^{-1}\epsilon^{-1}\tilde{v}\tilde{v} = \tilde{v}\tilde{\epsilon}^{-1}\tilde{v}$ and $\tilde{\epsilon}^{-1} = \tilde{v}^{-1}\epsilon^{-1}\tilde{v} = \tilde{v}^{-1}(\delta + \tilde{v}\tilde{v}\chi)\tilde{v} = \delta + \tilde{v}\chi\tilde{v}$.

3.4 Computing the Quasi-Particle Energies

Now that we computed the self-energy by solving Hedin's equation, we can proceed with calculating the quasi-particle energies. The quasi-particle energies $\varepsilon_i^{\mathrm{QP}}$ are obtained by solving the Quasi-Particle (QP) equation (Equation 2.57) on the real axis:

$$\varepsilon_i^{\mathrm{QP}} = \varepsilon_i^{\mathrm{KS}} + \langle \phi_i^{\mathrm{KS}} | \, \Sigma_c(\varepsilon_i^{\mathrm{QP}}) + \Sigma_x - \hat{V}_{\mathrm{XC}} \, | \phi_i^{\mathrm{KS}} \rangle \, , \qquad i = 1, 2, \ldots, N_{\mathrm{MO}}. \tag{3.61}$$

Here, $\varepsilon_i^{\mathrm{QP}}$ and $\varepsilon_i^{\mathrm{KS}}$ denote the quasi-particle and Kohn-Sham energy corresponding to the i^{th} MO respectively. The Kohn-Sham energies are obtained through a preceding DFT calculation. The diagonal expectation values of the self-energy exchange Σ_x and correlation Σ_c are given by Equations 3.50 and 3.51 respectively. The expectation values of the exchange-correlation potential $\hat{V}_{\mathrm{XC}}$ depend on the specific functional that is used.

We solve the QP equation for each state separately and we can therefore drop the i subscript. We rewrite Equation 3.61 using simplified notation:

$$\omega = \varepsilon_{\mathrm{KS}} + \sigma_c(\omega) + \sigma_x - \nu_{\mathrm{XC}}, \tag{3.62}$$

where

$$\sigma_c(\cdot) := \mathrm{Re}[\langle \phi_i^{\mathrm{KS}} | \, \Sigma_c(\cdot) \, | \phi_i^{\mathrm{KS}} \rangle], \quad \sigma_x := \mathrm{Re}[\langle \phi_i^{\mathrm{KS}} | \, \Sigma_x \, | \phi_i^{\mathrm{KS}} \rangle], \quad \nu_{\mathrm{XC}} := \mathrm{Re}[\langle \phi_i^{\mathrm{KS}} | \, \hat{V}_{\mathrm{XC}} \, | \phi_i^{\mathrm{KS}} \rangle].$$

The variable ω denotes the QP energy $\varepsilon_{\mathrm{QP}}$. The KS energy $\varepsilon_{\mathrm{KS}}$, the self-energy exchange σ_x and the exchange-correlation potential ν_{XC} are essentially constants since they do not depend on ω. Note that $\sigma_c(\omega)$ has a nonlinear dependence on the QP energy $\varepsilon_{\mathrm{QP}}$, which means that we must solve Equation 3.62 numerically.

Before we proceed with solving the QP equation, we first investigate the self-energy correlation function. The real part of the self-energy correlation is given by Equation 3.53. Its diagonal elements van be written as:

$$\sigma_c(\omega) = \sum_{n,s} \frac{R^s_{m,n} R^s_{m,n} \left(\omega - \varepsilon_n + \Theta_{N_v}(n)\Omega_s\right)}{\left(\omega - \varepsilon_n + \Theta_{N_v}(n)\Omega_s\right)^2 + \eta^2}, \qquad \Theta_{N_v}(n) = \begin{cases} +1 & \text{if} n > N_v, \\ -1 & \text{otherwise.} \end{cases} \tag{3.63}$$

We note that $\sigma_c(\omega)$ has no poles on the real axis since the discriminant of its denominator equals $-4\eta^2 < 0$. The function $\sigma_c(\omega)$ is therefore defined and continuous over the entire real axis. This is exactly why we introduced the "small" parameter η. We can derive an expression for the derivative $\sigma_c'(\omega)$. Let $R \equiv R^s_{m,n} R^s_{m,n}$ and

$$E(\omega) := \omega - \varepsilon_n + \Theta_{N_v}(n)\Omega_s, \quad \text{s.t.} \quad E'(\omega) = 1 \quad \text{and} \quad [E(\omega)^2]' = 2E(\omega)E'(\omega) = 2E(\omega).$$

We then rewrite Equation 3.63 into:

$$\sigma_c(\omega) = \sum_{n,s} \frac{RE(\omega)}{E(\omega)^2 + \eta^2}. \tag{3.64}$$

We compute

$$\frac{\mathrm{d}RE(\omega)}{\mathrm{d}\omega} = RE'(\omega) = R, \qquad \frac{\mathrm{d}[E(\omega)^2 + \eta^2]}{\mathrm{d}\omega} = 2E(\omega).$$

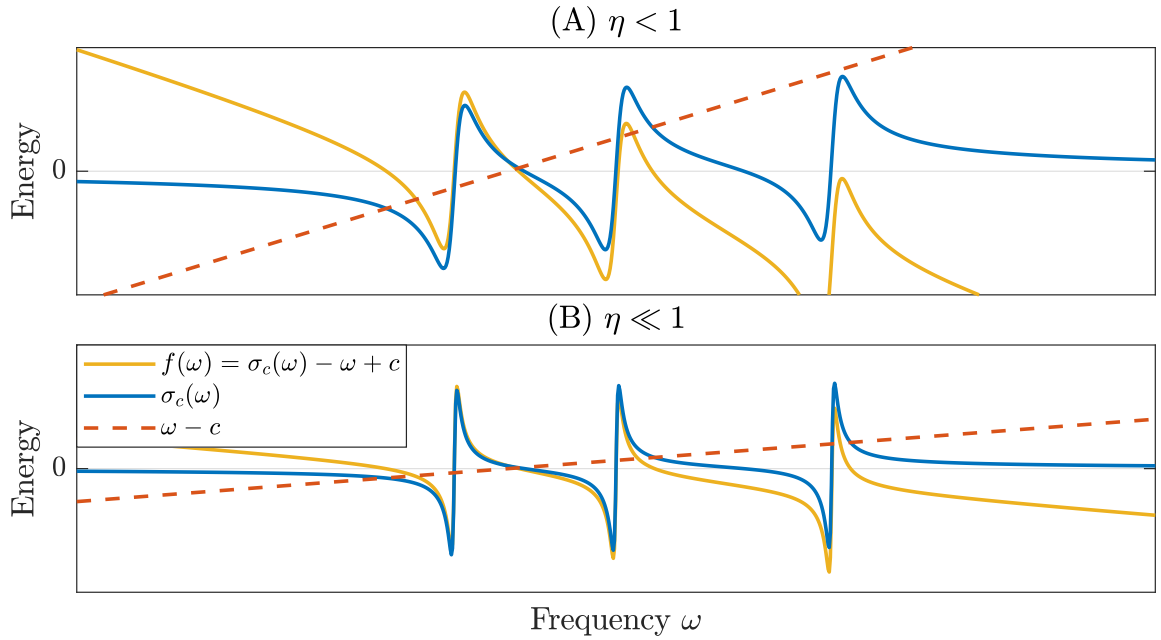

Figure 3.1: A sketch of the real part of the self-energy correlation $\sigma_c(\omega)$. The QP energies are defined as the points-of-intersections of σ_c (blue) and the line $w - c$ (red), or alternatively as the roots of $f(\omega)$ (yellow). σ_c is a construct of peaks, situated at the poles of the self-energy correlation Σ_c. As η becomes smaller ((A) $\rightarrow$(B)), the peaks become steeper. Each peak contributes up to three solutions to the QP equation. As η becomes smaller, these three solutions converge to the pole corresponding to their peak.

The derivative is then given by:

$$\sigma_c'(\omega) = \frac{[E(\omega)^2 + \eta^2] \cdot R - RE(\omega) \cdot 2E(\omega)}{[E(\omega)^2 + \eta^2]^2} = -\frac{E(\omega)^2 - \eta^2}{[E(\omega)^2 + \eta^2]^2} R. \tag{3.65}$$

We note that $E(\omega)^2 > 0$, $\eta^2 > 0$ and $R > 0$ such that $\sigma_c'(\omega) < 0$ if $E(\omega)^2 > \eta^2$. In other words, σ_c is usually decreasing except at the peaks where $|E(\omega)| < \eta$, which are situated at the poles of of the self-energy correlation Σ_c. We further note that, if $|E(\omega)| \ll \eta$, we have $\mathcal{O}(\sigma_c'(\omega)) = \mathcal{O}(\eta^{-1})$, with $0 < \eta \ll 1$. In other words, as η becomes smaller, the peaks become steeper. A sketch of the real part of the self-energy correlation $\sigma_c(\omega)$ is shown in Figure 3.1.

We now return our attention to solving the QP equation (Equation 3.62). To further simplify the notation, we define:

$$f(\omega) := \sigma_c(\omega) - \omega + c, \qquad c := \varepsilon_{\text{KS}} + \sigma_x - \nu_{\text{XC}}. \tag{3.66}$$

Both functions $\sigma_c(\omega)$ and $f(\omega)$ are defined and continuous over the entire real axis. Equation 3.62 can be seen as an intersection of the function $\sigma_c(\omega)$ with the line $\omega - c$, or alternatively as a root-finding problem of the function $f(\omega)$.

An initial guess of the solution is available, namely the KS energies $\varepsilon_{\mathrm{KS}}$. We can therefore apply one-point iterative root-finding methods such as the fixed-point method or Newton's method. Of course, we can also find a solution through brute force evaluation of $f(\omega)$ on a grid. We may find multiple solutions to our problem, but we are specifically looking for the solution related to the coherent part of the spectral function (Equation 2.50). This is because the coherent part is assumed to be centered around the QP energy, as shown in Figure 2.5. part of the spectral function (Equation 2.50). Recall that we already assume that the QP energy is close to the KS energy. We can therefore state that the desired solution is likely near our initial guess $\varepsilon_{\mathrm{KS}}$. In the following, we explore various root-finding methods for the purpose of solving the QP equation.

3.4.1 Fixed-Point Method

Finding the roots of $f(\omega)$ is equivalent to finding the fixed-points of $g(\omega) := f(\omega) + \omega$:

$$f(\omega) = 0 \quad \equiv \quad g(\omega) = \omega, \quad \text{where} \quad g(\omega) := f(\omega) + \omega = \sigma_c(\omega) + c. \tag{3.67}$$

We assume the existence of fixed-points of $g(\omega)$. According to the fixed-point method, we can find the local fixed-point ω^* using the following algorithm:

1. Obtain the starting guess $\omega_0 = \varepsilon_{\mathrm{KS}}$ through DFT.
2. Compute the next iterate according to $\omega_n = g(\omega_{n-1})$.
3. Repeat step 2 until $|\omega_n - \omega_{n-1}|$ is smaller than the tolerance ϵ.

The mean value theorem states that, for the continuous function $f(x)$, we have

$$f'(\xi) = (f(a) - f(b))/(a - b), \tag{3.68}$$

for some value $\xi \in (a, b)$, $a, b \in \mathbb{R}$, where

$$f'(\omega) = \frac{\mathrm{d}}{\mathrm{d}\omega}\left(\sigma_c(\omega) - \omega + c\right) = \sigma_c'(\omega) - 1, \tag{3.69}$$

and with $\sigma_c'(\omega)$ defined in Equation 3.65. By setting $a = \omega^*$, $b = \omega_{n-1}$ and rearranging, we rewrite Equation 3.68 into:

$$\sigma_c(\omega^*) - \sigma_c(\omega_{n-1}) = f'(\xi)(\omega^* - \omega_{n-1}). \tag{3.70}$$

Using $\omega_n = \sigma_c(\omega_{n-1}) + c$ and by taking the absolute value, we find

$$|\omega^* - \omega_n| = |\sigma_c(\omega^*) - \sigma_c(\omega_{n-1})| = |f'(\xi)||(\omega^* - \omega_{n-1})|. \tag{3.71}$$

So, if $|f'(\xi)| < 1$, the method converges to the fixed-point ω^*. The fixed-point method may "overshoot" the fixed-point (i.e. diverge) if the derivatives are large. This occurs when $\eta \to 0$ (see Figure 3.1). While this method is simple and inexpensive, we cannot guarantee convergence to a fixed-point. Visual examples of converging and non-converging fixed-point iterations are shown in Figure 3.2 (A) and (B) respectively.

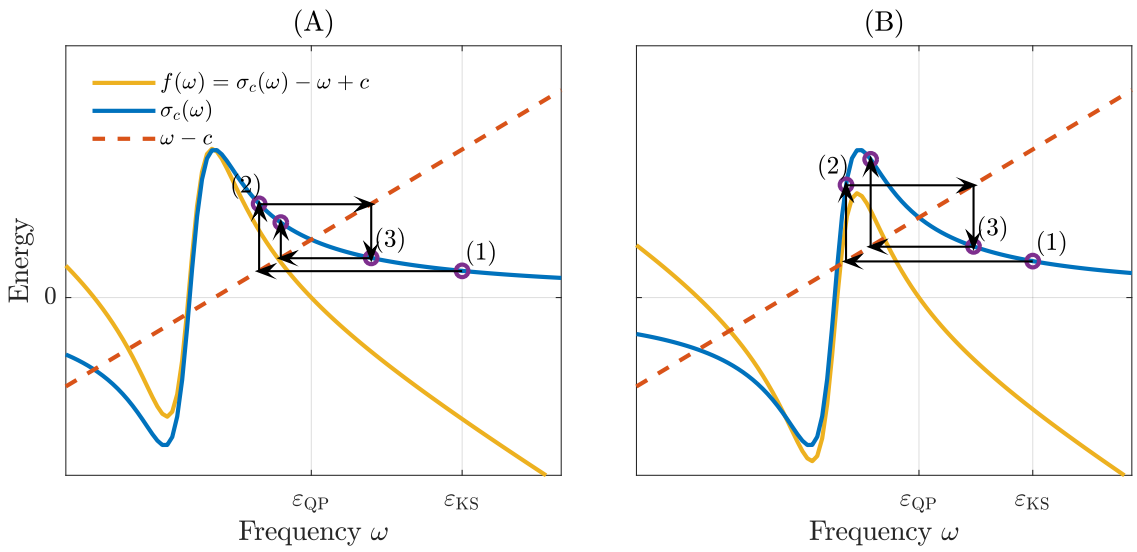

Figure 3.2: A sketch of the self-energy correlation function $\sigma_c(\omega)$ with the line $\omega - c$. Using the fixed-point method, we aim to find the QP energy $\varepsilon_{\mathrm{QP}}$ at the point-of-intersection, using an initial guess (1) of the KS energy $\varepsilon_{\mathrm{KS}}$. The next iterates (2) and (3) are computed using the fixed-point method. Two scenarios are shown. (A) The scenario where the fixed-point method converges from the KS energy $\varepsilon_{\mathrm{KS}}$ to the desired QP energy $\varepsilon_{\mathrm{QP}}$. (B) The scenario where the fixed-point method does not converge.

3.4.2 Newton's Method

Newton's method is a root-finding algorithm which produces successively better estimates of the root ω^* of $f(\omega)$ using the derivative $f'(\omega)$. We can find an improved estimate ω_n using the previous guess ω_{n-1} via:

$$\omega_n = \omega_{n-1} - \frac{f(\omega_{n-1})}{f'(\omega_{n-1})}, \quad \text{where} \quad f'(\omega) = \frac{\mathrm{d}}{\mathrm{d}\omega}\left(\sigma_c(\omega) - \omega + c\right) = \sigma_c'(\omega) - 1, \tag{3.72}$$

with $\sigma_c'(\omega)$ defined in Equation 3.65. According to Newton's method, we can find the local root ω^* using the following algorithm:

1. Obtain the starting guess $\omega_0 = \varepsilon_{\mathrm{KS}}$ through DFT.
2. Compute the next iterate according to Equation 3.72.
3. Repeat step 2 until $|\omega_n - \omega_{n-1}|$ is smaller than the tolerance ϵ.

We can express the root in a Taylor expansion around out current guess ω_{n-1}:

$$f(\omega^*) = 0 = f(\omega_{n-1}) + f'(\omega_{n-1})(\omega^* - \omega_{n-1}) + \frac{1}{2}f''(\omega_{n-1})(\omega^* - \omega_{n-1})^2 + R. \tag{3.73}$$

By assuming that estimate ω_{n-1} is sufficiently close to the root ω^* and that the higher order terms are negligible ($R \to 0$), and subsequently dividing both sides by $f'(\omega_{n-1})$, we find:

$$\frac{f(\omega_{n-1})}{f'(\omega_{n-1})} + (\omega^* - \omega_{n-1}) = -\frac{f''(\omega_{n-1})}{2f'(\omega_{n-1})}(\omega^* - \omega_{n-1})^2. \tag{3.74}$$

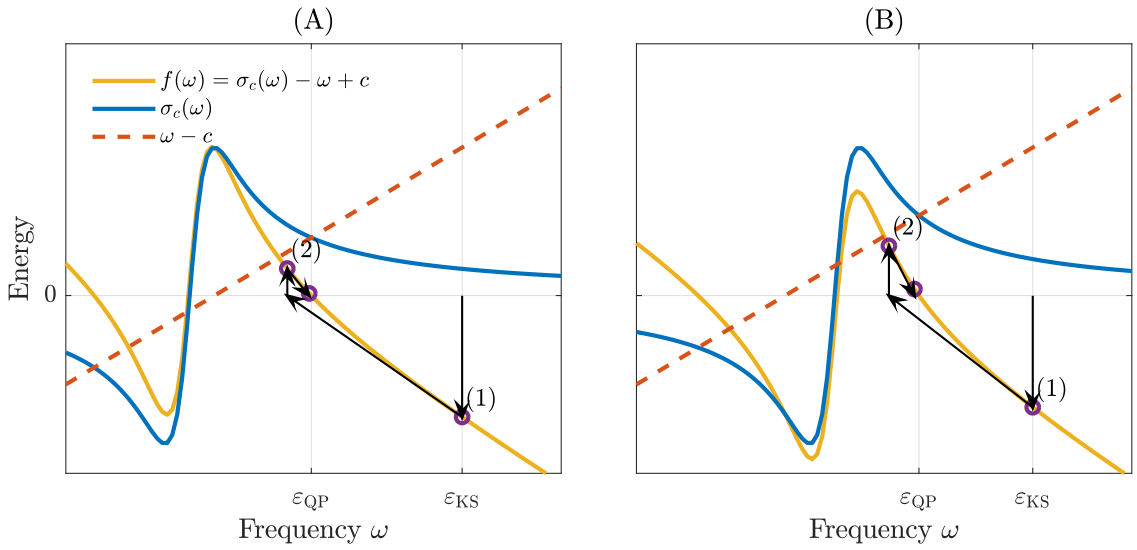

Figure 3.3: A sketch of the self-energy correlation function $\sigma_c(\omega)$ with the line $\omega - c$. Using Newton's method, we aim to find the QP energy $\varepsilon_{\mathrm{QP}}$ at the point-of-intersection, using an initial guess (1) of the KS energy $\varepsilon_{\mathrm{KS}}$. The next iterate (2) is computed using Newton's method. In both scenarios (A) and (B), Newton's method converges.

We substitute Equation 3.72 to find:

$$\omega^* - \omega_n = -\frac{f''(\omega_{n-1})}{2f'(\omega_{n-1})}(\omega^* - \omega_{n-1})^2 \tag{3.75}$$

From this equation follows the evolution of the error $\epsilon_i := \omega^* - \omega_i$:

$$\epsilon_n = -\frac{f''(\omega_{n-1})}{2f'(\omega_{n-1})}\epsilon_{n-1}^2. \tag{3.76}$$

So, if the assumptions hold, the rate of convergence is quadratic. Newton's method may "overshoot" the root (i.e. diverge), if the derivatives are large. This occurs when $\eta \to 0$ (see Figure 3.1). While we can easily compute $\sigma_c'(\omega)$ and the rate of convergence is quadratic in the best case scenario, we cannot guarantee convergence to a root. Visual examples of Newton iterations are shown in Figure 3.3 (A) and (B) respectively.

3.4.3 Grid Method

If the above iterative methods fail to converge, we can always resort to brute forcing a solution. To this end, we evaluate the target function $f(\omega)$ on a uniformly spaced grid, centered at the initial guess $\varepsilon_{\mathrm{KS}}$. Let N_g denote the number of grid points and $\Delta\omega$ the spacing between each grid point. Then

$$\omega_j = \varepsilon_{\mathrm{KS}} + \left(j - 1 - \left\lfloor \frac{N_g - 1}{2} \right\rfloor\right) \cdot \Delta\omega, \quad f_j = f(\omega_j), \quad j = 1, 2, \ldots, N_g.$$

By increasing the spacing $\Delta\omega$, we increase the search range but reduce the resolution of the grid and therefore also the accuracy of the root estimate. By increasing the number of grid points N_g, we improve the resolution of the grid, but increase the computational cost. For every interval $[j, j+1]$, we determine whether it contains a root by detecting a sign-change in the target function, i.e. $f_j \cdot f_{j+1} < 0$. If the interval contains a root, the location of the root ω^* can be estimated via e.g. a mean computation, or a Newton iteration:

$$\omega^*_{\text{mean}} = (\omega_j + \omega_{j+1})/2, \qquad \omega^*_{\text{fixed-point}} = \omega_j - \frac{f_j}{f'_j} \approx \omega_j - \frac{f_j}{\Delta f/\Delta\omega}.$$

We rank every detected root by their quasi-particle weight Z_{QP}, defined by Equation 2.51, where we estimate the derivative:

$$\frac{\mathrm{d}\Sigma(\omega)}{\mathrm{d}\omega} = \frac{\mathrm{d}\Sigma_c(\omega)}{\mathrm{d}\omega} \approx \frac{f_{j+1} - f_j}{w_{j+1} - w_j}. \tag{3.77}$$

We select the root associated to the largest quasi-particle weight. We assume that this root corresponds to the coherent part of the spectral function (Equation 2.50).

While the grid method is simple and robust, it requires many function evaluations. Furthermore, the accuracy of the solution is limited to the grid resolution; the solution cannot be "improved" until the desired convergence criterion is reached (unlike the previously discussed iterative methods). One way to circumvent this issue is to follow-up with a bounded iterative method, e.g. the bisection method.

Chapter 4

Practical Implementation

We discussed the methodology behind the GW step of DFT-GW-BSE. We subdivided the GW step into two parts: (1) computing the self-energy Σ by evaluating the GW convolution (Equation 3.43) and (2) computing the QP energies $\varepsilon_{\mathrm{QP}}$ by solving the QP equation (Equation 3.61). Furthermore, we proposed two ways for calculating the self-energy:

1. We can evaluate the GW convolution analytically by diagonalizing $\underline{\mathbf{H}}^{2\mathrm{p}}$ and subsequently transforming the reducible polarizability χ into its spectral representation [27]. While this is the most accurate approach, it is also the most computationally demanding. This method is referred to as the *Fully-Analytical Approach*, or *FAA*. The bottleneck of this method is the diagonalization of $\underline{\mathbf{H}}^{2\mathrm{p}}$, which scales with $\mathcal{O}(N^6)$.

2. We can simplify the frequency-dependence of the GW convolution by approximating the dielectric function ϵ using a Plasmon-Pole Model (PPM) [30]. The simplified GW convolution is then evaluated analytically. This method is referred to as the *Plasmon-Pole Model*, or *PPM*. The bottleneck of this method is the computation of the *plasmon-pole*, i.e. its frequency ω_ℓ and corresponding weight z_ℓ, which scales with $\mathcal{O}(N^4)$.

In this thesis, we implement the FAA for the GW step of DFT-GW-BSE. Our implementation will be part of the VOTCA-XTP library. The PPM is already implemented in VOTCA-XTP and provides a point of reference.

The VOTCA-XTP library is written in the C++ programming language. C++ is versatile in that it provides excellent object-oriented features in addition to low-level memory manipulations. It further is among the best programming languages in raw performance, which makes it a very suitable choice for running the expensive quantum mechanical calculations.

The VOTCA-XTP library relies heavily on the Eigen3 linear algebra library [31]. Eigen3 offers abstract and vectorizable code, which allows us to implement large scale matrix operations that greatly outperform manual implementations using conventional loops. This performance boost is achieved through a number of factors, e.g. by employing SIMD instructions, smart algorithms and multi-threading. For even higher performance, we link Eigen3 with the Intel MKL library, which is a highly optimized BLAS/LAPACK library for Intel

chip sets. Finally, we employ the OpenMP library to distribute the computational workload of our calculations over multiple threads.

In the Eigen3 library, all of the data in a matrix is guaranteed to be contiguous in memory and, by default, in column-major order. In memory, this means that the matrix is stored as a sequence of chunks, where each chunk contains the data of one column. The data structure is best traversed in the order in which they are stored. This is an important consideration to make when optimizing code because iteration or extraction on a column is significantly faster than doing the same operation on a row.

Through performance analysis using Intel VTune Amplifier [32], inefficient code constructs are detected and systematically removed.

Chapter 5

Results

In this chapter, we benchmark the accuracy and performance of the FAA. We aim to answer the following questions:

1. First and foremost; is the FAA implemented correctly? Can we reproduce the results of an independent, and verified, QM package using our implementation in VOTCA-XTP? Specifically, how does our implementation compare to MOLGW [27]? MOLGW is a QM package that implements the many-body perturbation theory (MBPT) to describe the excited states. Most importantly, it implements the FAA for the GW procedure. We investigate this question in Sections 5.1 and 5.2.

2. What are the advantages and disadvantages of the FAA with respect to the approximate PPM? Which method offers the greatest degree of accuracy for a reasonable computational cost? Specifically, are there situations in which the increase in computational cost of the analytical method outweighs the gain in accuracy with respect to the approximate method? We investigate this question in Section 5.3.

All calculations are performed on the molecules in the *Thiel set* [33]. The Thiel set is composed of 28 small molecules which can be sorted into the four categories: (1) aldehydes, ketones, amides, (2) aromatic hydrocarbons and heterocycles, (3) nucleobases, and (4) unsaturated aliphatic hydrocarbons. The smallest molecule, at 4 atoms, is formaldehyde and the largest, at 18 atoms, is naphthalene. The molecules cover three important types of electronic transitions: $\sigma \rightarrow \sigma^*$, $\pi \rightarrow \pi^*$ and $\sigma \rightarrow \pi^*$.

Thiel et al. proposed the best theoretical estimates for 104 singlet and 63 triplet excitation energies among these molecules. These estimates are found using the best and most expensive higher order methods, such as CCSDT, and are compiled in the TBE-2 dataset. In order to gauge the accuracy of our GW-BSE implementation, we can compare our energies to TBE-2 estimates. Such a comparison was also made in a study by Blase et al. [34].

5.1 MOLGW Comparison: Ethene Case Study

In this section, we investigate the ground state and excited state properties of ethene. Ethene is classified as an unsaturated aliphatic hydrocarbon and its molecule composition is given by C_2H_4, or $H_2C{=}CH_2$. Its molecular structure is depicted in Figure 5.1.

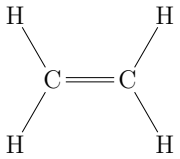

Figure 5.1: The molecule structure of ethene.

Since ethene is such a small molecule, it requires a relatively small number of basis functions to accurately model its MOs. Consequently, GW-BSE calculations on the molecule are cheap, making ethene a suitable test subject. All calculations are performed using the `cc-pVTZ` basis set and its corresponding `aux-cc-pVTZ` auxiliary basis set. In this basis, the first 116 of ethene's real MOs are accounted for. Figure 5.2 provides a picture of some MOs of ethene.

We calculate the KS energies ε_{KS}, the QP energies ε_{QP} and finally several neutral excitation energies Ω of ethene. The results are compared to MOLGW [27]. MOLGW is QM package that implements the many-body perturbation theory (MBPT) to describe the excited states. Most importantly, it implements the FAA for the GW procedure. MOLGW has been extensively tested on a large variety of molecules and it therefore provides a valuable benchmark.

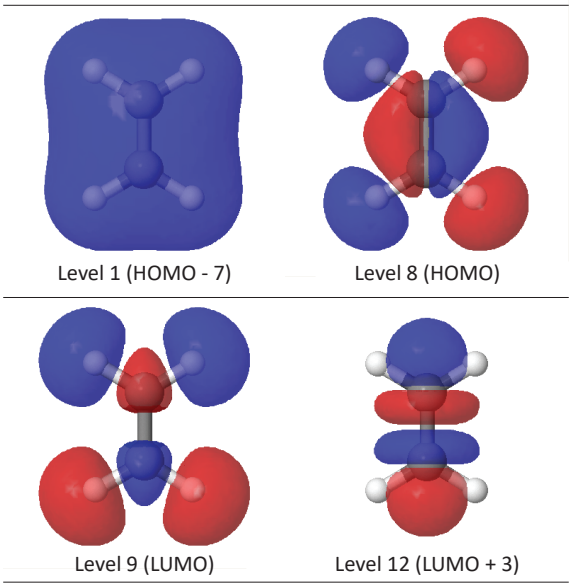

Figure 5.2: Molecular orbitals of ethene. The first row shows MOs which are occupied in the ground state and the second row shows MOs which are unoccupied in the ground state, but may be occupied in excited states. The wave function is positive in the red regions and negative in the blue regions.

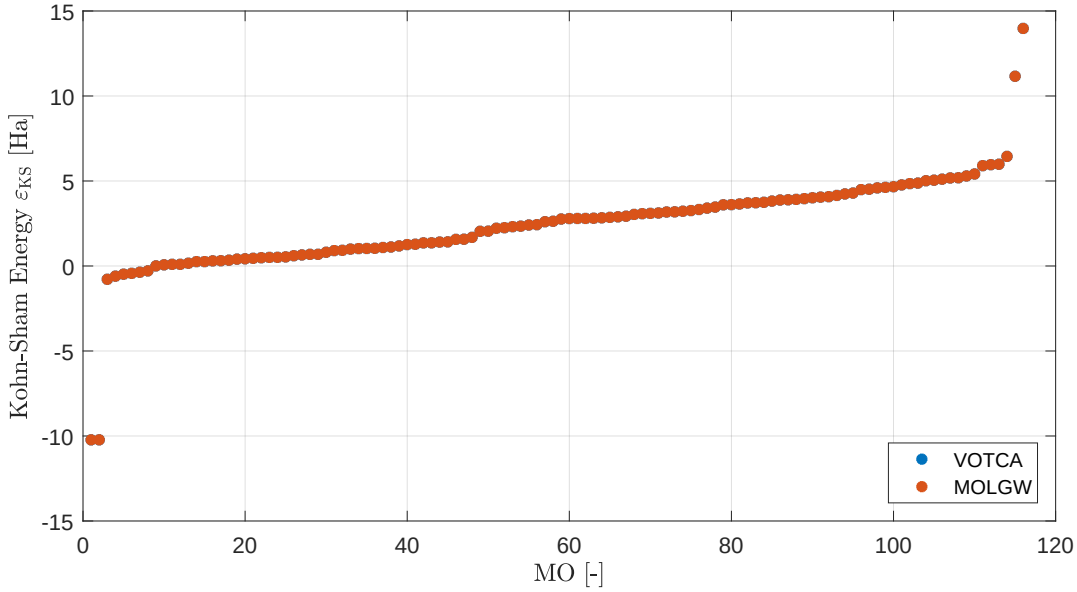

Figure 5.3: A comparison of the KS energies ε_{KS} of ethene calculated by VOTCA and MOLGW versus the MO index. The KS energies are calculated self-consistently according to the KS scheme (Equation 2.37), using a tolerance of $\epsilon = 10^{-7}$ Ha. The resulting KS energies are shifted such that zero energy marks half of the HOMO-LUMO gap. The KS energies match sufficiently well that the markers overlap on this y-scale.

5.1.1 Ground-State Kohn-Sham Energies

The Kohn-Sham (KS) energies are calculated self-consistently according to the KS scheme (Equation 2.37), using a tolerance of $\epsilon = 10^{-7}$ Ha. The resulting KS energies are arbitrarily shifted such that zero energy marks half of the HOMO-LUMO gap. A visual comparison of the KS energies between VOTCA and MOLGW is shown in Figure 5.3. Furthermore, the KS energies of the first 16 MOs are reported in Table 5.1. We observe errors in the order of 10^{-4} Ha. The KS energies serve only as an initial guess to the QP energies. Therefore, these errors do not necessarily affect the QP energies.

5.1.2 Self-Energy Correlation

The self-energy correlation function Σ_c is given by Equation 3.53, where we set $\eta = 10^{-3}$ Ha. We evaluate Σ_c at the QP energies calculated by MOLGW, which we symbolically denote as: $\Sigma_c(\varepsilon_{\text{QP}}^{\text{MOLGW}})$. Visual comparisons of the self-energy correlation between VOTCA and MOLGW are shown in Figures 5.4 and 5.5. Furthermore, the self-energy correlation corresponding to the first 16 MOs are reported in Table 5.2. For the low-energy MOs, we observe errors in the order of 10^{-4} Ha. For the higher-energy MOs, however, the errors grow to the order of 10^{-2} Ha. Since the input energies were set equal, these errors suggest different implementations of the self-energy function between VOTCA and MOLGW. Errors in Σ_c will affect the QP energies.

Table 5.1: The KS energies $\varepsilon_{\mathrm{KS}}$ of the first 16 MOs of ethene calculated by VOTCA and MOLGW. The "Difference" column contains the energy differences between the VOTCA and MOLGW results. The "Increment" column contains the energy increment between every two consecutive MOs, calculated by VOTCA. The MSE (Mean Signed Error) and MAE (Mean Absolute Error) of $\varepsilon_{\mathrm{QP}}^{\mathrm{VOTCA}}$ w.r.t. $\varepsilon_{\mathrm{QP}}^{\mathrm{MOLGW}}$ are given below.

MO [-]	$\varepsilon_{\mathrm{KS}}^{\mathrm{MOLGW}}$ [Ha]	$\varepsilon_{\mathrm{KS}}^{\mathrm{VOTCA}}$ [Ha]	Difference [Ha]	Increment [Ha]
1	-10.226285	-10.226300	-0.000015	-
2	-10.225366	-10.225400	-0.000034	0.000919
3	-0.783220	-0.783300	-0.000080	9.442146
4	-0.598541	-0.598600	-0.000059	0.184679
5	-0.483136	-0.483200	-0.000064	0.115405
6	-0.433338	-0.433400	-0.000062	0.049798
7	-0.367125	-0.367100	0.000025	0.066213
HOMO	-0.287352	-0.287400	-0.000048	0.079774
LUMO	0.005676	0.005700	0.000024	0.293028
10	0.068650	0.068600	-0.000050	0.062973
11	0.096555	0.096500	-0.000055	0.027905
12	0.097435	0.097400	-0.000035	0.000880
13	0.161639	0.161600	-0.000039	0.064204
14	0.257713	0.257700	-0.000013	0.096074
15	0.258458	0.258500	0.000042	0.000745
16	0.301250	0.301100	-0.000150	0.042792
$17-116$	...	...	...	...
Low-energy MOs (MO ≤ 16)				
MSE		$-3.811756 \cdot 10^{-5}$		
MAE		$+4.952668 \cdot 10^{-5}$		
All MOs (MO $\in [1, 116]$)				
MSE		$-2.880831 \cdot 10^{-5}$		
MAE		$+1.507337 \cdot 10^{-4}$		

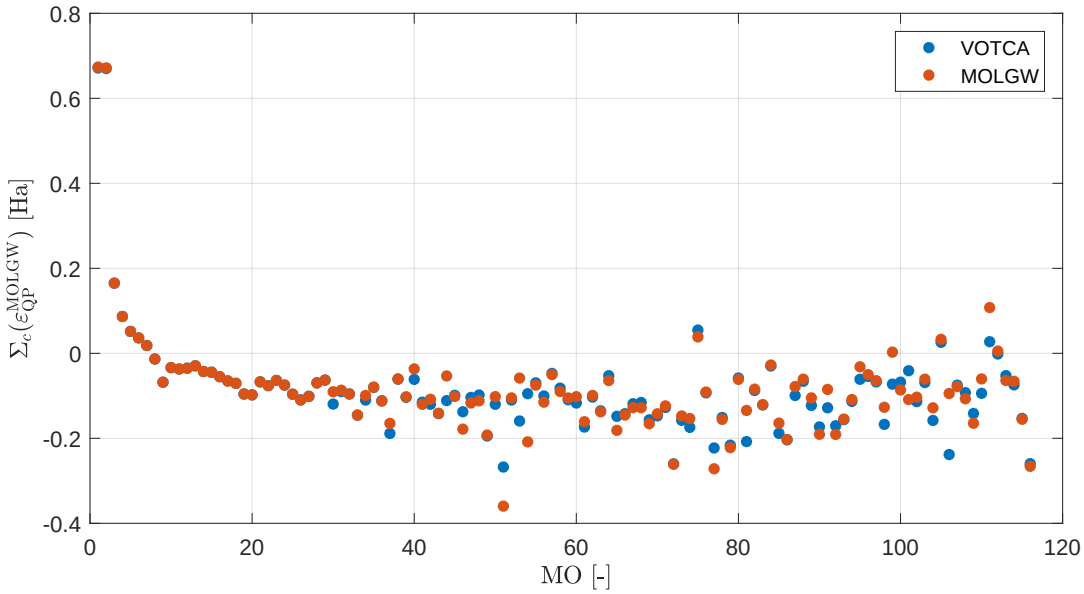

Figure 5.4: A comparison of the real part of the self-energy correlation Σ_c of ethene calculated by VOTCA and MOLGW versus the MO index. We set the "small" imaginary number to $\eta = 10^{-3}$ Ha. The self-energy correlation is evaluated at the QP energies calculated by MOLGW, which we symbolically denote as: $\Sigma_c(\varepsilon_{\rm QP}^{\rm MOLGW})$.

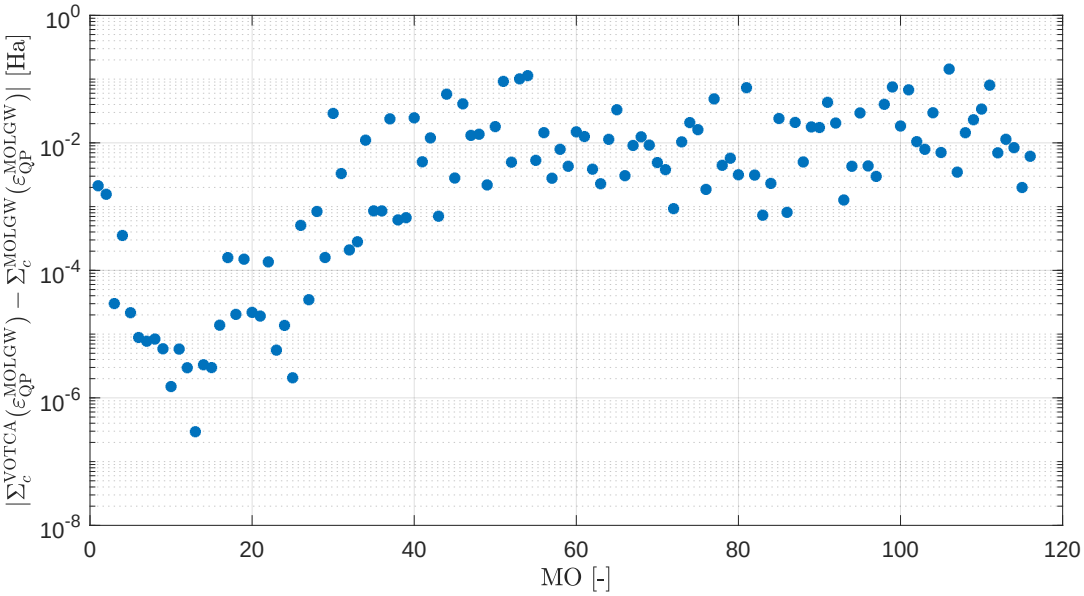

Figure 5.5: The difference between the real part of the self-energy correlation Σ_c of ethene calculated by VOTCA and MOLGW versus the MO index. We set the "small" imaginary number to $\eta = 10^{-3}$ Ha. The self-energy correlation is evaluated at the QP energies calculated by MOLGW, which we symbolically denote as: $\Sigma_c^{VOTCA}(\varepsilon_{\rm QP}^{\rm MOLGW})$ and $\Sigma_c^{\rm MOLGW}(\varepsilon_{\rm QP}^{\rm MOLGW})$ for the VOTCA and MOLGW results respectively.

Table 5.2: The real part of the self-energy correlation Σ_c of the first 16 MOs of ethene calculated by VOTCA and MOLGW. We set the "small" imaginary number to $\eta = 10^{-3}$ Ha. The self-energy correlation is evaluated at the QP energies calculated by MOLGW, which we symbolically denote as: $\Sigma_c^{VOTCA}(\cdot)$ and $\Sigma_c^{\mathrm{MOLGW}}(\cdot)$ for the VOTCA and MOLGW results respectively. The "Difference" column contains the energy differences between the VOTCA and MOLGW results. The MSE (Mean Signed Error) and MAE (Mean Absolute Error) of $\Sigma_c^{\mathrm{VOTCA}}$ w.r.t. $\Sigma_c^{\mathrm{MOLGW}}$ are given below.

MO [-]	$\Sigma_c^{\mathrm{MOLGW}}(\cdot)$ [Ha]	$\Sigma_c^{\mathrm{VOTCA}}(\cdot)$ [Ha]	Difference [Ha]
1	0.673479	0.671356	−0.002123
2	0.671605	0.670044	−0.001561
3	0.165081	0.165051	−0.000030
4	0.086467	0.086819	0.000352
5	0.051499	0.051477	−0.000022
6	0.036306	0.036297	−0.000009
7	0.018421	0.018413	−0.000008
HOMO	−0.013415	−0.013423	−0.000008
LUMO	−0.067993	−0.067999	−0.000006
10	−0.033701	−0.033699	0.000002
11	−0.036935	−0.036941	−0.000006
12	−0.034986	−0.034989	−0.000003
13	−0.029361	−0.029361	0.000000
14	−0.042770	−0.042767	0.000003
15	−0.044552	−0.044549	0.000003
16	−0.054992	−0.054978	0.000014
17 − 116	...	...	...
Low-energy MOs (1:16)			
MSE		$-2.125870 \cdot 10^{-4}$	
MAE		$+2.593844 \cdot 10^{-4}$	
All MOs (:)			
MSE		$-3.368724 \cdot 10^{-3}$	
MAE		$+1.473026 \cdot 10^{-2}$	

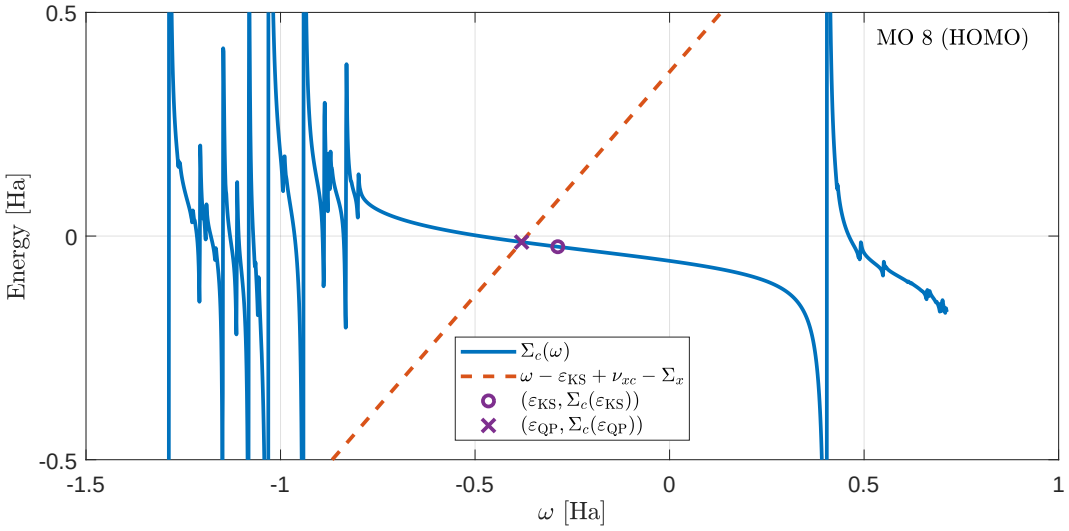

Figure 5.6: A visualization of the QP equation for the HOMO of ethene. The QP energy ε_{QP} (purple cross) is found at the point-of-intersection of the self-energy correlation Σ_c (blue line) with $\omega - \varepsilon_{\text{KS}} - \Sigma_x + \nu_{xc}$ (red dashed line). The initial guess of the solution is given by the KS energy ε_{KS} (purple circle), obtained through a preceding DFT calculation. The self-energy correlation is evaluated using $\eta = 10^{-3}$ Ha.

5.1.3 Quasi-Particle Excitation Energies

The Quasi-Particle (QP) excitation energies are calculated by solving the QP equation (Equation 3.61) using the one-shot GW, or G_0W_0, approach. In Figure 5.6, we plot Σ_c of the HOMO as a function of the energy (/frequency) ω, near the KS energy. In this plot, the solution to the QP equation is marked by the intersection of Σ_c with the line $\omega - \varepsilon_{\text{KS}} + \nu_{\text{XC}} - \Sigma_x$. We solve the QP equation via the brute-force grid approach (Section 3.4.3), where we use $N_g = 1001$ grid points and a step size of $\Delta\omega = 10^{-3}$ Ha. Visual comparisons of the QP energies between VOTCA and MOLGW are shown in Figures 5.7 and 5.8. Furthermore, the KS energies, QP energies and the self-energy correlation of the first 16 MOs are reported in Table 5.3. Recall that the relative accuracy of the QP energies is limited to the grid resolution of 10^{-3} Ha. At least for the first 16 MOs, the relative errors in QP energies are well below the grid resolution. The errors increase for the higher-energy MOs. The errors of order 10^{-2} Ha may be caused by the previously observed differences in Σ_c.

5.1.4 Neutral Excitation Energies

Finally, the neutral excitation energies Ω are calculated using the BSE implementations of VOTCA and MOLGW. The first 20 neutral MOs are reported in Table 5.4. We observe an MAE of 0.04848 eV $= 1.7816 \cdot 10^{-3}$ Ha. Recall that neutral excitation energies are eigenvalues of the BSE matrix. Since the BSE matrix is of the same order as the QP energies, the error in QP energies carry over one-to-one to the neutral excitation energies. We can therefore conclude that the neutral excitation energies are accurate up to the grid resolution of 10^{-3} Ha.

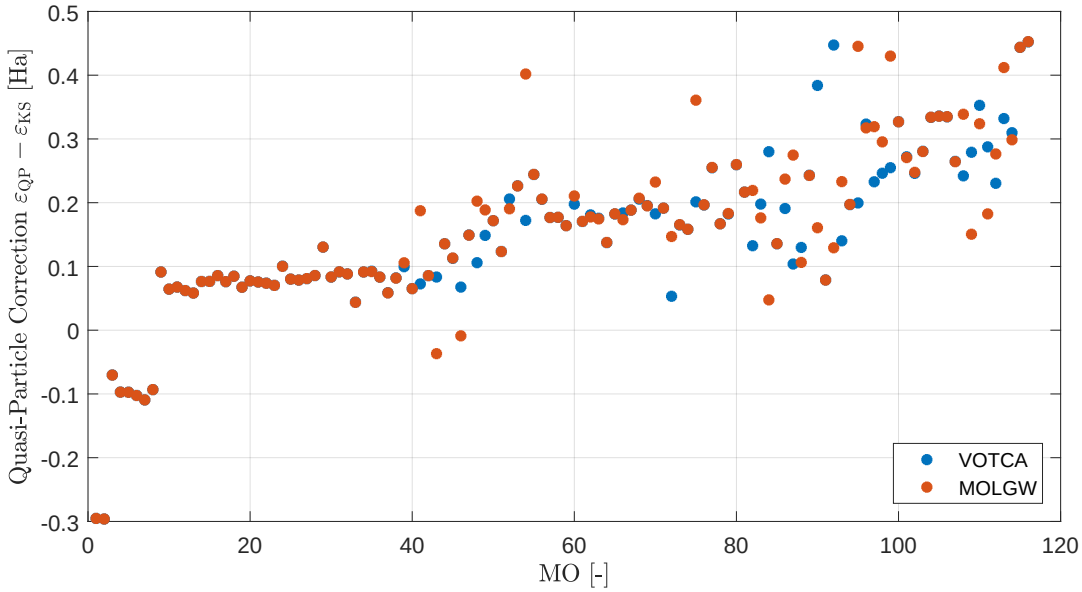

Figure 5.7: A comparison of the QP corrections $\varepsilon_{\mathrm{QP}} - \varepsilon_{\mathrm{KS}}$ of ethene calculated by VOTCA and MOLGW versus the MO index. The self-energy correlation is evaluated using $\eta = 10^{-3}$ Ha. The QP equation is solved on a grid with $N_g = 1001$ grid points and a step size of $\Delta\omega = 10^{-3}$ Ha, using the one-shot GW, or G_0W_0, approach.

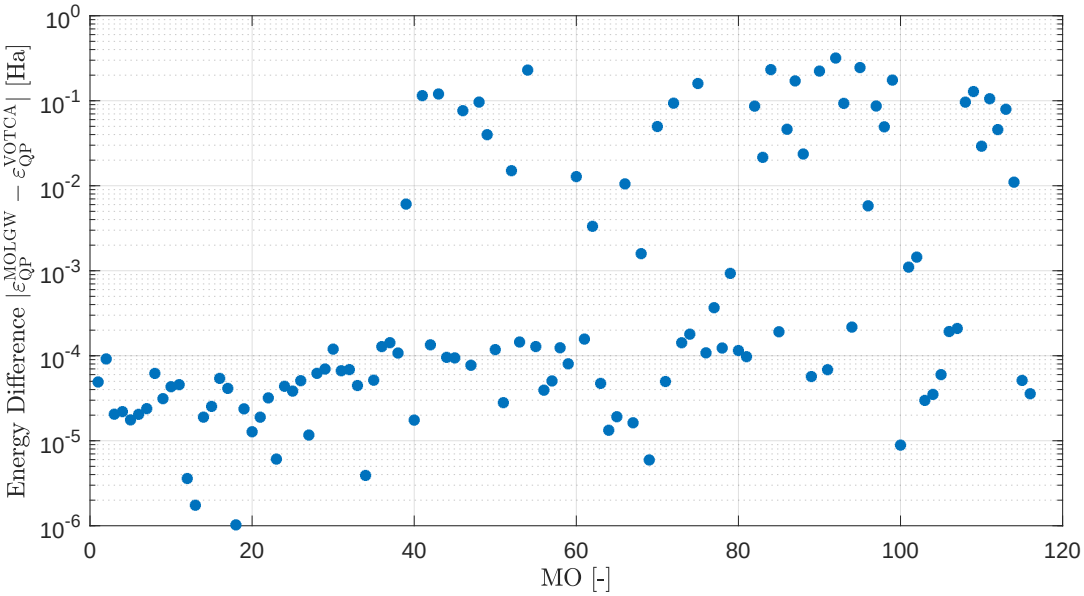

Figure 5.8: The difference between the QP energies of ethene calculated by VOTCA and MOLGW versus the MO index. The self-energy correlation is evaluated using $\eta = 10^{-3}$ Ha. The QP equation is solved on a grid with $N_g = 1001$ grid points and a step size of $\Delta\omega = 10^{-3}$ Ha, using the one-shot GW, or G_0W_0, approach.

Table 5.3: The DFT, GW results-KS energies $\varepsilon_{\mathrm{KS}}$, QP energies $\varepsilon_{\mathrm{QP}}$, self-energy correlation Σ_c-of the first 16 MOs of ethene calculated by VOTCA and MOLGW. The self-energy correlation is evaluated using $\eta = 10^{-3}$ Ha. The QP equation is solved on a grid with $N_g = 1001$ grid points and a step size of $\Delta\omega = 10^{-3}$ Ha, using the one-shot GW, or G_0W_0, approach. The MSE (Mean Signed Error) and MAE (Mean Absolute Error) of VOTCA w.r.t. MOLGW are given below.

MO [-]	$\varepsilon_{\mathrm{KS}}$ [Ha]		$\varepsilon_{\mathrm{QP}}$ [Ha]		$\Sigma_c(\varepsilon_{\mathrm{QP}})$ [Ha]	
	MOLGW	VOTCA	MOLGW	VOTCA	MOLGW	VOTCA
1	−10.22629	−10.22630	−10.52155	−10.52160	0.67283	0.67280
2	−10.22537	−10.22540	−10.52151	−10.52160	0.67112	0.67110
3	−0.78322	−0.78330	−0.85362	−0.85360	0.16508	0.16510
4	−0.59854	−0.59860	−0.69568	−0.69570	0.08670	0.08670
5	−0.48314	−0.48320	−0.58052	−0.58050	0.05149	0.05150
6	−0.43334	−0.43340	−0.53578	−0.53580	0.03630	0.03630
7	−0.36713	−0.36710	−0.47648	−0.47650	0.01842	0.01840
HOMO	−0.28735	−0.28740	−0.38054	−0.38060	−0.01342	−0.01340
LUMO	0.00568	0.00570	0.09697	0.09700	−0.06799	−0.06800
10	0.06865	0.06860	0.13304	0.13300	−0.03370	−0.03370
11	0.09655	0.09650	0.16425	0.16420	−0.03693	−0.03690
12	0.09743	0.09740	0.15960	0.15960	−0.03498	−0.03500
13	0.16164	0.16160	0.21990	0.21990	−0.02936	−0.02940
14	0.25771	0.25770	0.33408	0.33410	−0.04277	−0.04280
15	0.25846	0.25850	0.33497	0.33500	−0.04455	−0.04450
16	0.30125	0.30110	0.38685	0.38680	−0.05499	−0.05500
17 − 116	...	...	...	...	...	...
Low-energy MOs (1:16)						
MSE	$-3.81176 \cdot 10^{-5}$		$-1.83274 \cdot 10^{-5}$		$-3.36242 \cdot 10^{-6}$	
MAE	$+4.95267 \cdot 10^{-5}$		$+3.32078 \cdot 10^{-5}$		$+1.99265 \cdot 10^{-5}$	
All MOs (:)						
MSE	$-2.88083 \cdot 10^{-5}$		$-5.68125 \cdot 10^{-3}$		$-5.67250 \cdot 10^{-3}$	
MAE	$+1.50734 \cdot 10^{-4}$		$+2.85555 \cdot 10^{-2}$		$+2.85558 \cdot 10^{-2}$	

Table 5.4: The first 20 neutral excitation energies Ω of ethene calculated by VOTCA and MOLGW. The self-energy correlation is evaluated using $\eta = 10^{-3}$ Ha. The QP equation is solved on a grid with $N_g = 1001$ grid points and a step size of $\Delta\omega = 10^{-3}$ Ha, using the one-shot GW, or G_0W_0, approach. The "Difference" column contains the energy differences between the VOTCA and MOLGW results. The *character* of each neutral excitation denotes the two-particle transition (from index →to index) it most resembles. The MSE (Mean Signed Error) and MAE (Mean Absolute Error) of Ω^{VOTCA} w.r.t. Ω^{MOLGW} are given below.

MO [-]	Ω [eV]		Difference [eV]	Character [-]	
	MOLGW	VOTCA		MOLGW	VOTCA
1	7.486875	7.465671	−0.021204	$8 \to 9$	$8 \to 9$
2	8.039130	8.104795	0.065665	$8 \to 10$	$8 \to 10$
3	8.132460	8.116415	−0.016045	$7 \to 9$	$7 \to 9$
4	8.708033	8.847517	0.139484	$8 \to 11$	$8 \to 11$
5	9.023771	9.087175	0.063404	$8 \to 12$	$8 \to 12$
6	9.413006	9.395047	−0.017959	$6 \to 9$	$6 \to 9$
7	10.628769	10.668895	0.040125	$7 \to 10$	$7 \to 10$
8	10.712836	10.733653	0.020817	$5 \to 9$	$5 \to 9$
9	10.974270	11.018571	0.044301	$8 \to 13$	$8 \to 13$
10	11.680821	11.724601	0.043780	$7 \to 12$	$7 \to 12$
11	11.749928	11.806526	0.056598	$7 \to 11$	$7 \to 11$
12	12.403402	12.450279	0.046877	$6 \to 10$	$6 \to 10$
13	12.960973	12.933415	−0.027558	$8 \to 15$	$8 \to 15$
14	12.969704	13.019653	0.049949	$6 \to 11$	$8 \to 14$
15	12.982286	13.088307	0.106020	$8 \to 14$	$6 \to 11$
16	13.183205	13.256363	0.073158	$6 \to 12$	$6 \to 12$
17	13.588237	13.617220	0.028982	$7 \to 13$	$7 \to 13$
18	13.649825	13.687510	0.037685	$5 \to 10$	$5 \to 10$
19	13.922399	13.866056	−0.056343	$8 \to 16$	$8 \to 16$
20	14.331375	14.317736	−0.013639	$5 \to 12$	$4 \to 9$
MSE		0.033205			
MAE		0.048480			

5.2 MOLGW Comparison: Thiel Set

We repeat the previous GW-BSE calculation for all molecules in the Thiel set. Specifically, we calculate the Mean-Absolute Error (MAE) of the QP energies and neutral energies, which we define as follows:

$$\mathrm{MAE}_{(*)} = \frac{1}{N_{\mathrm{MO}}} \sum\nolimits_{i=1}^{N_{\mathrm{MO}}} \left| \varepsilon_{(*),i}^{\mathrm{FAA}} - \varepsilon_{(*),i}^{\mathrm{PPM}} \right|, \tag{5.1}$$

where N_{MO} denotes the molecule size (i.e. the number of MOs) and $(*) \in \{\mathrm{QP}, \mathrm{neutral}\}$. The self-energy correlation is evaluated using $\eta = 10^{-3}$ Ha. The QP equation is solved on a grid with $N_g = 1001$ grid points and a step size of $\Delta\omega = 10^{-3}$ Ha, using the one-shot GW, or G_0W_0, approach.

The resulting MAEs are reported in Table 5.5. The lowest errors are observed in the Unsaturated Aliphatic Hydrocarbons category whereas the highest errors are observed in the Nucleobases category. In terms of relative accuracy of the first 16 QP energies, ethene is only the fourth most accurate molecule, behind butadiene, benzene and acetone, all of which are bigger than ethene. Importantly, ethene does not stand out as an exceptional case, reaffirming our conclusions from the previous section.

5.3 PPM Comparison: Accuracy and Performance.

In this section, we compare the accuracy and performance between the FAA and PPM implementations of VOTCA. To this end, we benchmark the Thiel set of molecules using both implementations. All calculations are performed using the `cc-pVTZ` basis set and its corresponding `aux-cc-pVTZ` auxiliary basis set. The DFT energies are converged up to a tolerance of $\epsilon = 10^{-7}$ Ha. In the FAA calculations, the self-energy correlation is evaluated using $\eta = 10^{-3}$ Ha. The QP equation is solved on a grid with $N_g = 1001$ grid points and a step size of $\Delta\omega = 10^{-3}$ Ha. The QP equation is solved either for 1 GW iteration (G_0W_0), or for 10 GW iterations ($evGW$).

In order compare the accuracy between FAA and PPM, we test our neutral excitation energies against the estimates in the TBE-2 dataset. Specifically, we calculate the first singlet (S_0) energies for all molecules in the Thiel set and compare these to TBE-2. Whichever method resembles the TBE-2 estimates the best is considered to be the most accurate of the two. The resulting singlet energies are reported in Table 5.6. The MAEs completely agree with the theory; the FAA yields more accurate energies than the approximate PPM and, simultaneously, the self-consistent $evGW$ approach yields more accurate energies than the one-shot G_0W_0 approach.

While the neutral excitation energies are the final result of the GW-BSE calculation, the FAA and PPM methods diverge from one another in the GW step. Therefore, in order to measure the difference between two methods, we compare the QP energies between both methods. For every molecule, we calculate the Mean Absolute Error (MAE) of the QP energies as defined in Equation 5.1. In Figure 5.9, we plot the MAE as a function of the molecule size N_{MO}. We observe a decrease in MAE as N_{MO} increases. This suggests that the approximate PPM results approach the theoretical QP energies better for increasingly larger molecules.

Table 5.5: The Mean Absolute Error (MAE) in Ha of the QP energies and neutral energies between the FAA and MOLGW (Equation 5.1), for all molecules in the Thiel set. The self-energy correlation is evaluated using $\eta = 10^{-3}$ Ha. The QP equation is solved on a grid with $N_g = 1001$ grid points and a step size of $\Delta\omega = 10^{-3}$ Ha, using the one-shot GW, or G_0W_0, approach.

		MAE VOTCA w.r.t. MOLGW		
Molecule	N_{MO}	$\varepsilon_{\mathrm{QP}}(1{:}16)$	$\varepsilon_{\mathrm{QP}}(:)$	$\Omega(1{:}20)$
Aldehydes Ketones and Amides				
Acetamide	190	$1.4530 \cdot 10^{-3}$	$1.2247 \cdot 10^{-2}$	$1.7847 \cdot 10^{-3}$
Acetone	204	$3.0527 \cdot 10^{-5}$	$1.8134 \cdot 10^{-2}$	$2.7562 \cdot 10^{-3}$
Benzoquinone	296	$2.7977 \cdot 10^{-3}$	$2.2668 \cdot 10^{-2}$	$3.3710 \cdot 10^{-3}$
Formaldehyde	88	$5.5528 \cdot 10^{-3}$	$1.9735 \cdot 10^{-2}$	$2.6727 \cdot 10^{-3}$
Formamide	132	$1.0101 \cdot 10^{-3}$	$2.1434 \cdot 10^{-2}$	$3.1503 \cdot 10^{-3}$
Propanamide	248	$5.7730 \cdot 10^{-3}$	$8.0033 \cdot 10^{-3}$	$2.9233 \cdot 10^{-3}$
Aromatic Hydrocarbons and Heterocycles				
Benzene	264	$2.9704 \cdot 10^{-5}$	$3.0326 \cdot 10^{-2}$	$9.9520 \cdot 10^{-4}$
Furan	206	$7.0041 \cdot 10^{-3}$	$1.8823 \cdot 10^{-2}$	$1.7855 \cdot 10^{-3}$
Imidazole	206	$4.8687 \cdot 10^{-4}$	$1.2651 \cdot 10^{-2}$	$2.3440 \cdot 10^{-3}$
Pyrazine	236	$3.7296 \cdot 10^{-5}$	$2.6522 \cdot 10^{-2}$	$2.3565 \cdot 10^{-3}$
Pyridazine	236	$2.8867 \cdot 10^{-3}$	$1.8521 \cdot 10^{-2}$	$2.5782 \cdot 10^{-3}$
Pyridine	250	$1.1898 \cdot 10^{-3}$	$1.6134 \cdot 10^{-2}$	$2.4574 \cdot 10^{-3}$
Pyrimidine	236	$8.6926 \cdot 10^{-4}$	$1.8153 \cdot 10^{-2}$	$3.1553 \cdot 10^{-3}$
Pyrrole	220	$3.5979 \cdot 10^{-5}$	$1.8510 \cdot 10^{-2}$	$1.2814 \cdot 10^{-3}$
Tetrazine	208	$6.9412 \cdot 10^{-4}$	$2.6270 \cdot 10^{-2}$	$1.8012 \cdot 10^{-3}$
Triazine	222	$6.2258 \cdot 10^{-5}$	$1.8024 \cdot 10^{-2}$	$4.2228 \cdot 10^{-3}$
Nucleobases				
Cytosine	310	$1.2920 \cdot 10^{-2}$	$9.8701 \cdot 10^{-3}$	$2.0644 \cdot 10^{-3}$
Uracil	296	$2.7424 \cdot 10^{-3}$	$1.0618 \cdot 10^{-2}$	$1.1647 \cdot 10^{-3}$
Unsaturated Aliphatic Hydrocarbons				
Butadiene	204	$2.8830 \cdot 10^{-5}$	$1.7030 \cdot 10^{-2}$	$1.4319 \cdot 10^{-3}$
Cyclopentadiene	234	$5.0763 \cdot 10^{-4}$	$1.4671 \cdot 10^{-2}$	$1.7112 \cdot 10^{-3}$
Cyclopropene	146	$2.0576 \cdot 10^{-4}$	$2.9697 \cdot 10^{-2}$	$1.8945 \cdot 10^{-3}$
Ethene	116	$3.3208 \cdot 10^{-5}$	$2.8555 \cdot 10^{-2}$	$1.7816 \cdot 10^{-3}$
Hexatriene	292	$6.4991 \cdot 10^{-5}$	$1.7746 \cdot 10^{-2}$	$1.3282 \cdot 10^{-3}$
Norbornadiene	322	$4.5312 \cdot 10^{-5}$	$9.6248 \cdot 10^{-3}$	$1.3239 \cdot 10^{-3}$
Mean		$1.9359 \cdot 10^{-3}$	$1.8499 \cdot 10^{-2}$	$2.1807 \cdot 10^{-3}$

Table 5.6: A comparison of the first singlet transitions S_0 in eV between FAA, PPM and TBE-2. The self-energy correlation in the FAA is evaluated using $\eta = 10^{-3}$ Ha. The QP equation is solved on a grid with $N_g = 1001$ grid points and a step size of $\Delta\omega = 10^{-3}$ Ha. The QP equation is solved either for 1 GW iteration (G_0W_0), or for 10 GW iterations ($evGW$). The MSE (Mean Signed Error) and MAE (Mean Absolute Error) of FAA and PPM w.r.t. TBE-2 are given below.

Molecule	Transition	G_0W_0		$evGW$		TBE-2
		FAA	PPM	FAA	PPM	
Aldehydes Ketones and Amides						
Acetamide	$16 \to 17$	4.97771	4.66522	5.58034	5.30572	5.62000
Acetone	$16 \to 17$	3.67555	2.84606	4.26198	3.99425	4.38000
Benzoquinone	$28 \to 29$	1.90735	1.71934	2.71519	2.20075	2.74000
Formaldehyde	$8 \to 9$	3.27432	3.09754	3.91539	3.72679	3.88000
Formamide	$12 \to 13$	4.82427	4.65837	5.52638	5.18819	5.55000
Aromatic Hydrocarbons and Heterocycles						
Benzene	$20 \to 23$	4.86174	4.82925	5.12470	5.12625	5.08000
Furan	$18 \to 19$	6.27622	5.11582	6.78702	6.51783	6.32000
Imidazole	$18 \to 21$	5.99352	5.94671	6.58038	6.20550	6.25000
Naphthalene	$34 \to 35$	4.01313	3.83207	4.34703	4.22445	4.82000
Pyrazine	$21 \to 22$	3.44741	3.05088	3.98430	3.73437	4.13000
Pyridazine	$21 \to 22$	3.09056	2.72862	3.69500	3.39006	3.85000
Pyridine	$21 \to 22$	4.31981	4.02911	4.95705	4.59701	4.59000
Pyrimidine	$21 \to 22$	3.81280	3.52679	4.39806	4.16724	4.43000
Pyrrole	$17 \to 22$	7.33080	7.16310	7.59698	7.41841	6.37000
Tetrazine	$21 \to 22$	1.74681	1.15375	2.21190	2.11662	2.46000
Triazine	$20 \to 22$	3.96351	3.68081	4.64286	4.33463	4.70000
Nucleobases						
Cytosine	$29 \to 30$	4.21420	3.86504	4.73955	4.03979	4.66000
Thymine	$32 \to 34$	4.20399	3.79770	4.93056	4.42220	4.82000
Uracil	$28 \to 30$	4.19776	3.84634	4.89970	4.21910	5.00000
Unsaturated Aliphatic Hydrocarbons						
Butadiene	$15 \to 16$	5.53701	5.36811	5.92842	5.75604	6.18000
Cyclopropene	$11 \to 12$	6.18371	6.13841	6.63045	5.72745	6.68000
Ethene	$8 \to 9$	8.11641	7.91217	8.57232	8.49894	7.80000
Hexatriene	$22 \to 23$	4.50930	4.06937	4.92675	4.64083	5.10000
Norbornadiene	$25 \to 26$	4.78619	4.21685	5.15112	4.78626	5.37000
Octatetraene	$29 \to 30$	3.84528	3.58668	4.25007	3.96788	4.66000
MSE		−0.49323	−0.82384	0.03654	−0.28534	
MAE		0.59540	0.89626	0.23818	0.44521	

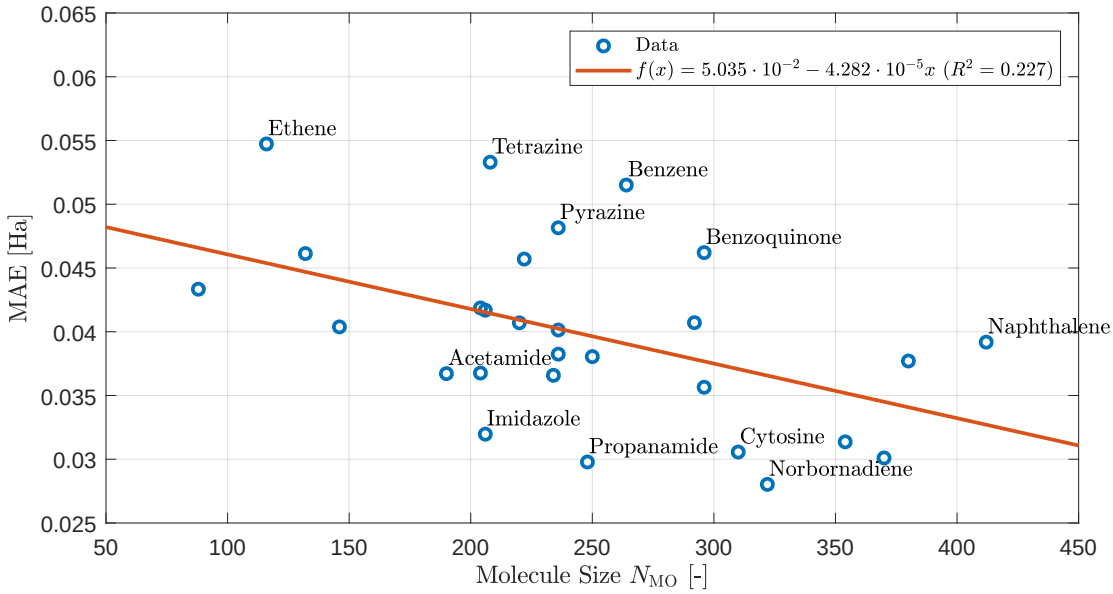

Figure 5.9: The Mean Absolute Error (MAE) of the QP energies between the FAA and PPM (Equation 5.1) as a function of the molecule size N_{MO}, for all molecules in the Thiel set. The self-energy correlation is evaluated using $\eta = 10^{-3}$ Ha. The QP equation is solved for 10 GW iterations ($evGW$) on a grid with $N_g = 1001$ grid points and a step size of $\Delta\omega = 10^{-3}$ Ha. The blue circles represent the MAEs and the red line represents a simple linear regression fit.

We compare the computational effort between both methods. For the duration of all calculations, we log their accumulated CPU time and memory usage. In Figure 5.10, we plot the accumulated CPU time as a function of the molecule size N_{MO}. By fitting power functions to the data points, we estimate the empirical scaling of both methods. The FAA calculations scale as $\mathcal{O}(N_{\mathrm{MO}}^{3.87})$, whereas the PPM calculations scale as $\mathcal{O}(N_{\mathrm{MO}}^{2.83})$. As expected, the FAA is computationally more demanding than the PPM. However, the empirical scalings do not match the theoretical scalings of $\mathcal{O}(N_{\mathrm{MO}}^{6})$ and $\mathcal{O}(N_{\mathrm{MO}}^{4})$ for the FAA and PPM respectively. This suggests that the computational bottleneck of these calculations lies elsewhere, i.e. not at the evaluation of the self-energy.

In order to explain the observed empirical scalings, we take a closer look at the FAA naphthalene calculation. Naphthalene is the largest molecule of the Thiel set with $N_{\mathrm{MO}} = 412$. In order to get a sense of where the computation times are spent, we determine the accumulated CPU times of: (1) the GW diagonalization step, in which the two-particle Hamiltonian $\underline{\mathbf{H}}^{\mathrm{2p}} \in \mathbb{R}^{N_t \times N_t}$ is diagonalized, and (2) the GW root-finding step, in which the QP equation is solved. The resulting timings are reported in Figure 5.11. A hefty 92.59% of the total time is spent on the root-finding step while only 7.41% is spent on the diagonalization step. Evidently, the diagonalization step does not form the bottleneck for these small molecules. Rather, the bottleneck is formed by the grid root-finding method, which scales with the number of grid points, in addition to the molecule size.

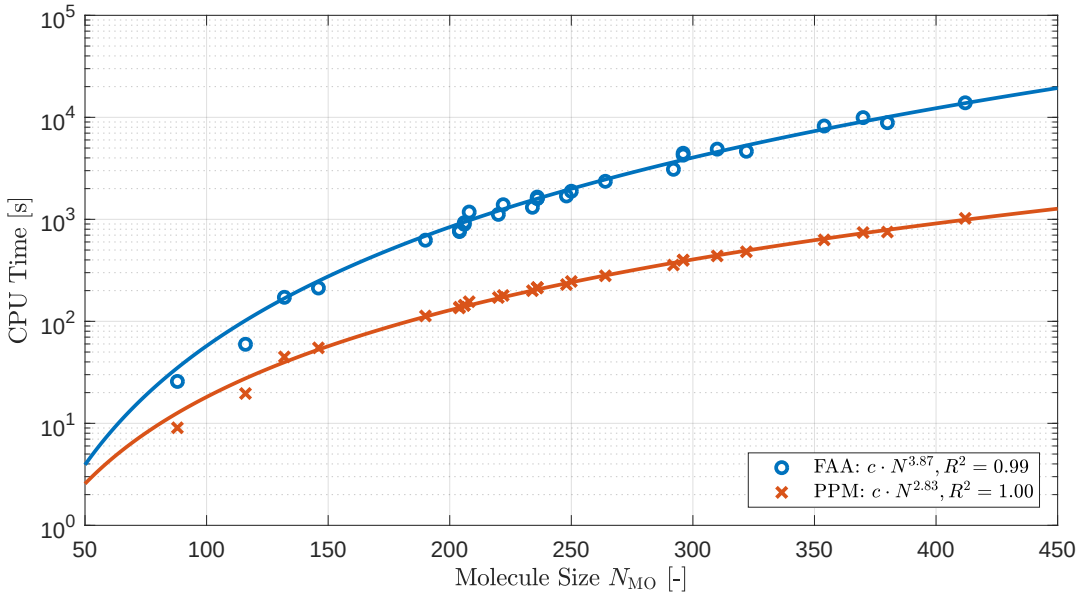

Figure 5.10: The accumulated CPU time as a function of the molecule size N_{MO}. The self-energy correlation is evaluated using $\eta = 10^{-3}$ Ha. The QP equation is solved for 10 *GW* iterations (*evGW*) on a grid with $N_g = 1001$ grid points and a step size of $\Delta\omega = 10^{-3}$ Ha. The markers represent data points. The lines represent power function fitted to the data.

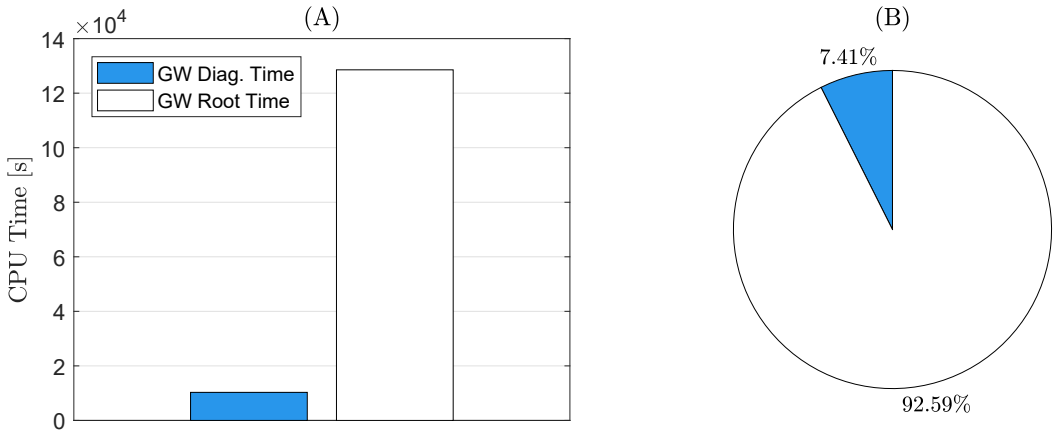

Figure 5.11: The accumulated CPU times of: the *GW* diagonalization step ("GW Diag. Time"), in which the two-particle Hamiltonian $\underline{\mathbf{H}}^{2\mathrm{p}} \in \mathbb{R}^{N_t \times N_t}$ is diagonalized, and the *GW* root-finding step ("GW Root Time"), in which the QP equation is solved. The self-energy correlation is evaluated using $\eta = 10^{-3}$ Ha. The QP equation is solved for 10 *GW* iterations (*evGW*) on a grid with $N_g = 1001$ grid points and a step size of $\Delta\omega = 10^{-3}$ Ha. In (A), the timings are represented in a bar chart and in (B) as a pie chart.

Chapter 6

Conclusion

In this thesis, I investigated the excited state properties of molecular systems using the DFT-GW-BSE procedure, within the framework of Many-Body Perturbation Theory (MBPT). In the derivation of the DFT-GW-BSE procedure, many approximations have to be made, including: Born-Oppenheimer, KS (Kohn-Sham), GW, QP (Quasi-Particle), RPA (Random Phase Approximation). Without simplifying the quantum mechanical systems, calculations–analytical or numerical–are impossible on larger, more interesting, systems. Despite these approximations, DFT accurately predicts ground state energies and GW improves upon this to yield inherently more accurate excitation energies.

The central quantity of GW is the self-energy operator Σ, which is given by a convolution of the Green's function G and the screened Coulomb interaction W. The integration of the frequency-dependence is particularly computationally demanding. I discussed two methods to perform this integration; the Fully-Analytical Approach (FAA)–direct analytical integration–and the Plasmon-Pole Model (PPM)–analytical integration of an approximate convolution. The bottleneck of GW is not the integration itself, but rather the evaluation of the polarizability P, which in turn involves diagonalizing the two-particle Hamiltonian $H^{2\mathrm{p}} \in \mathbb{R}^{N_t \times N_t}$. The FAA performs the full diagonalization of $H^{2\mathrm{p}}$ such that the GW convolution can be evaluated analytically, which scales with $\mathcal{O}(N^6)$. The PPM approximates the GW convolution and requires the computation of the plasmon-pole, which scales with $\mathcal{O}(N^4)$.

I implemented the FAA for the GW step of the DFT-GW-BSE procedure. Two notable obstacles that I encountered while implementing the method were, firstly, the introduction of the "small" parameter η and, secondly, numerically solving the QP equation. Below, I discuss these problems.

The "small" parameter η is introduced in the FAA to shift the poles of the self-energy off the imaginary axis. This parameter introduces an error in the GW calculation, which is reduced as $\eta \to 0$. However, as η decreases, the derivative Σ_c' becomes less behaved, which causes numerical issues in solving the QP equation. In all calculations, I simply set $\eta = 10^{-3}$ Ha, which is the default value used in MOLGW. It is unclear whether decreasing the value of η would yield more accurate results. If so, would the improvement in accuracy be worth the extra computational effort caused by small values of η? The effect of η should be investigated.

The QP equation is solved numerically using a standard root-finding algorithm. In the earlier versions of VOTCA, the default root-finding technique was a fixed-point iteration. While this method is both simple and effective for the easier spectral functions that the PPM produces, it failed to converge for the FAA. In this thesis, I proposed two alternative root-finding methods; Newton's method and a brute-force grid approach. The derivative of the self-energy correlation can be expressed in closed-form, making Newton's method a viable contender. However, since implementing the FAA was my main objective, I resorted to the simpler grid method, which was more workable in the GW framework of VOTCA. Furthermore, MOLGW also uses a grid method. Using the same root-finding method allowed for more direct energy comparisons between VOTCA and MOLGW. An important limitation of the grid method, however, is that the accuracy of the QP energies is limited to the resolution of the root-finding grid. In later versions of VOTCA, the default fixed-point iteration is replaced by a grid method which kick-starts a subsequent Newton iteration.

The research questions consist of; firstly, is the FAA implemented correctly and, secondly, how does the accuracy and performance of the FAA compare to the PPM? To answer these questions, I performed GW-BSE calculations on molecules of the Thiel set and compared the resulting QP and neutral excitation energies to PPM, MOLGW and the TBE-2 dataset. The following is an overview of my findings.

I compared the FAA implementation to that of MOLGW in an ethene case study. I observed that the KS energies between VOTCA and MOLGW matched within 10^{-4} Ha. Since the KS energies only serve as an initial guess to the QP energies, any mismatch between the KS energies does not limit the relative accuracy of the QP energies later. For the first 16 MOs, both the self-energy correlation and the QP energies matched within 10^{-4} Ha, the same as the KS energies. However, for the high-energy MOs, errors increased to the order of 10^{-2} Ha. Note that the QP energies are limited to the grid accuracy of 10^{-3} Ha. The errors of 10^{-2} Ha are therefore not expected. I propose two possible explanations for these errors. Firstly, the self-energy correlation function may simply be implemented differently between VOTCA and MOLGW. Another explanation could be that the MOs are arranged differently between VOTCA and MOLGW. The MOs are ordered in increasing energy. Slight energy variations in degenerate MOs may cause different MO orderings. As a result, the i-th QP energy in VOTCA and MOLGW may be associated to different MOs. Either explanation must be investigated. Finally, I compared the first 20 singlet energies between VOTCA and MOLGW. These matched up to the grid resolution of 10^{-3} Ha and seemed unaffected by the errors in the high-energy MOs.

The MOLGW comparison was extended to all molecules in the Thiel set. Importantly, ethene did not stand out as an exceptional case, which reaffirmed my conclusions from the ethene case study.

In order to test the accuracy between the FAA and PPM, I compare the first singlet excitation energies (S_0) to the estimates of the TBE-2 dataset. Whichever method resembles the TBE-2 estimates the best is considered to be the most accurate of the two. The findings completely agreed with the theory; the FAA yielded more accurate energies than the approximate PPM and, simultaneously, the self-consistent *evGW* approach yielded more accurate energies than the one-shot G_0W_0 approach. Therefore, if the highest degree accuracy is desired, the FAA must be chosen over PPM.

While the neutral excitation energies are the final result of the GW-BSE calculation, the FAA and PPM methods diverge from one another in the GW step. Therefore, in order to measure the difference between two methods, I compared the QP energies between both methods. I observed that the difference between the FAA and PPM decreased as the sizes of the molecules increased. From this, I concluded that the approximate PPM results approach the theoretical QP energies better for increasingly larger molecules.

The empirical scaling of the FAA was found to be $\mathcal{O}(N_{\mathrm{MO}}^{3.87})$, whereas that of the PPM $\mathcal{O}(N_{\mathrm{MO}}^{2.83})$. As expected, the FAA is computationally more demanding than PPM. However, the empirical scalings did not agree with the theoretical scaling of $\mathcal{O}(N_{\mathrm{MO}}^{6})$ for the FAA and $\mathcal{O}(N_{\mathrm{MO}}^{4})$ for the PPM. I found that, for the small molecules in the Thiel set, the computation times are not dominated by the diagonalization of $H^{2\mathrm{p}}$, but rather by the root-finding step, during which the QP equation is solved. It is likely that the observed trend in CPU time is not applicable for large molecules, where I would expect that the diagonalization of $H^{2\mathrm{p}}$ is the time-dominant step. For these small molecules, the computational cost could be significantly reduced by employing a better root-finding strategy. For example, Newton's iterative method could be used instead of the brute-force grid method. Otherwise, a lower-resolution grid could be used to kick-start one of the efficient iterative methods. Using an iterative method to finalize the QP energies would also remove the accuracy restriction imposed by the resolution of the root-finding grid.

From the previous results, I note the following. As the molecule size increases, the computational cost of the FAA increases more rapidly than PPM. At the same time, the difference in QP energies between both methods decreases. If this trend continues for larger molecules, the relatively large gain in computational efficiency of the PPM method would outweigh the relatively small increase in accuracy of the Exact method.

In conclusion, the FAA produced singlet energies that were accurate to the MOLGW energies up to the grid resolution. This suggests that indeed the FAA was implemented correctly. Furthermore, the FAA was found to yield more accurate singlet energies than PPM. This gain in accuracy, however, comes at a significant computational price. I argue that the FAA is better suited for benchmarking other *GW* implementations, whereas approximate methods such as the PPM are better suited for large scale analyses. Since only small molecules were tested, the bottleneck of the *GW* calculation was not the diagonalization step, but rather by the root-finding step. As system sizes increase, I expect to see a sharp rise in computational cost as the diagonalization step, which is expected to scale with $\mathcal{O}(N^6)$, takes the overhand. The accuracy-cost trade-off would then shift even more in favour of the PPM method. Future studies may focus on testing large molecular systems to verify this expected trend.

Bibliography

[1] P. Hohenberg and W. Kohn. Inhomogeneous electron gas. *Phys. Rev.*, 136:B864–B871, Nov 1964.

[2] W. Kohn. Nobel lecture: Electronic structure of matter—wave functions and density functionals. *Rev. Mod. Phys.*, 71:1253–1266, Oct 1999.

[3] J. P. Perdew. Density functional theory and the band gap problem. *Int. J. Quantum Chem.*, 28(S19):497–523, 1985.

[4] A. Szabo and N. S. Ostlund. *Modern Quantum Chemistry: Introduction to Advanced Electronic Structure Theory*. 01 1989.

[5] V. Rühle, A. Lukyanov, F. May, M. Schrader, T. Vehoff, J. Kirkpatrick, B. Baumeier, and D. Andrienko. Microscopic simulations of charge transport in disordered organic semiconductors. *Journal of Chemical Theory and Computation*, 7(10):3335–3345, 2011.

[6] V. Rühle, A. Lukyanov, F. May, M. Schrader, T. Vehoff, J. Kirkpatrick, B. Baumeier, and D. Andrienko. Microscopic simulations of charge transport in disordered organic semiconductors. *Journal of Chemical Theory and Computation*, 7(10):3335–3345, 2011.

[7] J. Wehner, L. Brombacher, J. Brown, C. Junghans, O. Caylak, Y. Khalak, P. Madhikar, G. Tirimbò, and B. Baumeier. Electronic excitations in complex molecular environments: Many-body green's functions theory in votca-xtp. *Journal of Chemical Theory and Computation*, 14(12):6253–6268, 12 2018.

[8] G. Tirimbò, V. Sundaram, O. Caylak, W. Scharpach, J. Sijen, C. Junghans, J. Brown, F. Zapata Ruiz, N. Renaud, J. Wehner, and B. Baumeier. Excited-state electronic structure of molecules using many-body greens functions: Quasiparticles and electron-hole excitations with votca-xtp. *The Journal of Chemical Physics*, 152(11):114103, 2020.

[9] Votca-xtp github. https://github.com/votca/xtp. Accessed: April 2020.

[10] E. Schrödinger. Quantisierung als eigenwertproblem. *Ann. Phys.*, 384(4):361–376, 1926.

[11] M. Born and R. Oppenheimer. Zur quantentheorie der molekeln. *Ann. Phys.*, 389(20):457–484, 1927.

[12] J. C. Slater. The self consistent field and the structure of atoms. *Phys. Rev.*, 32:339–348, Sep 1928.

[13] J. A. Gaunt. A theory of hartree's atomic fields. *Math. Proc. Camb. Philos. Soc.*, 24(2):328–342, 1928.

[14] J. C. Slater. Note on hartree's method. *Phys. Rev.*, 35:210–211, Jan 1930.

[15] V. Fock. Näherungsmethode zur lösung des quantenmechanischen mehrkörperproblems. *Z. Phys.*, 61(1):126–148, Jan 1930.

[16] J. Wehner. *Investigation of exciton properties in organic materials via many-body perturbation theory.* PhD thesis, Department of Mathematics and Computer Science, 5 2019. PhD thesis.

[17] W. Kohn and L. J. Sham. Self-consistent equations including exchange and correlation effects. *Phys. Rev.*, 140:A1133–A1138, Nov 1965.

[18] A. D. Becke. Density-functional thermochemistry. iii. the role of exact exchange. *J. Chem. Phys.*, 98(7):5648–5652, 1993.

[19] F. J. Devlin, J. W. Finley, P. J. Stephens, and M. J. Frisch. Ab initio calculation of vibrational absorption and circular dichroism spectra using density functional force fields: A comparison of local, nonlocal, and hybrid density functionals. *J. Phys. Chem.*, 99(46):16883–16902, 1995.

[20] J. P. Perdew, K. Burke, and M. Ernzerhof. Generalized gradient approximation made simple. *Phys. Rev. Lett.*, 77:3865–3868, Oct 1996.

[21] K. Burke and L. O. Wagner. Dft in a nutshell. *Int. J. Quantum Chem.*, 113(2):96–101, 2013.

[22] C. Adamo, G. E. Scuseria, and V. Barone. Accurate excitation energies from time-dependent density functional theory: Assessing the pbe0 model. *J. Chem. Phys.*, 111(7):2889–2899, 1999.

[23] S. Obara and A. Saika. Efficient recursive computation of molecular integrals over cartesian gaussian functions. *J. Chem. Phys.*, 84(7):3963–3974, 1986.

[24] C. Faber. *Electronic, excitonic and polaronic properties of organic systems within the many-body GW and Bethe-Salpeter formalisms : towards organic photovoltaics.* Theses, Université de Grenoble, November 2014.

[25] J. Harl. *The linear response function in density functional theory.* PhD thesis, Fakultät für Physik, 2008. PhD thesis.

[26] L. Hedin. New method for calculating the one-particle green's function with application to the electron-gas problem. *Phys. Rev.*, 139(3A):A796–A823, 1965.

[27] F. Bruneval, T. Rangel, S. M. Hamed, M. Shao, C. Yang, and J. B. Neaton. molgw 1: Many-body perturbation theory software for atoms, molecules, and clusters. *Comput. Phys. Commun.*, 208:149 – 161, 2016.

[28] M. J. van Setten, F. Weigend, and F. Evers. The gw-method for quantum chemistry applications: Theory and implementation. *J. Chem. Theory Comput.*, 9(1):232–246, 2013. PMID: 26589026.

[29] S. V. Faleev, M. van Schilfgaarde, and T. Kotani. All-electron self-consistent *gw* approximation: Application to si, mno, and nio. *Phys. Rev. Lett.*, 93:126406, Sep 2004.

[30] M. Rohlfing, P. Krüger, and J. Pollmann. Efficient scheme for gw quasiparticle band-structure calculations with applications to bulk si and to the si(001)-(2×1) surface. *Phys. Rev. B*, 52:1905–1917, Jul 1995.

[31] G. Guennebaud and B. Jacob et al. Eigen v3. http://eigen.tuxfamily.org, 2010.

[32] Intel Software. Intel vtune amplifier. https://software.intel.com/en-us/vtune. Accessed: September 2019.

[33] M. Schreiber, M. R. Silva-Junior, S. P. A. Sauer, and W. Thiel. Benchmarks for electronically excited states: Caspt2, cc2, ccsd, and cc3. *J. Chem. Phys.*, 128(13):134110, 2008.

[34] D. Jacquemin, I. Duchemin, and X. Blase. Benchmarking the bethe-salpeter formalism on a standard organic molecular set. *J. Chem. Theory Comput.*, 11(7):3290–3304, 2015. PMID: 26207104.

[35] X. Ren, P. Rinke, V. Blum, J. Wieferink, A. Tkatchenko, A. Sanfilippo, K. Reuter, and M. Scheffler. Resolution-of-identity approach to hartree-fock, hybrid density functionals, rpa, mp2 and gw with numeric atom-centered orbital basis functions. *New J. Phys.*, 053020, 05 2012.

[36] L. J. Whitten. Coulombic potential energy integrals and approximations. *J. Chem. Phys.*, 58(10):4496–4501, 1973.

BIBLIOGRAPHY

Appendices

A.1 Contour Deformation Techniques

Here, we provide a short description of contour deformation techniques. Integrals over the real axis $(-\infty, +\infty)$ can be simplified by means of contour deformation. Consider the following common type of integral:

$$\int_{-\infty}^{\infty} \mathrm{d}\omega I(\omega) = \frac{1}{2\pi i} \int_{-\infty}^{\infty} \mathrm{d}\omega \frac{f(\omega)}{\omega - i\eta}, \qquad \omega \in \mathbb{R}. \tag{1}$$

Instead of solving this integral along the real axis, we instead consider a contour integral along the upper half of a circle with radius R in the complex plane (See Figure 1). We split the closed contour C into the contour C_1 along the real axis and the contour C_2 along the semi-circle:

$$\oint_C \mathrm{d}z I(z) = \oint_{C_1} \mathrm{d}z I(z) + \oint_{C_2} \mathrm{d}z I(z), \qquad z \in \mathbb{C}. \tag{2}$$

The contour C_2 is further parametrized using $z = Re^{i\theta} = R\cos(\theta) + iR\sin(\theta)$, $dz = iRe^{i\theta}d\theta$. The contour integrals over C_1 and C_2 are then given by:

$$\oint_{C_1} \mathrm{d}z I(z) = \int_{-R}^{R} \mathrm{d}\omega I(\omega), \tag{3}$$

$$\oint_{C_2} \mathrm{d}z I(z) = \int_{0}^{\pi} iRe^{i\theta} \mathrm{d}\theta I(Re^{i\theta}). \tag{4}$$

According to the residue theorem, the closed contour integral over $I(z)$ yields

$$\oint_C \mathrm{d}z I(z) = 2\pi i \sum_k \mathrm{Res}(I, z_k), \tag{5}$$

with z_k the simple poles enclosed by the contour C and $\mathrm{Res}(I, z_k)$ the residues corresponding to the poles z_k, i.e. the coefficient of the $(z - z_k)^{-1}$ summand in a Laurent expansion. Next, we use Jordan's Lemma, which states that

$$\left| \oint \mathrm{d}z f(z) \right| \leq \frac{\pi}{a} M_R, \qquad M_R := \max_{\theta \in [0,\pi]} \left\{ g(Re^{i\theta}) \right\} \tag{6}$$

for continuous function $f(z) = e^{iaz} g(z)$. Furthermore, $\lim_{R\to\infty}\{M_R\} = 0$ such that

$$\lim_{R\to\infty} \left\{ \oint_{C_R} f(z) dz \right\} = 0, \tag{7}$$

where c_R denotes a semi-circular contour with radius R. Applying Jordan's Lemma to the contour integral of C_2, we conclude

$$\lim_{R\to\infty} \left\{ \oint_C \mathrm{d}z I(z) \right\} = \lim_{R\to\infty} \left\{ \int_{-R}^{R} \mathrm{d}\omega I(\omega) \right\} = \int_{-\infty}^{\infty} \mathrm{d}\omega I(\omega) = 2\pi i \sum_k \mathrm{Res}(I, z_k). \tag{8}$$

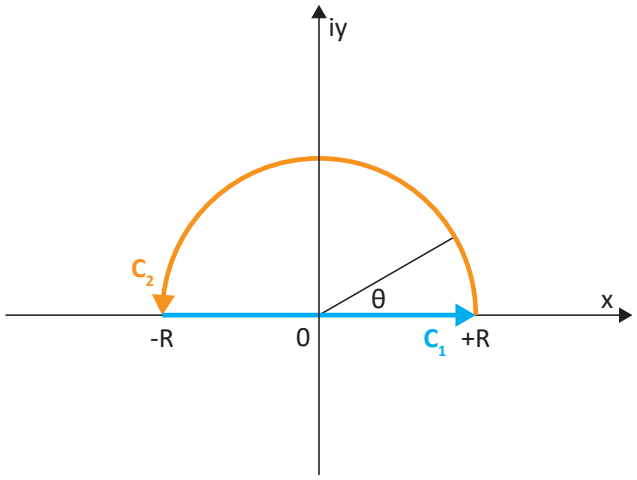

Figure 1: The two contours C_1 and C_2 form a semi-circle in the complex plane. C_1 lies along $[-R, +R]$ on the real axis and C_2 is the upper half of the circle with radius R.

B.2 Four-Center Integral

The molecular orbital electronic repulsion integral (ERI) is defined as

$$K_{a,b}^{c,d} \equiv (ab|cd) := \iint \mathrm{d}\mathbf{r}_1 \mathrm{d}\mathbf{r}_2 \, \frac{\phi_a(\mathbf{r}_1)\phi_b(\mathbf{r}_1)\phi_c^*(\mathbf{r}_2)\phi_d^*(\mathbf{r}_2)}{|\mathbf{r}_1 - \mathbf{r}_2|} \equiv (ab|cd). \tag{9}$$

This integral is otherwise known as the *four-center integral*, as it calculates the convolution of four orbitals. The evaluation of these four-center integrals is computationally demanding and forms the traditional bottleneck for DFT-type calculations. We can accelerate their computation using atom-centered basis functions using to the *Resolution-of-the-Identity* (RI) approximation [35]. The pair product of basis functions are expanded in terms of *auxiliary basis functions* χ_γ:

$$|ab) \approx |\widetilde{ab}) = \sum_\gamma C_{a,b}^\gamma \chi_\gamma(\mathbf{r}_1), \tag{10}$$

where the coefficients $C_{a,b}^\gamma$ are found by minimizing of the error $\delta = (ab|cd) - (\widetilde{ab}|cd)$ [36]:

$$C_{a,b}^\gamma = \sum_\alpha (ab|\alpha)[\underline{\mathbf{V}}^{-1}]_{\alpha,\gamma}. \tag{11}$$

The set of auxiliary basis functions χ_γ is called the *auxiliary basis set*. The three-center and two-center integrals respectively defined as:

$$(ab|\alpha) := \iint \mathrm{d}\mathbf{r}_1 \mathrm{d}\mathbf{r}_2 \; \phi_a(\mathbf{r}_1)\phi_b(\mathbf{r}_1) \frac{1}{|\mathbf{r}_1 - \mathbf{r}_2|} \phi_\alpha(\mathbf{r}_2), \tag{12a}$$

$$[\underline{\mathbf{V}}]_{\alpha,\gamma} = (\alpha|\gamma) := \iint \mathrm{d}\mathbf{r}_1 \mathrm{d}\mathbf{r}_2 \; \phi_\alpha(\mathbf{r}_1) \frac{1}{|\mathbf{r}_1 - \mathbf{r}_2|} \phi_\gamma(\mathbf{r}_2). \tag{12b}$$

The four-center integral is then approximated by

$$\begin{aligned}(ab|cd) \approx (\widetilde{ab}|cd) &= \sum_{\gamma} C^{\gamma}_{a,b}(\gamma|cd) \\ &= \sum_{\alpha,\gamma}(ab|\alpha)[\underline{\mathbf{V}}^{-1}]_{\alpha,\gamma}(\gamma|cd) \\ &= \sum_{\alpha,\beta,\gamma}(ab|\alpha)[\underline{\mathbf{V}}^{-1/2}]_{\alpha,\beta}[\underline{\mathbf{V}}^{-1/2}]_{\beta,\gamma}(\gamma|cd) \\ &= \sum_{\beta}\left[\sum_{\alpha}(ab|\alpha)[\underline{\mathbf{V}}^{-1/2}]_{\alpha,\beta}\right]\left[\sum_{\gamma}[\underline{\mathbf{V}}^{-1/2}]_{\beta,\gamma}(\gamma|cd)\right] \\ &= \sum_{\beta} M^{\beta}_{a,b}M^{\beta}_{c,d}. \end{aligned} \tag{13}$$

In practice $\underline{\mathbf{V}}$ is positive definite [27], such that its square root can be calculated. In conclusion, four-center integrals are efficiently evaluated using pre-computed $M^{\beta}_{a,b}$ and $M^{\beta}_{c,d}$:

$$(ab|cd) \approx \sum_{\beta} M^{\beta}_{a,b}M^{\beta}_{c,d}. \tag{14}$$

Pre-computing $M^{\beta}_{a,b}$ requires the storage of $N_b^2 \cdot N_x$ doubles, whereas pre-computing the four-center integrals exactly would require the storage of N_b^4 doubles.